Mechanical And Electronic Properties Of Technologically Important Materials

A Thesis submitted for the degree of

Doctor of Philosophy (Science)
in
Physics (Theoretical)

by

Poulami Chakraborty

Department of Physics
University of Calcutta

2018

Dedicated To……

My mother

……for being an inspiration.

Acknowledgements

Looking back and remembering the enthusiasm and excitement I had when I first joined, I feel like a completely different person now. In this long journey filled with medley of emotions, I am at a loss while reflecting on the contributions of so many people who had left an impression. It seems an impossible task to acknowledge this huge team work which results in a Ph.D., I apologise for the names which remain unspoken due to lack of space.

The first name which comes to mind is that of my supervisor Prof. Tanusri Saha-Dasgupta. Her humongous drive and self motivation towards research is awe inspiring. Her constant push and perseverance motivated me to come out of my comfort zone and give my best. She supported and encouraged me not only to discuss academic issues but also personal problems. Her attitude towards science and towards life has influenced my overall perspective for which I am grateful to her. I take this opportunity to express my gratitude and deepest regards to my supervisor for having faith in me. I am thankful to my collaborator Dr. Amitava Moitra for his immense support and guidance. He gave me the freedom and confidence to think out of the box, always welcomed my doubts, answered them patiently and encouraged me to question more without any hesitation. I am thankful to Dr. Amlan Dutta for the long discussion sessions where he patiently clarified my doubts. He was always very helpful with his vast knowledge on numerous computational tecniques. I would like to Dr. Lilia Boeri for giving her invaluable time for discussion and the wonderful ideas that she shared with us. A special thanks to Dr. Tilmann Hickel and Prof. Jörg Neugebauer for giving me the oppurtunity to present my work and interact with the group members.

I convey my thanks and heartfelt regards to my seniors and collaborators

Dr. Tilak Das and Dr. Aurab Chakrabarty who were always there to help me whenever I got stuck with any problem. I have learnt a lot of computational techniques from them. I want to thank Rohit from IISER Pune for helping me with my VASP queries. I convey my thanks to my collaborator Pallabi Paul and all my group mates - Hrishit, Kartik, Dhani, Anita, Shreya, Ransell and Edwin for their constant help and support. Dhani and Poonam has been much more than a friend, their sisterly love and affection made S. N. Bose a second home for me. Now, I would mention those without whom this roller-coaster ride would have remained void - Subhadip, Aslam, Subrata, Rakesh, Ananda, Sumanto, Arpita, Karan, Ravi. In this long arduous journey filled with many ups and downs Subhadip is one name without whom I doubt I would have survived so long, he is among the likes who could transform any situation into something straight out of a comic book. For him, only one line would suffice, he is the Asterix in my Asterix and Obelix. Sumanto had been a positive influence, his steady motivation and career advices helped me to look forward. Ravi had played a pivotal role in these years, the long academic discussions widened my perspective and understanding of the subject and has inspired me to think differently and challenge myself. I appreciate his constant patience and understanding. I have been lucky to be friends with seniors like Subhojit, Biplab and Arghya whose attitude towards learning new things never failed to surprise me. I would miss the long hearty discussions with my senior Siddhi whose great sense of humour always cheered me up. My postgraduate friends who deserve a special mention are Vaibhav, Saheli, Tausif and last but not the least, my childhood friend Shrobona, the one who introduced me to the world of Physics. She is my trusted friend who has always been patient and supportive of me.

My acknowledgement is incomplete without the mention of my family - mom, dad, sister and brother. No words can suffice their unconditional love, support and patience for bearing with me. My mother has been my role model who taught me “even sky is not the limit”. She was always there to pull me up whenever I fell down. My sister encourages me to stay strong and calm even in the face of a storm. I consider myself extremely lucky to have such a liberal family where I have never faced any obstruction to follow my dreams.

List of Publications

1. *Effect of hydrogen on degradation mechanism of zirconium: A molecular dynamics study*
   Poulami Chakraborty, Amitava Moitra and Tanusri Saha-Dasgupta.
   J. Nucl. Mater. 466 (2015) 172.

2. *Manipulating the mechanical properties of Ti_2C MXene: Effect of substitutional doping*
   Poulami Chakraborty, Tilak Das, Dhani Nafday, Lilia Boeri and Tanusri Saha-Dasgupta.
   Phys. Rev. B 95 (2017) 184106.

3. *Properties at the interface of graphene and Ti_2C MXene*
   Pallabi Paul, Poulami Chakraborty, Tilak Das, Dhani Nafday and Tanusri Saha-Dasgupta.
   Phys. Rev. B 96 (2017) 035435.

4. *MXene: A New Trend in 2D Materials Science*
   Poulami Chakraborty, Tilak Das and Tanusri Saha-Dasgupta.
   Chapter 10414, Comprehensive Nanoscience and Nanotechnology, 2nd edition.
   (to be published)

5. *Soft MAX phases with Boron-substitution: A Computational Prediction*
   Poulami Chakraborty, Aurab Chakrabarty, Amlan Dutta and Tanusri Saha-Dasgupta.
   (communicated)

Contents

List of Figures

Chapter 1

Introduction

Materials are probably more deep-seated in our culture than most of us realize. Transportation, housing, clothing, communication, recreation, and food production virtually every segment of our everyday life is influenced by one or other material aspect. Historically, the development and advancement of societies have been intimately tied to our ability to produce and manipulate materials to our needs. The history of human civilization evolved from the Stone Age to the Bronze Age, the Iron Age, the Steel Age, and to the Space Age (simultaneous with the Electronic Age). Each age is marked by the advent of certain materials. The Iron Age brought tools and utensils. The Steel Age brought railroads, instruments, and the Industrial Revolution. The Space Age brought the materials for stronger and light structures (e.g., composite materials). The Electronic Age brought semiconductors, and thus many varieties of electronic gadgets. Thus there has been a need for human and material resources for centuries, which still is going strong. In summary, materials constitute foundation of technology.

Materials with certain specific set of properties which make them useful in the field of engineering are termed as engineering materials. As engineering materials constitute foundation of technology, its not only necessary but a must to understand how materials behave like they do and why they differ in properties. This is only possible with the atomistic understanding allowed by quantum mechanics that first explained atoms and then solids starting in the 1930s. The combination of physics, chemistry, engineering and the focus on the relationship between the properties of a material and its microstructure is the domain of Materials Science.

Specifically, the mechanical properties of materials, the properties in focus of this thesis are of crucial importance for technological applications. However, till recent time, efforts in understanding mechanical properties of materials have been based mainly on phenomenological and empirical concepts and approaches. On the other hand, the underlying theory for the study of physics of materials at the atomic scales is quite well established. First-principles techniques based on quantum density functional theory (DFT) allow material-specific understanding of local structural and electronic properties at the ground state. What is needed is connecting the details of electronic-structure calculations at the atomic scale to the macroscopic behaviour of materials, as observed in experiments. Following this spirit, the present thesis attempts to study the mechanical behaviour in three technologically important classes of materials starting from microscopic description.

1.1 Technologically important materials

The development and application of new materials involve a close interplay of their physical and chemical properties with their structure. Many new materials are predicted theoretically and their structure and properties are analysed. But they actually gain technological importance, once the structure-property relations are verified through experiments and used for large scale productions in industry. There are numerous examples of such technologically important materials, we mention only few of them to set the background.

Silicon (Si) is perhaps the most prominent example, which is a versatile material with applications ranging from semiconductors and electronic devices to glass fabrication processes. Silicon can assume various forms and can mix with other elements to create silicon-rich compounds. Silicon alloys are often used to manufacture large automotive parts, while pure silicon is used in sensitive electronics applications. Silicon Carbide (SiC), which is the only chemical compound of carbon and silicon, has been used repeatedly in electronic devices and MicroElectro-Mechanical Systems (MEMS) due to its capability of operating at high power levels and high temperatures. It serves as an ideal material for applications that require superior hardness, high thermal conductivity, low thermal expansion, chemical and oxidation resistance. The performance of SiC due to its high-temperature, and high-power capabilities makes it suitable for aircraft, automotive, communications, power, and spacecraft industries. These specific industries are starting to take advantage of the benefits of SiC in electronics. SiC films are used as high temperature semiconductors [21, 22].

Another material having wide range applications is GaAs. The uses of GaAs are varied, they are used in diodes, field-effect transistors (FETs), and integrated circuits (ICs). GaAs components are useful in ultra-high radio frequencies and in fast electronic switching applications. The benefit of using GaAs in devices is that it generates less noise than most other types of semiconductor components and, as a result, is useful in weak-signal amplification applications. Due to its higher saturated electron velocity, electron mobility and breakdown voltages it is often used in electronics, optics, and photovoltaics.

Since the discovery of 'wonder material' graphene, 2D materials have received much focus and attention. There has been a lot of research in order to commercialize the production of 2D materials since they exhibit remarkable properties that can be exploited in a range of applications, for example graphene is found to be an excellent electronic and thermal conductor. It has a record thermal conductivity, a very high intrinsic mobility and a high current density. Its surface is chemically inert with low surface energy and no out-of-plane dangling bonds. Graphene like materials discovered recently named MXene are known for its versatile properties that complement those of graphene. For example, they have a wide range of bandgaps as opposed to graphene, where the bandgap is absent.

The materials introduced in the following section have the potential for wide range of applications due to their various properties which can be modified and tuned, detailed study of which will be presented in this thesis.

1.2 Materials discussed in the Thesis

1.2.1 Zirconium Hydrogen System

The transition metal zirconium is found abundantly in nature, contained primarily in the naturally occurring ore zircon. The high melting point, good high temperature mechanical properties combined with a considerable resistance to corrosion in a variety of environments makes zirconium and its alloys a very attractive material to a number of major industries. In light engineering, zirconium can be found as the getter in vacuum tubes, like those used in electron guns, where its high affinity for gasses, including oxygen and nitrogen, allows it to increase and maintain the level of vacuum. The chemical industry, for example, has been known to use commercial grade zirconium alloys in the manufacturing of valves, centrifugal pumps, pressure vessels, reactors, agitators, piping and heat exchangers [23]. These adoptions can be easily attributed to the discussed resistance of zirconium to corrosive media, as well as the stability of mechanical properties demonstrated at elevated temperatures, which may be necessary during certain stages of chemical processing. Despite this, the largest consumer of zirconium is undoubtedly the nuclear industry.

Hydrogen is another material present abundantly on Earth. Hydrogen has some unique features, namely small atomic size and mass, medium electronegativity and the ability to react with various elements. The hydrogen atom can easily penetrate an interstitial site in a metal lattice due to its small size. Depending on the electronegativity of the two atoms, hydrogen can form wide range of bonds with different elements.

Hydrogen solute atoms have a deleterious effect on the structural integrity of many transition metals. This has resulted in an abundance of research into the effect of H on metals on many length scales. The presence of hydrogen in certain metals such as Hf, Ti and Zr based alloys is a major cause of embrittlement due to precipitation of hydrides (MH_x). The absorption of hydrogen results in a degradation of mechanical properties, known as hydrogen embrittlement. As discussed previously, Zr is widely used in the nuclear industry as fuel cladding due to its unique set of mechanical properties. Henceforth, there have been several studies aimed at understanding hydrogen related failures that occurs in light water reactor fuel cladding materials, which can lead to the failure of the barriers to fission product (radio-toxic material) release. A schematic representation of the Pressurised Water Reactor which is a type of light water reactor is presented in Fig. 1.1, where the fuel cladding made of Zr-based alloys. In order to improve

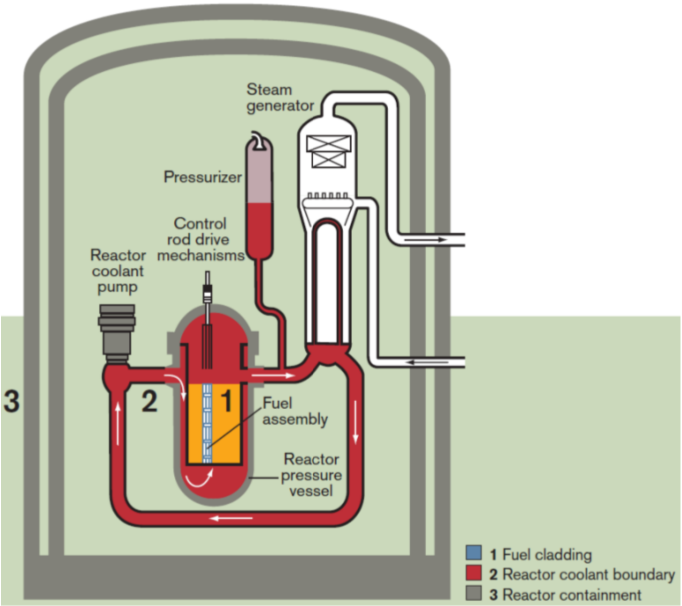

Figure 1.1: Schematic representation of the three safety barriers in a Pressurised Water Reactor (PWR). Figure adapted from Ref. [1]

efficiency of nuclear reactors and minimise nuclear waste produced during operation, it is necessary to optimise fuel usage without compromising safety. This requires a complete physical understanding of how the manufacturing route affects the performance of the cladding and the mechanisms that determine the degradation during in-reactor performance.

The equilibrium phase diagram for zirconium consists of the following phases:

- αZr - the hcp solid solution, P6_3/mmc space group, with maximum hydrogen solubility of 5.9 at.%H at 550°C. The Zr hcp lattice has tetragonal and octagonal positions available for hydrogen to occupy. Depicted in Fig. 1.2(a), the unit cell consists of two Zr atoms.

- βZr - the bct solid solution, Im$\bar{3}$m space group. Body-centered tetragonal (bct) structure has Zr atoms occupying all bcc positions, but in a tetragonally deformed bcc lattice to accomodate hydrogen atoms on the edge of the unit cell. Similar to αZr, the unit cell consists of two Zr atoms.

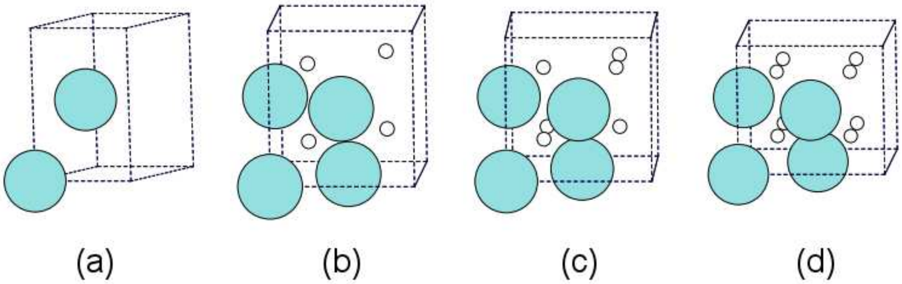

Figure 1.2: The unit cells for (a) αZr, (b) γ-ZrH, (c) δ-$ZrH_{1.5}$, (d) ϵ-ZrH_2. Figure adapted from Ref. [2]

- γZr - the fct γ metastable phase, of the $P4_2/n$ space group, with ratio $c/a > 1$ and composition of ZrH. γZr is the only zirconium hydride that has the stoichiometric composition. Different arrangements of hydrogen atoms inside the fcc lattice are depicted in Fig. 1.2(b).

- δZr - the fcc phase, fluorite structure of the $Fm\bar{3}m$ space group, is the most common hydride with the composition of around $ZrH_{1.6}$. The unit cell consists of four fcc unit cell Zr atoms as shown in Fig. 1.2(c).

- ϵZr - the fct, face-centered tetragonal or distorted fluorite structure, of the I4/mmm space group, which actually represents a bct lattice type. The fct ϵ phase, has an axial ratio $c/a < 1$ and the composition of around ZrH_2. The face-centered tetragonal lattice is shown in Fig. 1.2(d).

- ζZr - the hcp ζ metastable/transient phase has been reported with probable stoichiometric composition Zr_2H in Zircaloy-4 alloys. This hydride has a hexagonal lattice and belongs to the trigonal crystal system with the space group P3m1.

The general aim of research in this field is to understand the underlying mechanisms responsible for the microstructure evolution during processing and degradation modes during performance. The hexagonal close packed crystal structure of Zr makes the understanding of deformation mechanisms and the aim of predicting microstructure evolution during processing particularly challenging. Current research efforts have been dedicated towards developing crystal plasticity models that will be able to predict texture evolution during processing. In order to study these factors it is necessary to introduce microscale simulations by Molecular Dynamics (MD), which is expected to provide understanding of formation of hydrides in zirconium and the changes it inflicts on mechanical properties. Study of H embrittlement in Zr is presented in Chapter 3 where we have looked into the degrading effect of H in Zr, dilute and concentrated limit of H incorporation.

1.2.2 MAX phases

The terminology MAX refers to a new class of solids having the general formula $M_{n+1}AX_n$ ($n = 1, 2, 3$) where M represents an early transition metal, A is an A-group element, and X is carbon or nitrogen [24, 25]. These layered ternary transition-metal carbides and nitrides form three main groups, M_2AX, M_3AX_2, and M_4AX_3, depending on the choice of n. A vast amount of experimental and theoretical studies have been devoted to the study of MAX phases due their extraordinary mechanical, physical, and chemical properties [26, 27, 28, 29, 30]. Similar to their corresponding binary carbides and nitrides (MX), the MAX phases are elastically stiff, good thermal and electrical conductors, resistant to chemical attack, and have relatively low thermal expansion coefficients. Strikingly, however they are quite distinct from binary carbides and nitrides in terms of their mechanical properties. MAX phases are relatively soft compared to MX and most are readily machinable, thermal shock resistant and damage tolerant [25, 31]. Moreover, some MAX compounds are fatigue, creep, and oxidation resistant. At room temperature, they can fully recover upon removal of the load when subjected to stresses as high as 1 GPa. Furthermore, at higher temperatures, they undergo a brittle-to-plastic transition (BPT) [32].

All MAX phases crystallize in the layered and hexagonal structure with the space group of P63/mmc (194). The unit cells of the MAX phases are characterized by M_6X octahedra with the X atoms filling the octahedral sites between the M atoms (c.f. Fig. 1.3), which are identical to those found in the rock salt structure of the MX binaries. The A-group elements are located at the centres of trigonal prisms, which are larger than the octahedral sites so as to accommodate

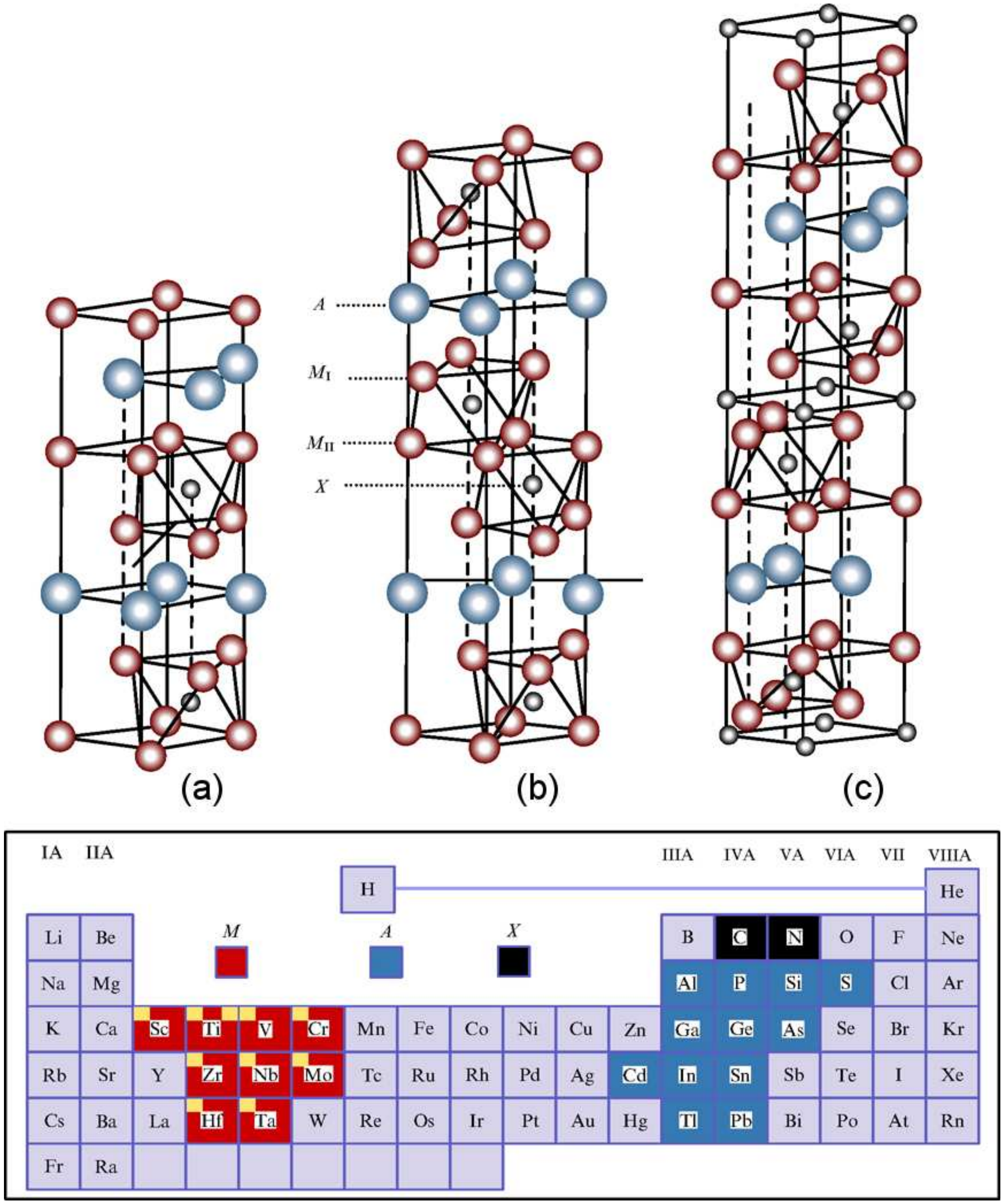

Figure 1.3: Unit cells of the phases (a) M_2AX, (b) M_3AX_2, and (c) M_4AX_3. The periodic table shows the M, A and X elements that form the MAX phases. Figure adapted from Ref [3]

the larger A atoms. As listed in the table shown in Fig. 1.4, there are over 60 MAX phases synthesized to date. A majority are 211 phases ($n = 1$) while Ti_2AlC and Ti_3SiC_2 are the most well known and most studied [33, 34]. Although the higher order MAX phases such as 514 [35], 615 [36], and 716 [37] have been made, no pure bulk samples are successfully synthesized and characterized to date. In addition, the hybrid structure that can be described as intergrowth of two known MAX phases (211, 312, and 413) has been synthesized, such as $Ti_5Si_2C_3$ [35], $Ti_7Si_2C_5$ [35], and $Ti_5Al_2C_3$ [38, 39].

Bonding in MAX phases is a combination of metallic, covalent and ionic bonds. The M and X atoms form strong directional covalent bonds in the MX layers that are comparable to those of the corresponding MX binaries. The M-d-M-d metallic bonding dominates the electronic density of states at the Fermi level, N(E_F). In most MAX phases, the M-A bonds are relatively weaker than the M-X bonds which is partly ionic, partly covalent. The most intriguing aspect about this class of materials is the ease with which the chemistry can be changed while maintaining the same crystal structure. They have been routinely synthesized as bulk and as thin films, and are found to exhibit exceptional physical, chemical, electrical and mechanical properties, the reason being the inherently laminated structure, and a mixture of strong M-X bonds and weaker M-A bonds.

Experimental evidence of magnetic MAX phases were first reported in 2013. Their laminated character makes them an ideal model system for the study of the complex magnetic phenomena that occur in atomically layered materials, extending beyond traditional ferromagnetic (FM), antiferromagnetic (AFM), and paramagnetic (PM) order. The first predicted stable magnetic MAX phase to be synthesized was $(Cr_{1-x}Mn_x)_2AlC$. Theoretically, a chemically ordered structure with Mn-C-Mn-Al-Cr-C-Cr-Al layer stacking along the c-direction was identified as the low energy structure, with FM ordered Mn layers coupled via nearly non-magnetic Cr layers. The degree of intermixing between Cr and Mn layers was also addressed as a possible route to tune the sign and magnitude of the coupling. Later theoretical predictions include $(Cr_{1-x}Mn_x)_2GeC$, which was shown to be stabilized by Cr/Mn disorder and related configurational entropy upon an increased temperature. MAX phases that have been studied experimentally in terms of magnetic characteristics are Cr_2AC and $(Cr,Mn)_2AC$ where A= Al, Ge,

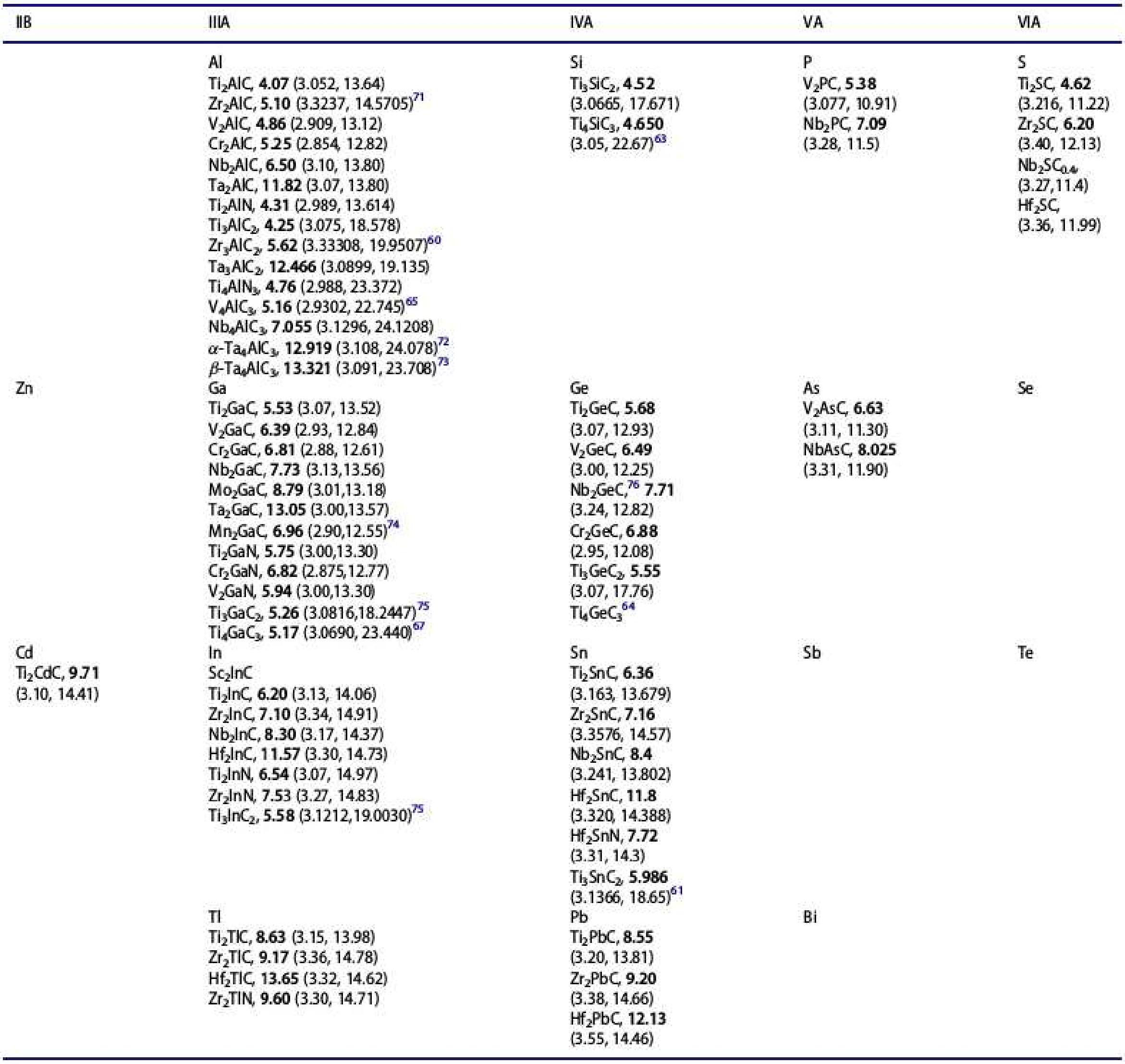

IIB	IIIA	IVA	VA	VIA
	Al Ti_2AlC, **4.07** (3.052, 13.64) Zr_2AlC, **5.10** (3.3237, 14.5705)[71] V_2AlC, **4.86** (2.909, 13.12) Cr_2AlC, **5.25** (2.854, 12.82) Nb_2AlC, **6.50** (3.10, 13.80) Ta_2AlC, **11.82** (3.07, 13.80) Ti_2AlN, **4.31** (2.989, 13.614) Ti_3AlC_2, **4.25** (3.075, 18.578) Zr_3AlC_2, **5.62** (3.33308, 19.9507)[60] Ta_3AlC_2, **12.466** (3.0899, 19.135) Ti_4AlN_3, **4.76** (2.988, 23.372) V_4AlC_3, **5.16** (2.9302, 22.745)[65] Nb_4AlC_3, **7.055** (3.1296, 24.1208) α-Ta_4AlC_3, **12.919** (3.108, 24.078)[72] β-Ta_4AlC_3, **13.321** (3.091, 23.708)[73]	Si Ti_3SiC_2, **4.52** (3.0665, 17.671) Ti_4SiC_3, **4.650** (3.05, 22.67)[63]	P V_2PC, **5.38** (3.077, 10.91) Nb_2PC, **7.09** (3.28, 11.5)	S Ti_2SC, **4.62** (3.216, 11.22) Zr_2SC, **6.20** (3.40, 12.13) $Nb_2SC_{0.4}$, (3.27,11.4) Hf_2SC, (3.36, 11.99)
Zn	Ga Ti_2GaC, **5.53** (3.07, 13.52) V_2GaC, **6.39** (2.93, 12.84) Cr_2GaC, **6.81** (2.88, 12.61) Nb_2GaC, **7.73** (3.13,13.56) Mo_2GaC, **8.79** (3.01,13.18) Ta_2GaC, **13.05** (3.00,13.57) Mn_2GaC, **6.96** (2.90,12.55)[74] Ti_2GaN, **5.75** (3.00,13.30) Cr_2GaN, **6.82** (2.875,12.77) V_2GaN, **5.94** (3.00,13.30) Ti_3GaC_2, **5.26** (3.0816,18.2447)[75] Ti_4GaC_3, **5.17** (3.0690, 23.440)[67]	Ge Ti_2GeC, **5.68** (3.07, 12.93) V_2GeC, **6.49** (3.00, 12.25) Nb_2GeC,[76] **7.71** (3.24, 12.82) Cr_2GeC, **6.88** (2.95, 12.08) Ti_3GeC_2, **5.55** (3.07, 17.76) Ti_4GeC_3[64]	As V_2AsC, **6.63** (3.11, 11.30) NbAsC, **8.025** (3.31, 11.90)	Se
Cd Ti_2CdC, **9.71** (3.10, 14.41)	In Sc_2InC Ti_2InC, **6.20** (3.13, 14.06) Zr_2InC, **7.10** (3.34, 14.91) Nb_2InC, **8.30** (3.17, 14.37) Hf_2InC, **11.57** (3.30, 14.73) Ti_2InN, **6.54** (3.07, 14.97) Zr_2InN, **7.53** (3.27, 14.83) Ti_3InC_2, **5.58** (3.1212,19.0030)[75]	Sn Ti_2SnC, **6.36** (3.163, 13.679) Zr_2SnC, **7.16** (3.3576, 14.57) Nb_2SnC, **8.4** (3.241, 13.802) Hf_2SnC, **11.8** (3.320, 14.388) Hf_2SnN, **7.72** (3.31, 14.3) Ti_3SnC_2, **5.986** (3.1366, 18.65)[61]	Sb	Te
	Tl Ti_2TlC, **8.63** (3.15, 13.98) Zr_2TlC, **9.17** (3.36, 14.78) Hf_2TlC, **13.65** (3.32, 14.62) Zr_2TlN, **9.60** (3.30, 14.71)	Pb Ti_2PbC, **8.55** (3.20, 13.81) Zr_2PbC, **9.20** (3.38, 14.66) Hf_2PbC, **12.13** (3.55, 14.46)	Bi	

Figure 1.4: List of $M_{n+1}AX_n$ phases known to date. The bold text is theoretical density, the numbers in parentheses are lattice parameters a and c. Table adapted from Ref [4]

Ga. The high stability of Mn_2GaC motivates alloying this phase with others elements, beyond Cr, to study the effect of composition on the magnetic properties.

The physical properties of the MAX phases, such as thermal expansion, elastic properties, and thermal conductivity, have much in common with their respective MX binaries [40]. However, the electronic structure and transport properties of the MAX phases are more similar to those of the transition metals [40]. The ease of machinability is one of the most characteristic feature which sets them apart from other structural ceramics or high-temperature alloys [41, 42, 43]. Very recently, bulk superconductivity is reported in Ti_2GeC at 9.5 K [44]. To date, bulk superconductivity has been discovered for seven systems: Mo_2GaC [45], Nb_2SC [46], Nb_2SnC [47], Nb_2AsC [48], Ti_2InC [49], Nb_2InC [50], and Ti_2InN [51]. Due to the unique blend of properties MAX phase compounds have a wide range of possible technological and engineering applications.

Theoretical studies related to MAX phase properties are numerous [52, 53, 54] but they are mostly first-principles calculations which investigate the electronic structure, bonding and other microscopic phenomenon. However, in comparison to experimental studies, there are very few computational studies to evaluate the mechanical and structural aspects of these unique set of compounds. Since they have a layered structure, the study of dislocations and their mobility with temperature and strain can be an effective way of analysing deformation behaviour of such layered structures. This motivated us to study the mechanical properties of V_2AlC and the proposed V_2AlB compound, obtained by replacing C by B which will be discussed in Chapter 4.

1.2.3 MXenes

Two dimensional (2D) materials are defined as solid crystals consisting of single or few layers of atoms having typical thickness of 1-10Å, and lateral dimension of tens of microns. In the post graphene era, search of new 2D materials has become an active field of research due to the unusual properties exhibited by them. 2D or quasi-2D structures that contain more than one element may offer new properties because they provide a larger number of compositional variables that can be tuned for achieving specific properties. This ever expanding list includes 2D materials like *h*-BN [55], metal chalcogenides [56], holey carbon [57], graphane [58] etc. This excitement has been shared by the recent findings on new family of quasi-2D materials [59], named MXene which are formed by early transition metals and carbon or/and nitrogen. MXenes are 2D structures derived from MAX phases. Unlike graphite and other layered structures where layers are held together by van der Waals forces, MAX phases are characterized by combination of different bonding characters; while the M-X bonds are strong directional covalent bonds, M-A bonds are relatively weaker than covalent M-X bonds, M-M bonding being of metallic nature. M-A bonds are thus too strong to be broken by shear/mechanical means. MXenes are therefore produced from MAX phases via selective etching of the A layers by chemical methods. The nomenclature MXene comes from metal (M) and carbon and/or nitrogen (X) along with the *ene* from the family of 2D materials like graphene, silicene, or germanene etc. [60]. For instance, Al atom from Ti_3AlC_2 can be selectively etched by using aqueous HF to form Ti_3C_2. Since different Ti_3C_2 layers are bonded together with Al atoms, loss of Al from Ti_3AlC_2 weakens the force between different Ti_3C_2 layers. This results in the formation of thin sheets/layers whose thickness is typically a few atomic layers thick (less than 1 nm). Today about 70+ examples of MXene compounds are found either by experimental synthesis or predicted in theory, as shown in Figure. 1.5. Because the n values for the existing $M_{n+1}AX_n$ phases can vary from 1 to 3, the corresponding single MXene sheets consist of 3, 5 or 7 atomic layers for M_2X, M_3X_2 and M_4X_3, respectively (cf Fig. 1.5). With a goal to tailor properties of this exciting class of 2D materials, solid solution phases with mixed M-site or X-site MXenes have also been synthesized in experiment or predicted in theory in some cases, as included in Fig. 1.5.

The resulting 2D compounds exhibit combination of excellent conductivity properties, thermal stability, mechanical properties [61, 62, 63, 64, 65]. MXenes have been discussed as potential candidates for Li-ion battery anodes and as a hydrogen storage medium [66, 67]. For practical application of 2D materials, flexibility is an issue to be considered which is related to mechanical properties. Thus tailoring of mechanical properties by solid solutions or through construction of heterostructures is an effective way for improved performance in flexible devices.

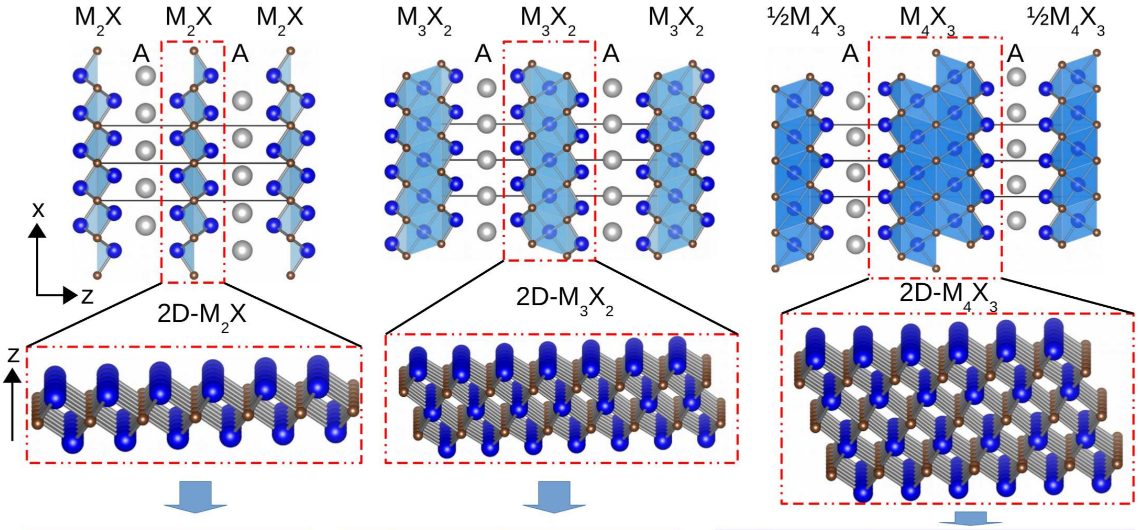

M_2X	Synthesis	Theory
M_2C	Ti_2C, Sc_2C, V_2C, Cr_2C, Mo_2C, W_2C, Zr_2C, Ta_2C, Nb_2C, Hf_2C,	Ti_2C, Sc_2C, V_2C, Cr_2C, Mo_2C, W_2C, Zr_2C, Ta_2C, Nb_2C, Hf_2C,
M_2N	Ti_2N, V_2N, W_2N, Cr_2N, Mo_2N, Zr_2N, Nb_2N, Ta_2N, Hf_2N,	Ti_2N, V_2N, Sc_2N, Cr_2N, Mo_2N, W_2N, Zr_2N, Ta_2N, Hf_2N,
Mixed	$(Ti,V)_2C$, $(Ti,Nb)_2C$,	$^{a}(Ti,V)_2C$, $^{a}Ti_2(C,B)$,

M_3X_2	Synthesis	Theory
M_3C_2	Ti_3C_2, Sc_3C_2, V_3C_2, Zr_3C_2, Mo_3C_2, Ta_3C_2, Hf_3C_2,	Ti_3C_2, Sc_3C_2, V_3C_2, Cr_3C_2, Zr_3C_2, Mo_3C_2, Nb_3C_2, Ta_3C_2,
M_3N_2	$^{d}Ti_3N_2$ $^{d}Ta_3N_2$	Ti_3N_2, $^{e}Sc_3N_2$, $^{f}V_3N_2$, Cr_3N_2, Ta_3N_2, Nb_3N_2, Zr_3N_2,
Mixed	$(Ti,V)_3C_2$, $(Cr,V)_3C_2$, $(Ti,Cr_2)C_2$, $(Ti,Mo_2)C_2$, $^{b}(Sc,Mo_2)C_2$, $Ti_3(C,N)_2$,	$(Ti_2,Ta)C_2$, $(Ti,Cr_2)C_2$, $(Ti_2,Nb)C_2$, $(Ti,Mo_2)C_2$, $(V,Mo_2)C_2$, $(V,Cr_2)C_2$, $(Nb,Cr_2)C_2$, $(Ta,Mo_2)C_2$, $(Ta,Cr_2)C_2$, $(Nb,Mo_2)C_2$, $^{c}(Sc,Mo_2)C_2$,

M_4X_3	Synthesis	Theory
M_4C_3	$^{d}Ti_4C_3$, $^{d}V_4C_3$, Nb_4C_3, Ta_4C_3,	$^{i}Ti_4C_3$, $^{k}Sc_4C_3$, V_4C_3, $^{g}Mo_4C_3$, $^{j}Zr_4C_3$, Nb_4C_3, Ta_4C_3,
M_4N_3	Ti_4N_3, $^{h}V_4N_3$, Ta_4N_3,	Ti_4N_3, Sc_4N_3, $^{h}V_4N_3$, $^{h}Cr_4N_3$,
Mixed	$(Ti,Nb)_4C_3$, $(Ti_2,Mo_2)C_3$, $(Zr,Nb)_4C_3$,	$(Ti_2,V_2)C_2$, $(Ti_2,Ta_2)C_3$, $(Ti_2,Nb_2)C_3$, $(Ti_2,Cr_2)C_2$, $(Ti_2,Mo_2)C_2$, $(V_2,Cr_2)C_2$, $(V_2,Mo_2)C_2$, $(V_2,Nb_2)C_2$, $(V_2,Ta_2)C_2$, $(Nb_2,Ta_2)C_2$, $(Nb_2,Cr_2)C_2$, $(Nb_2,Mo_2)C_2$, $(Mo_2,Ta_2)C_2$, $(Cr_2,Ta_2)C_2$,

Figure 1.5: 2D M_2X, M_3X_2 and M_4X_3, formed from 3D $M_{n+1}AX_n$ phase with n = 1, 2 and 3, by removal of A element. The M, A and X sites are denoted by large blue, large grey, small brown balls, respectively. Possible examples for each of the three classes which have been either synthesized experimentally or predicted in theoretical studies, are tabulated at the bottom of the figure. The examples are taken from a) Ref [5], b) Ref [6], c) Ref [7], d) Ref [8], e) Ref [9], f) Ref [10], g) Ref [11], h) Ref [12], i) Ref [13], j) Ref [14], k) Ref [9] the rest being taken from Ref [15]. Figure adaptad from Ref [16]

MXenes are unique among the family of 2D materials because a) they manifest the properties of ceramics which make them chemically and mechanically stable b) they can be of single unit thickness consisting of M-X-M tri-layer, or of several units thick, c) thickness of the single unit MXene, i.e M_2X can be tuned which makes them suitable materials to study the effects of quantum confinement. Along with experimental studies, theoretical techniques such as density functional theory (DFT) and to a lesser extent, molecular dynamics simulations, have been extensively applied to understand and predict properties, to identify potential applications guiding much of the experimental research in the field of MXenes [61, 62, 68, 69] specifically their electronic, magnetic and elastic properties.

The 2D layered MXene has hexagonal space group ($P6_3/mmc$, No.194) symmetry, with generic chemical formula of $M_{n+1}X_nT$, where T denotes the surface termination by H, -OH, or F which may happen during the acid etching and sonication procedure followed during the synthesis. In the MXene structure the hexagonal layer of X sites are sandwiched between two M layers and the number of $(MX)_n$-layers are one, two, and three for M_2X, M_3X_2, M_4X_3 class of MXenes.

The electronic properties of MXenes are of special interest as they can, in principle, be tuned by changing the MXene elemental composition and/or their surface terminations. The bandstructure and electron density of states (DOS) of MXene have been extensively studied by DFT. The M-d M-d metallic bonding character dominate the states near Fermi level, resulting in a metallic solution. It is important to mention here, the situation may change dramatically in presence of surface termination. While MXenes with termination free surfaces, M_2C (M = Sc, Ti, V, Cr, Zr, Nb, or Ta) and M_2N (M = Ti, Cr, or Zr) are predicted to be metallic,[10, 70] where the surfaces are passivated by F, O or OH functional groups, the metallicity may found to be vanished. For example Sc_2CF_2, $Sc_2C(OH)_2$, Sc_2CO_2, Ti_2CO_2, Zr_2CO_2, and Hf_2CO_2, are predicted to be semiconductors [70]. According to DFT calculations [70], the surface passivated MXenes Ti_2CO_2, Zr_2CO_2, Hf_2CO_2 , Sc_2CF_2, $Sc_2C(OH)_2$ and Sc_2CO_2 are semiconductors with energy gaps of 0.24, 0.88, 1.0, 1.03, 0.45 and 1.8 eV respectively. $Sc_2C(OH)_2$ is a direct band-gap semiconductor, whereas all other systems are found to be indirect band-gap semiconductors. Among all theoretically studied MXenes, only electronic properties of Ti_2C, Ti_3C_2, Mo_2C, Mo_2TiC_2 and $Mo_2Ti_2C_3$ with mixed terminations have been experimentally measured [71, 72, 73, 74, 75, 76, 77].

The high value of DFT computed non spin polarized density of states at the Fermi level, may indicate magnetic instability. According to the standard approach of Stoner theory [78], the stability of magnetic states is given by N(0) $> 1/I$, where N(0) is the density of states at E_F and I is the Stoner parameter. Plugging in the Stoner parameter values of the M site in MXene, several of them is expected to be magnetic. Considering the magnetism of metal atom, one may expect different possible arrangement of TM spins within the single unit MXene structure. It can be ferromagnetism (FM) with parallel alignment of all TM spins, or it can be antiferromagnetism (FM) of A-type, C-type of G-type, In case of A-type, the intra layer TM spins are aligned parallely, while those between the layers are aligned in an antiparallel manner. The reverse is true for C-type AFM with intra layer TM spins aligned antiparallely and TM spins between layers aligned parallely. For G-type AFM, the metal spins are aligned antiparallely in all directions.

It was first reported by Khazaei et al. that Cr_2C and Cr_2N MXenes have lower ground-state energy for ferromagnetic configurations compared to nonmagnetic configurations [70]. The difference between magnetic ground states for O-terminated carbide and nitride MXenes arises due to the extra electron from nitrogen. Recently, Si et al. [79] have shown that unpassivated Cr_2C MXene is a ferromagnetic half-metal, characterized by the existence of metallic transport behavior for one spin channel and insulating behavior for the other. It is worth mentioning that materials with such a transport behavior are highly desired for next-generation spintronic devices such as spin filters, spin-polarized FET, spin injectors, and magnetic sensors [80, 81].

While the unpassivated MXenes have been studied for their magnetic behavior, similar studies have been extended to passivated MXene compounds as well. Depending on the nature of M, X and the passivating agent, the magnetic behavior is found to be different. In a recent study [59], five different nitride MXenes (Mn_2NF_2, Mn_2NO_2, $Mn_2N(OH)_2$, Ti_2NO_2, and Cr_2NO_2) have been found with FM ground states. In comparison, their carbide counterpart Mn_2C MXenes, are reported to exhibit FM ground state for F/OH- terminations, but AFM ground state for O-terminations [82]. Similarly the carbide counterpart of Ti_2NO_2 is found to be nonmagnetic, which might suggest that nitride MXenes may be more viable as materials with net moment. Other passivated MXenes with FM ground states include Cr_2NO_2 and Ti_2NO_2. While a large fraction of the surface-terminated MXenes have been predicted to have AFM ground states, the mixed surface termination is seen to produce ferromagnetic and related half-metallicity properties. The current synthesis methods, which usually produce mixed surface termination groups, therefore is expected to produce a large variety of ferromagnetic, half metallic MXene.

One of the key properties of 2D materials is the mechanical flexibility, which means deformability under strain. A good measure of mechanical flexibility, is the stress-strain relation. For 2D materials, the strain can be bi-axial or uni-axial. The slope of the stress-strain curve for small strain value provide estimate of elastic moduli like in plane stiffness, Young's moduli. The slope was found (Ref. our paper) to be the same for the zig-zag and arm-chair uniaxial loading, suggesting MXenes are nearly isotropic, as opposed to dichalcogenides like MoS_2[83]. Such study of elastic and mechanical properties of Ti_2C MXene was done in Chapter 5, where the effect of Boron and Vanadium doping was considered at the X and M site respectively. During experimental synthesis of MXenes, they are passivated by several functional groups, so in our study we also considered the oxygen passivated Ti_2C.

The 2D morphology of MXene family, combined with their attractive transport and magnetic properties may be beneficial for integration with other layered materials in vertical hybrid heterostructure geometries. Formation of such heterostructure may be used to modify the electronic properties of other 2D materials. This may also allow for new functionality at the interface of the two, rendering conceptually new degree of flexibility in designing novel electronic devices. To date, only minimal experimental studies have been carried out in this promising area. One of recent theoretical study based on DFT reports properties at interface of transition metal dichalcogenide (TMD) and MXene [84]. Since graphene and MXene, both materials are of high technological interest, we studied the heterostructures of graphene/Ti_2C MXene in Chapter 6. We also explored the possibilities of heterostructuring between graphene and Ti_2CO_2.

1.3 Overview of present thesis

It is apparent from the several examples presented in the previous sections that diverse classes of systems show a variety of properties which are not completely understood at the microscopic level. Therefore, in order to have a better understanding and a deeper insight, we have used the first principles calculations focusing primarily on mechanical properties together with other properties like electronic and magnetic. The understanding at the microscopic level opens up new avenues for the design of novel functional materials. We have also made use of molecular dynamic simulation based on classical potential in order to study large length scale property which is beyond the scope of density functional theory. The contents of the various chapters discussed in the present thesis have been organized as follows :

- **Chapter 2**: In this chapter, we discuss the theoretical methodology of our calculations. This includes both the theoretical background of DFT and its practical implementation. In connection to later, we discussed the different basis sets which we have considered during the course of calculation, depending upon the properties we have studied. We also discussed tools beyond the zero temperature DFT such as classical molecular dynamics simulation.

- **Chapter 3**: In this chapter the degradation properties of the nuclear reactor material Zr has been studied. Using large scale atomistic simulation, the deleterious effect of H in the two phases of Zr has been investigated. Our study revealed that the deformation caused by H follows different mechanism depending on the concentration of H.

- **Chapter 4**: In this chapter the effect of Boron substitution has been studied in a class of transition-metal ternary-layered carbides and nitrides commonly known as MAX phases. The effect of boron-substitution on plastic deformation properties of a typical MAX phase compound,V_2AlC was extensively studied using first-principles density functional theory calculations, combined with continuum modeling to access the core structure of dislocations.

- **Chapter 5**: This chapter deals with ternary carbides and nitrides termed MXenes. It discusses the possible routes through which the mechanical and electronic properties of this class of 2D materials can be tailored. In particular, the effect of substitutional doping with Boron and Vanadium on the electronic, magnetic and elastic properties of Ti_2C MXene and its oxygen passivated counterparts has been studied.

- **Chapter 6**: This particular chapter explores the possibility of bringing together graphene and Ti_2C to form heterostructures. Here all possible stacking arrangements have been explored and studied in order to provide a comprehensive outlook. We studied the effect of stacking on the nature of bonding, electronic density of states as well as the local magnetic moments. Formation of such heterostructure interestingly is found to give rise to chemically bonded heterostructures influencing drastically the magnetic and electronic properties of individual components, as opposed to commonly observed vander Waals heterostructures of 2D materials.

- **Chapter 7**: This chapter provides a summary of all the studies presented in this thesis. In addition, scope of future work has been discussed. In particular, this involves a discussion on the development of semi-empirical potential for ternary carbide V_2AlC and other MAX phases, which should be an useful basis for some of the planned future work.

Chapter 2

Computational Methods

In this chapter we discuss the different methods and techniques used in this thesis. We have used density functional theory (DFT) and molecular dynamic (MD) simulations depending on the need of the problems addressed in this thesis. In the following, we start with the discussion of the many-body Hamiltonian, and subsequently provide details of the various methods of DFT that have been used for the studies presented in the thesis. Following this, we present the technique of molecular dynamic simulation of model built based on classical pair potentials. We conclude this section with a brief introduction of the concept of continuum modeling in the final section of this chapter.

2.1 The Many-Body Hamiltonian

The microscopic description of the physical and chemical properties of matter is a complex problem. The matter can be molecules and clusters or a condensed solid phase. However, in all these cases it can be thought of as a collection of positively charged particles (nuclei) and negatively charged particles (electrons). If we have N_a nuclei surrounded by N_e electrons, then essentially we are dealing with a many-body problem. The many body Hamiltonian for any such system can be written in a generalized form as

$$\hat{H} = -\sum_{I}^{N_a} \frac{\hbar^2}{2M_I}\nabla_I^2 - \sum_{i}^{N_e} \frac{\hbar^2}{2m_i}\nabla_i^2 + \frac{e^2}{2}\sum_{I=1}^{N_a}\sum_{J\neq I}^{N_a} \frac{Z_I Z_J}{|R_I - R_J|} \tag{2.1}$$

$$+ \frac{e^2}{2}\sum_{i=1}^{N_e}\sum_{j\neq i}^{N_e} \frac{1}{|r_i - r_j|} - e^2 \sum_{I=1}^{N_a}\sum_{i=1}^{N_e} \frac{Z_I}{|R_I - r_i|} \tag{2.2}$$

where $\{R_I\}, I = 1, \cdots, N_a$ are the set of N_a nuclear coordinates and $\{r_i\}, i = 1, \cdots, N_e$ are the set of N_e electron coordinates. M_I and m_i are the nuclear and electron masses carrying charges Z_I and e respectively.

The Schrödinger's equation given by

$$\hat{H}\hat{\psi}(\mathbf{r}, \mathbf{R}) = E\hat{\psi}(\mathbf{r}, \mathbf{R}) \tag{2.3}$$

provides an exact description for the many-body system of electrons and nuclei, where $\hat{H}$ is the Hamiltonian of Eqn (2.1), $\mathbf{r} = \{r_i\}$ and $\mathbf{R} = \{R_I\}$ and $\hat{\psi}$ represents the total many-body wave-function. Therefore, it is expected that by solving the Schrödinger's equation within the full quantum mechanical framework, the characteristic properties of the system can be obtained. In reality, however, solving the Schrödinger's equation using either analytical methods or numerical approaches is non trivial since one has to deal with $3N_a + 3N_e$ coupled degrees of freedom which makes Eqn (2.1) very difficult to solve except for a few simple cases such as the isolated hydrogen atom. To simplify the above equation we need approximations such as the Born-Oppenheimer Approximation and Independent electron approximation that allow the full many-body wave-function $\hat{\psi}_n$ to be decoupled and hence makes Eqn (2.1) solvable in practice.

2.1.1 The Born-Oppenheimer Approximation

The Born-Oppenheimer approximation [85], aims to separate the electronic and nuclear degrees of freedom. The forces on both electrons and nuclei due to their electric charge are of the same order of magnitude, and so the changes which occur in their momenta as a result of these forces must also be the same. However, the nuclei are much more massive than the electrons, thus they must have much smaller velocities. Hence it is plausible that on the typical time-scale of the nuclear motion, the electrons will rapidly relax to the instantaneous ground-state configuration, so that in solving the time-independent Schrödinger's equation resulting from the Hamiltonian in equation 2.1, we can assume that the nuclei are stationary and solve for the electronic groundstate first, and then calculate the energy of the system in that configuration and solve for the nuclear motion. This separation of electronic and nuclear motion is known as the Born-Oppenheimer approximation. Following this, the many body Hamiltonian can be rewritten as

$$\begin{aligned} \hat{H} &= H_{electron} + H_{nuclei} && (2.4) \\ &= [\hat{T_e} + \hat{V_{ee}} + \hat{V_{ne}}] + [\hat{T_{nn}} + \hat{V_{nn}}] && (2.5) \end{aligned}$$

where $\hat{T_e}$ and $\hat{V_{ee}}$ are the kinetic and potential energy operators for the electrons, $\hat{V_{ne}}$ is the potential energy operator due to the interaction between electrons and nucleus, $\hat{T_{nn}}$ and $\hat{V_{nn}}$ are the kinetic and potential energy operators for the nuclei.

The key point is that the positions of the nuclei in $H_{electron}$ are no longer variables, but parameters, hence it is possible to solve the equations for the electronic Hamiltonian at a given time by assuming that the atomic coordinates are fixed. Hence, the nuclear-nuclear interactions can be assumed to be constant. A constant that is added to an operator only adds to the eigenvalues and has no effect on the eigenfunctions. The constant nuclear potential energy term $\hat{V_{nn}}$ is called Madelung energy and can be calculated classically. The Schrödinger equation using this approximations can be written as,

$$\hat{H}_{elec}\psi_{elec} = E_{elec}\psi_{elec} \tag{2.6}$$

The eigenfunctions are now the electronic wavefunction which explicitly depends on electronic coordinates, and parametrically on the nuclear coordinates, as does the electronic energy.

2.1.2 The Independent Electron Approximation

The ground state wavefunction can be determined by minimizing the total energy with respect to all the parameters in $\psi(r_i)$, with the constraint that ψ must obey the particle symmetry and conservation laws. The exact value of electron-electron Coulomb interactions, cannot be computed, and thus needs to be approximated. This assumes that the electrons behave as independent particles and replaces the effect of electron-electron interaction by an approximate mean field. There are two possible approaches, wave function based approach like Hartree and Hartree Fock and density based approach like Thomas Fermi and modern day density functional theory. In the following we discuss the details of density functional theory.

2.2 Density Functional Theory

Density functional theory (DFT) is one of the most successful approach to theoretical prediction of structures and properties of atoms, molecules and solids. It gives rather accurate description of the ground-state energy. This method is based on functional. The functional is a function which takes a value of a variable or variables and defines a single number from those variables. Here, the functional is the electron density. If we consider a system with N constituents, then the density depends only on three variables, i.e., the spatial coordinates x, y, z, instead of 3N (where every atom has three degrees of freedom), which makes calculations easier. Starting from this very idea Thomas and Fermi derived a differential equation for the density without any reference to the one electron orbitals (Thomas 1927, Fermi 1928). The basic idea was to replace the many-body wave-function $\psi(\mathbf{r})$ which is a function of 3N variables, N being the number of electrons, by the electron density $\rho(\mathbf{r})$ given by

$$\rho(\mathbf{r}) = N \int \psi(r_1, r_2, \cdots, r_N)\psi^*(r_1, r_2, \cdots, r_N) dr_1 dr_2 \cdots dr_N \tag{2.7}$$

as the fundamental variable. The Thomas-Fermi theory however suffered from serious drawbacks primarily due to the fact that the approximations for the kinetic energy of electrons as well as errors in the exchange energy were unable to sustain bound states. It was not until 1964, when Hohenberg and Kohn put forth two crucial theorems[86] which provided a practical approach for reducing the many-electron problem to an effective one-electron problem. Density functional theory is thus based on the two fundamental mathematical theorems proved by Hohenberg and Kohn.

2.2.1 The Hohenberg-Kohn Theorems

The two Hohenberg-Kohn theorems state that :-

Theorem 1: There is a one-to-one correspondence between the ground-state electron charge density $\rho_o(\mathbf{r})$ of a many electron system and the external potential $V(\mathbf{r})$.

Proof of theorem 1: Let us consider two N-electron systems, characterised by two different external potentials (differing by more than an additive constant), $v_1(\mathbf{r})$ and $v_2(\mathbf{r})$. Let us further assume, that the corresponding two wave-functions ψ_1 and ψ_2 yield the same ground state electron charge density $\rho_0(\mathbf{r})$. Therefore, the eigenvalue equation for the Hamiltonian H is

$$\begin{aligned} \hat{H}_1\hat{\psi}_1 &= E_1\hat{\psi}_1 \\ \hat{H}_2\hat{\psi}_2 &= E_2\hat{\psi}_2 \end{aligned} \tag{2.8}$$

Using the variational principle, one may obtain the energy expression as

$$E_1 = \langle\hat{\psi}_1|H_1|\hat{\psi}_1\rangle < \langle\hat{\psi}_2|H_2|\hat{\psi}_2\rangle \tag{2.9}$$

$$= \langle\hat{\psi}_2|H_2|\hat{\psi}_2\rangle + \langle\hat{\psi}_1|H_1 - H_2|\hat{\psi}_1\rangle \tag{2.10}$$

$$< E_2 + \int dr\rho(\mathbf{r})[v_1(\mathbf{r}) - v_2(\mathbf{r})] \tag{2.11}$$

On interchange of suffixes one can obtain

$$E_2 < E_1 + \int dr\rho(\mathbf{r})[v_2(\mathbf{r}) - v_1(\mathbf{r})] \tag{2.12}$$

By summing the two inequalities Eqn (2.10) and Eqn (2.11) we face a contradiction

$$E_1 + E_2 < E_2 + E_1 \tag{2.13}$$

Thus the assumption of identical density arising from two different external potentials is wrong. This automatically follows the following: A given ground state charge density $\rho_0(\mathbf{r})$ uniquely determines the external potential and thus the Hamiltonian of the many-electron system. Furthermore, the ground state expectation value of any observable $\hat{A}$ is a unique functional of the ground state electron charge density.

Theorem 2: The second theorem defines an important property of the energy functional. The exact ground state energy (E_o) is given by the global minimum of $E[\rho(\mathbf{r})]$, and the ground state density is the density that minimizes $E[\rho(\mathbf{r})]$. That is, the charge density that minimizes the total energy is the ground state charge density $\rho_0(\mathbf{r})$.

Proof of theorem 2: We consider the many-body Hamiltonian $\hat{H} = \hat{T} + \hat{V} + \hat{V_{ext}}$ where $\hat{T}$ is the kinetic energy, $\hat{V}$ is the electron-electron interaction and $\hat{V_{ext}}$ is the external potential. The ground state wavefunction can be denoted by ψ. For a given electron charge density $\rho(\mathbf{r})$, the ground-state total energy functional takes the form

$$\begin{aligned} E[\rho] &= \langle \psi[\rho] | \hat{H} | \psi[\rho] \rangle \\ &= \langle \psi[\rho] | \hat{T} + \hat{V} | \psi[\rho] \rangle + \langle \psi[\rho] | \hat{V_{ext}} | \psi[\rho] \rangle \\ &= F[\rho] + \int \rho(\mathbf{r}) \hat{V_{ext}}(\mathbf{r}) d\mathbf{r} \end{aligned}$$

where the Hohenberg-Kohn density functional $F[\rho]$ is universal for any many-electron system. $E[\rho]$ reaches its minimal value (equal to the ground-state total energy) for the ground state density corresponding to V_{ext}.

The Hohenberg-Kohn variational theorem states that the ground state energy can be obtained variationally. The exact ground state energy $E_0[\rho_0(\mathbf{r})]$ is the global minimum value of the functional $E[\rho](\mathbf{r})]$. The electron density that minimizes the energy of the overall functional is the true ground state electron density. So, if $\rho_0(\mathbf{r})$ is the ground state electron density, then this implies that, for any density $\rho(\mathbf{r})$, other than ground state density,

$$E[\rho(\mathbf{r})] \geq E_0[\rho_0(\mathbf{r})] \tag{2.14}$$

The difficulty in the above formulation is that the exact analytical form of universal functional $F[\rho](\mathbf{r})]$ is not known which consists of all many body effects. The equations of Kohn and Sham, published in 1965 [87], led to the formulation of modern DFT.

2.2.2 Kohn-Sham Formulation

The approach proposed by Kohn and Sham for electronic structure calculation is to replace the original many-body problem by an auxiliary independent particle problem. The density of the original system is assumed to be equal to that of non-interacting system, and the interactions are incorporated into an exchange-correlation functional of the density.

For system of N interacting electrons in the external potential V_{ext}, the total energy functional can be written as, $E[\rho] = F[\rho] + \int \hat{V}_{ext}(\mathbf{r})\rho(\mathbf{r})d\mathbf{r}$ with the $F[\rho]$ for the system given by

$$F[\rho] = T[\rho] + E_{ee}[\rho] \tag{2.15}$$

where $T[\rho]$ is the kinetic energy of the interacting electron, $V_{ee}[\rho]$ is the electron-electron interaction energy of electrons. $F[\rho]$ in the above equation is called the Hohenberg-Kohn functional. The expression for the ground state energy functional can be written as

$$V_{KS} = V_{ext}(\mathbf{r}) + V_H(\mathbf{r}) + V_{XC}(\mathbf{r}) \tag{2.16}$$

where E_H is the Hartree term or the self-interaction energy of density $\rho(\mathbf{r})$, E_{XC} is the exchange-correlation energy functional. The density of the system is expressed as

$$\rho(\mathbf{r}) = \sum_i^N |\phi_i|^2 \tag{2.17}$$

The exchange-correlation potential is given by the functional derivative

$$V_{XC} = \frac{\delta E_{XC}(\rho)}{\delta(\rho)} \tag{2.18}$$

The minimization of E_H is carried out subject to the constraint of normalized density $\int \rho(\mathbf{r})d\mathbf{r} = N$. The total energy functional for this non-interacting electron system can be written as

$$E_{KS}[\rho] = T_s[\rho(\mathbf{r})] + \int V_{ext}(\mathbf{r})\rho(\mathbf{r})d\mathbf{r} + \frac{1}{2}\frac{e^2}{4\pi\epsilon_0}\int\int \frac{\rho(\mathbf{r})\rho(\mathbf{r}')}{|\mathbf{r} - r'|}d\mathbf{r}d\mathbf{r}' + E_{xc}[\rho(\mathbf{r})] \tag{2.19}$$

and the corresponding Hamiltonian is given by

$$H_{KS} = -\frac{\hbar^2}{2m}\nabla^2 + V_{KS}(\mathbf{r}) \tag{2.20}$$

Thus using Eqn (2.15), (2.18) and (2.19) one can find the one-electron orbitals ϕ_i, which minimize the energy and satisfy the following set of one-electron Schrödinger-like equations

$$[-\frac{\hbar^2}{2m}\nabla^2 + V_{KS}(\mathbf{r};\rho)]\phi_i(\mathbf{r}) = \epsilon_i\phi_i(\mathbf{r}) \tag{2.21}$$

where ϕ_i and ϵ_i are the single-particle wave-functions and eigenvalues, respectively. The Eq.(2.20), therefore, represents the set of Kohn-Sham self-consistent equations. Since $V_H(\mathbf{r})$ and $V_{XC}(\mathbf{r})$ depend on ρ, which depend on ϕ_i, which in turn depend on $V_{KS}(\mathbf{r})$, the problem of solving the Khon-Sham equations is not a straight-forward one. The usual way of solving such problems is the iterative procedure, i.e. to start with an initial guess for $\rho(\mathbf{r})$, calculate the corresponding $V_{KS}(\mathbf{r})$, and then solve the differential equation (Eq.(2.20) for the ϕ_i. From these one calculates a new density, and starts again. The process is repeated until the energy converges. Thus the procedure is called a self-consistent field method, which is summarized in a flowchart given Fig. 2.1.

2.2.3 Exchange-Correlation Functional

The method proposed by Kohn-Sham, described above is exact, assuming that exact form of exchange-correlation functional is known. In reality, as the exact expression for exchange-correlation energy E_{xc} is not known, the Kohn-Sham potential V_{KS} itself becomes an unknown quantity. Hence, accurate approximations to the exchange-correlation functional are needed in order to obtain ground state

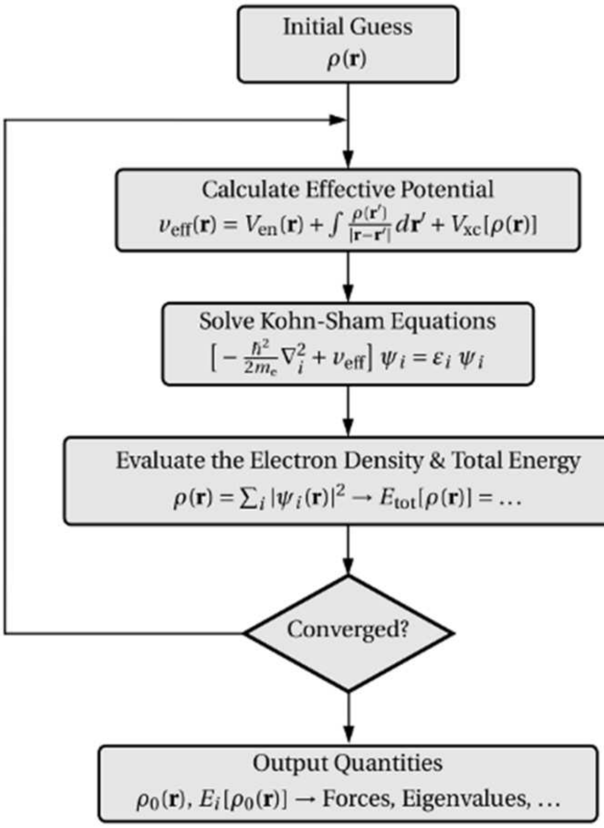

Figure 2.1: The iterative steps to solve the Kohn-sham equations. This figure is taken from Ref [17].

energy and density. The two most widely used approximations used for various calculations in this thesis are discussed here: the local density approximation (LDA) and generalized gradient approximation (GGA).

The simplest of these descriptions is called the Local Density Approximation (LDA), where the exchange correlation energy of a real system is expressed by the electronic charge density corresponding to that of a homogeneous electron gas. The exchange correlation energy takes the form

$$E_{xc}^{LDA}[\rho(\mathbf{r})] = \int \rho(\mathbf{r})\epsilon_{xc}[\rho(\mathbf{r})]d\mathbf{r} \tag{2.22}$$

where $\epsilon_{xc}[\rho(\mathbf{r})]$ is the exchange-correlation energy per electron in a homogeneous gas with electron density $\rho(\mathbf{r})$. Within the LDA, $\epsilon_{xc}[\rho(\mathbf{r})]$ is a function of only the local value of the density. It can be separated into exchange and correlation contributions;

$$\epsilon_{xc}(\rho) = \epsilon_x(\rho) + \epsilon_c(\rho) \tag{2.23}$$

Since the exchange energy of the homogeneous electron gas is known exactly [88], $\epsilon_x(\rho)$ takes the following form,

$$\epsilon_x(\rho) = -\frac{3e^2}{4}(\frac{3}{\pi})^{1/3}\rho(\mathbf{r})^{1/3} \tag{2.24}$$

The functional form for the correlation energy density, $\epsilon_c(\rho)$, is unknown and has been simulated for the homogeneous electron gas in numerical quantum Monte Carlo calculations which yield essentially exact results [89]. The resultant exchange correlation energy has been fitted by a number of analytic forms [90, 91] all of which yield similar results in practice and are collectively referred to as LDA functionals.

To make these functionals more accurate, the idea of exchange-correlation energy in terms of density $\rho(\mathbf{r})$ can be extended to include the information on how the density varies spatially in the functional. The exchange correlation functional which incorporate this modification is known as Generalized Gradient Approximations (GGA)[92] which can be expressed as

$$E_{xc}^{GGA}[\rho] = \int f(\rho(\mathbf{r}), \nabla\rho(\mathbf{r}))d\mathbf{r} \tag{2.25}$$

The choice of the function $f(\rho(\mathbf{r}), \nabla\rho(\mathbf{r}))$ differs for different GGAs. The calculations presented in this thesis are mostly done using the functional proposed by Perdew, Burke and Ernzerhof in 1996, famously known as PBE [93].

To solve the single-particle Kohn-Sham equations and to obtain the eigenvalues and eigenfunctions one need to choose an appropriate basis set to expand the single-particle wave-functions. We can group basis function in several types, in which Kohn-Sham orbitals can be expanded to obtain the eigenvalues and eigenfunctions. In this thesis we have used two types of basis set methods for geometry optimization and electronic structure calculations, plane wave basis set within the projected augmented wave (PAW) scheme and the linearized augmented plane wave method (LAPW) as discussed below.

2.2.4 Bloch electrons and plane wave method

For solids, the wave function of an electron placed in a periodic potential i.e., the effective potential derived in K-S equation has a periodicity of the cystalline lattice. From Bloch's theorem we can write K-S orbitals, $\psi_k^n(r)$ as a product of a plane wave $e^{i\mathbf{k.r}}$ and periodic function, $u_k^n(r)$ that has periodicity of the lattice.

$$\psi_k^n(r) = u_k^n(r)e^{i\mathbf{k.r}} \tag{2.26}$$

where k is vector in first Brillouin zone and n is a band index. Due to its periodicity $u_k^n(r)$ can be expanded as a set of plane waves

$$\psi_k^n(r) = \frac{1}{\sqrt{\Omega_{cell}}} \sum_j c_j^n(k)e^{i(\mathbf{k}+\mathbf{k_j}).\mathbf{r}} \tag{2.27}$$

where k_j is the reciprocal lattice vector, Ω_{cell} is the volume of the primitive cell. Expanding the K-S orbitals to plane wave basis set, we obtain

$$\sum_{j'} H_{j,j'}(k)c_{j'}^n(k) = \epsilon_n(k)c_j^n(k) \tag{2.28}$$

where

$$H_{j,j'}(k) = \frac{\hbar^2}{2m}|k + K_j|\delta_{j,j'} + V_{eff}(K_j - K_{j'}) \tag{2.29}$$

The above term is the matrix element of kinetic energy operator where the plane waves are orthonormalized once and

$$V_{eff}(K_j - K_{j'}) = \int_{\Omega_{cell}} V_{eff}(r)e^{i(\mathbf{k_j}-\mathbf{k_{j'}}).\mathbf{r}} \tag{2.30}$$

Where K is the reciprocal lattice vector. The above term is effective potential. Diagonalization of this Hamiltonian gives rise to discrete set of eigenvalues and corresponding eigenfunctions for all n band index at each k-point. The energy eigenvalue looks like,

$$\epsilon_n(k) = \epsilon_n(k + K) \tag{2.31}$$

We can choose cut-off vector in reciprocal space, $\mathbf{K}$ as $K \leq K_{max}$, where K_{max} is the reciprocal space wave vector corresponding to a chosen energy cut-off.

2.2.5 Linearized Augmented Plane Wave (LAPW) method

The linearized version of Augmented Plane Wave (LAPW) basis [94], following the Andersons linearization approach is, expressed as,

$$\chi_q(\mathbf{r},\epsilon) = \begin{cases} \sum_{l,m}(A^q_{lm,R}\phi_{LR}(r_R,\epsilon_\nu) + B^q_{lm,R}\phi_{LR}(\dot{r}_R,\epsilon_\nu)) & for\ r_R \leqslant S_R \\ e^{i\mathbf{k}.\mathbf{r}} & for\ r_R > S_R \end{cases}$$

where the coefficients $A^q_{lm,R}$ and $B^q_{lm,R}$ can be determined by matching these solutions in magnitude and slope at the sphere boundary. To do so the plane wave solution in the interstitial is required to expand in terms of Bessel functions $j_l(r_R, q)$. In principle a large number of l values are required for exact matching, but to keep the problem tractable one truncates this number at some value l_{max}. Therefore in band structure calculations based on LAPW basis set a crucial parameter is l_{max} for which a reasonable choice is needed. The condition that allows a good choice of l_{max} is,

$$R_i K_{max} = l_{max} \tag{2.32}$$

where R_i is the radius of i^{th} MT sphere and K_{max} determines the cut-off for the plane waves. The accuracy of the basis is controlled by the quantity $R_i^{min}K_{max}$, where R_i min is the smallest MT sphere radius in the unit cell. In this method the core states which do not participate in chemical bonding, are treated as in free atoms, but subject to the potential due to the valence states.

2.2.6 Projector Augmented Wave (PAW) method

It is important to know features of wave functions because at the nuclei region the waves functions oscillate rapidly and at delocalized region they are smooth in nature. Calculations of these wave functions are necessary. To get augmented wave methods the wave functions are divided into two parts, first part of partial waves are expanded within an atom-centered region and second part is expanded near envelope region called as envelope functions. In this section one of augmented wave function know as PAW is going to be explained here.

PAW is a general method for all-electron solution has been developed by Blochl [95].The PAW has been made up by combining the features of plane-wave pseudo potential method and linear augmented plave wave (LAPW) method. In PAW method, the pseudo-wave-functions $|\tilde{\psi_n}\rangle$ are linearly transformed to get one electron wave functions $|\psi_n\rangle$

$$|\psi_n\rangle = |\tilde{\psi_n}\rangle + \sum (|\phi_i\rangle - |\tilde{\phi_i}\rangle) \langle \tilde{\mathbf{P}}_{\mathbf{i}}| \, |\tilde{\psi_n}\rangle \tag{2.33}$$

The relation is made up on definition of augmentation volume, Ω_R, where R is the atomic site, in which the partial waves $|\phi_i\rangle$ form a basis of atomic wave functions, where $\tilde{\mathbf{P}}_{\mathbf{i}}$ is are set of projectors on partial waves $|\tilde{\phi_i}\rangle$.

2.3 Molecular Dynamics

Atomistic simulation allows us to study material's behaviour at the atomistic scale by investigating how atoms interact with one another inside the structure. Different phenomena, such as material defects and deformations, require the atomic scale accuracy and understanding of interactions between atoms. The first step of an atomistic simulation involves creating a material structure by means of a set of atomic coordinates, which in case of metals involves creating a crystal lattice and placing atoms on lattice points. Next, the simulation requires an energy functional or potential, that governs how atoms interact. The potential presents the biggest challenge and can be based on classical dynamics or quantum mechanics. Quantum approach is more accurate because, the electronic structure of each atom is analyzed, but must be applied on the smaller number of atoms due to high computational cost and limited computational capabilities available. The classical molecular dynamics (MD) approach is based on the simplified mathematical expressions that replaces the electronic degrees of freedom by an effective potential and forces between the nuclei. Without complex electronic structure of each atom classical MD is able to handle models with higher number of atoms, but with less accuracy.

2.3.1 Empirical Atomistic Models

Metallic bonding is characterized by electrostatic forces between an electron cloud of ‘free’ electrons and the positively charged metal ions. Electrons in the cloud are shared among lattice bound positive ions. So, an effective potential should as accurately as possible describe the potential energy of positively charged ions while approximating the electron contribution to the energy as a function of ion positions. Here we deal with solid metallic systems and the main challenge is for the potential to describe the environment of an atom embedded in the background of valence electrons of the host solid. This valence electron density is effectively described by the Embedded Atom Method (EAM). Empirical potentials, such as EAM, use a purely classical description of interactions between atoms which means the introduction of approximations that limit the transferability of the model. An effective empirical potential must satisfy the following critical properties:

1. Flexibility: In order to be flexible, a potential has to feature a sufficient range of fitting parameters to match key properties such as, for solids, lattice constants, cohesive energy, elastic properties, vacancy formation and surface energies.

2. Accuracy: Fitting parameters enable a potential to be fine-tuned to closely reproduce results of more accurate first-principles methods used as the basis for its creation.

3. Transferability: Now the fine-tuned potential should be able to describe structures not included in its fitting data base. On many occasions, this is only possible with qualitative, but not quantitative accuracy.

4. Computing efficiency: The potential has to function within limits of available computational resources, handle the system size and timescales of interest efficiently.

2.3.2 Embedded Atom Method (EAM)

A simplified approach towards the total energy of a solid is to assume that it can be expressed as a sum of all pair interactions between atoms. These interactions would be regarded as independent of one another, so that one bond is not affected by the presence of another bond. In reality, bonds in metals do not follow this simple pair-potential approximation due to many-atom interactions that govern fundamental properties of solids.

Embedded atom method (EAM), a pair potential model, was developed in order to accurately treat metallic systems in terms of their fracture response, surfaces, impurities and alloying additions. The basis for the EAM is quasiatom, as well as the effective medium theory. Quasiatom is a term that treats the whole atom as nucleus or ion, and electron polarization cloud as a single unit. Its energy is a function of the host electron density in which it is immersed. The quasiatom is neutral and unaffected by electric potentials due to charge distributions. Effective medium theory is another approach for calculating the embedding energy of an atom in a host system. The basic idea is to replace the (low-symmetry; imperfect) host by an effective (high-symmetry;ideal) host consisting of a homogeneous electron gas (jellium) of a density equal to that seen by the atom.

Jellium, also known as the uniform electron gas (UEG) or homogeneous electron gas (HEG), is a quantum mechanical model of interacting electrons in a solid. Positive charges (i.e. atomic nuclei) are assumed to be uniformly distributed in the space, therefore the electron density is also uniform in the space. So, without using the crystal structure of a real material we can analyze the effects due to quantum nature of electrons. This model serves as the basis for the EAM form. In the embedded atom method the energy of the metal, E, is derived from the embedding energy F and an electrostatic pair potential ϕ. The embedding energy is the energy to embed an atom into the local electron density created by the remaining atoms in the system. The EAM is one of the most widely used empirical many-body interatomic potential formalism by Daw and Baskes [96]. It has led to encouraging results in a number of atomistic studies for cubic transition and noble metals. But atomistic studies using EAM have been less common for hcp elements than cubic elements. The difficulty primarily arises from the large number of structural parameters which should be fitted to describe the lattice anisotropy. It is believed that the failure of the EAM in describing the physicsl properties of hcp elements comes from the lack of angular dependency in the EAM formalism. Later on, a modified version of the EAM was proposed by Baskes [97] which included the directionality of bonding and was named modified embedded atom method (MEAM).

2.4 Modified Embedded Atom Method (MEAM)

The MEAM can describe a wide range of elements without changing the functional expression. It has been applied to provide atomic potentials of various fcc, bcc, diamond, and gaseous elements [97]. The basic formalism is discussed below.

2.4.1 Formalism

In the MEAM, the total energy of a system is approximated as

$$E = \sum_i \left[F_i(\bar{\rho}_i) + \frac{1}{2} \sum_{j(\neq i)} \phi\left(R_{ij}\right) \right] \tag{2.34}$$

F_i is the embedding function, $\bar{\rho}_i$ is the background electron density at site i, and $\phi_{ij}(R_{ij})$ is the pair interaction between atoms i and j separated by a distance R_{ij}. The functional forms for the two terms on the right hand side of Eq.(2.34), F_i and ϕ_{ij} are given as follows :

$$F\left(\bar{\rho}\right) = AE_c \frac{\bar{\rho}}{\bar{\rho}^0} ln \frac{\bar{\rho}}{\bar{\rho}^0} \tag{2.35}$$

where A is an adjustable parameter, E_c is the cohesive energy, and $\bar{\rho}^0$ is the background electron density for a reference structure. The reference structure is a structure where individual atoms are on exact lattice points. Normally, the equilibrium structure is taken as the reference structure for elements. The background electron density $\bar{\rho}_i$ at a site is computed considering directionality in bonding, that is, by combining several partial electron density terms, $\rho_i^{(0)}$, $\rho_i^{(1)}$,

$\rho_i^{(2)}$, $\rho_i^{(3)}$ for different angular contributions with weight factors $t^{(h)}(h = 1 - 3)$. Each partial electron density term has the following form

$$\left(\rho_i^{(0)}\right)^2 = \left[\sum_{j\neq i} \rho_j^{a(0)}(R_{ij})\right]^2 \tag{2.36}$$

$$\left(\rho_i^{(1)}\right)^2 = \sum_{\alpha} \left[\sum_{j\neq i} \frac{R_{ij}^{\alpha}}{R_{ij}} \rho_j^{a(1)}(R_{ij})\right]^2 \tag{2.37}$$

$$\left(\rho_i^{(2)}\right)^2 = \sum_{\alpha,\beta} \left[\sum_{j\neq i} \frac{R_{ij}^{\alpha} R_{ij}^{\beta}}{R_{ij}^2} \rho_j^{a(2)}(R_{ij})\right]^2 - \frac{1}{3}\left[\sum_{j\neq i} \rho_j^{a(2)}(R_{ij})\right]^2 \tag{2.38}$$

$$\left(\rho_i^{(3)}\right)^2 = \sum_{\alpha,\beta,\gamma} \left[\sum_{j\neq i} \frac{R_{ij}^{\alpha} R_{ij}^{\beta} R_{ij}^{\gamma}}{R_{ij}^3} \rho_j^{a(3)}(R_{ij})\right]^2 - \frac{3}{5}\sum_{\alpha}\left[\sum_{j\neq i} \frac{R_{ij}^{\alpha}}{R_{ij}} \rho_j^{a(3)}(R_{ij})\right]^2 \tag{2.39}$$

Here, $\rho_j^{a(h)}$ represent atomic electron densities from j atom at a distance R_{ij} from site i. R_{ij}^{α} is the α component of the distance vector between atoms j and $i(\alpha = x, y, z)$. The partial electron densities are equivalent to an expansion of density in Legendre polynomials. The way of combining the partial electron densities to give the total background electron density is not unique, and several expressions have been proposed. Among them, the following form has been most widely used and chosen in the present work.

$$\bar{\rho}_i = \rho_i^{(0)} G(\Gamma_i) \tag{2.40}$$

where

$$G(\Gamma) = \frac{2}{1 + e^{-\Gamma}} \tag{2.41}$$

and

$$\Gamma = \sum_{h=1}^{3} t^{(h)} \left[\frac{\rho_i^{(h)}}{\rho_i^{(0)}}\right]^2 \tag{2.42}$$

$t_i^{(h)}$ are adjustable parameters. The atomic electron density is given as

$$\rho_j^{a(h)}(R) \;=\; e^{-\beta(h)\left(\frac{R}{r_e}-1\right)} \tag{2.43}$$

where $\beta^{(h)}$, the decay lengths are adjustable parameters and r_e is the nearest-neighbour distance in the equilibrium reference structure.

As shown above, a specific form is given to the embedding function F_i, but not to the pair interaction ϕ_{ij}. Instead the total energy per atom for the equilibrium reference structure is estimated from the zero-temperature universal equation of state by Rose *et al* [98] as a function of nearest-neighbour distance R.

$$E^u(R) \;=\; -E_c(1 + a^* + da^*)e^{-a^*} \tag{2.44}$$

where d is an adjustable parameter, and

$$a^* \;=\; \alpha\left(\frac{R}{r_e - 1}\right), \tag{2.45}$$

and

$$\alpha \;=\; \left(\frac{9B\Omega}{E_c}\right)^{1/2} \tag{2.46}$$

$E^u(R)$ is the universal function for a uniform expansion or contraction in the reference structure, B is the bulk modulus, and Ω is the equilibrium atomic volume.

Once the total energy per atom and embedding function are computed for a reference structure, the values of the pair interaction can be obtained numerically using Eq. 2.34, as a function of the nearest-neighbour distance.

In the original MEAM, only first nearest-neighbour interactions are considered. The inclusion of the second nearest-neighbour interactions in the 2NN MEAM formalism is affected by adjusting the screening parameters, C_{min} and C_{max}, so that the many-body screening becomes less severe. In the MEAM, the many-body screening function between atoms i and j, S_{ij}, is defined as the product of the screening factors, S_{ikj}, due to all other neighbour atoms k

$$S_{ij} \;=\; \prod_{k\neq i,j} S_{ikj} \tag{2.47}$$

The screening factor S_{ikj} is computed using a simple geometric construction. Imagine an ellipse on a x, y plane, passing through atoms, i, k, and j with the x axis of the ellipse determined by atoms i and j. The equation of the ellipse is given by

$$x^2 + \frac{1}{C}y^2 = \left(\frac{1}{2}R_{ij}\right)^2 \tag{2.48}$$

For each atom k, the value of parameter C can be computed from relative distances among the three atoms, i, j and k, as follows :

$$C = \frac{2(X_{ik} + X_{kj}) - (X_{ik} - X_{kj})^2 - 1}{1 - (X_{ik} - X_{kj})^2} \tag{2.49}$$

where $X_{ik} = (R_{ik}/R_{ij})^2$ and $X_{kj} = (R_{kj}/R_{ij})^2$. The screening factor, S_{ikj} is defined as a function of C as follows :

$$S_{ikj} = f_c \left[\frac{C - C_{min}}{C_{max} - C_{min}}\right] \tag{2.50}$$

where C_{min} and C_{max} are the limiting values of C determining the extent of screening and the smooth cutoff function is

$$f_c\,(x) = 1 \qquad x \geq 1, \tag{2.51}$$

$$\left[1 - (1 - x)^4\right]^2 \qquad 0 < x < 1, \tag{2.52}$$

$$0 \qquad x \leq 0 \tag{2.53}$$

The basic idea for the screening is that: First define two limiting values, C_{max} and $C_{min}(C_{max} > C_{min})$. Then, if the atom k is outside the ellipse defined by C_{max}, it is assumed that the atoms k does not have any effect on the interaction between atoms i and j. If the atom k is inside of the ellipse defined by C_{min} it is assumed that the atom k completely screens the $i - j$ interaction, and between C_{max} and C_{min} the screening changes gradually. In the numerical procedure the electron density and pair potential are multiplied by the screening function S_{ij}. Therefore, $S_{ij} = 1$ and $S_{ij} = 0$ mean that the interaction between atoms i and j is unscreened and completely screened, respectively. In addition to the many-body screening function, a radial cutoff function which is given by $f_c[(r_c - r)/\Delta r]$ where r_c is the cutoff distance and $\Delta r(0.1A^o)$ is the cutoff region, is also applied to the atomic electron density and the pair potential. The radial cutoff distance is chosen in a manner, such that it does not have any effect on the calculation results due to the many-body screening.

The MEAM has also been applied to develop interatomic potentials of hcp elements by Baskes and Johnson [99]. It was further modified by Lee and Baskes to solve structural stability problems with the previous version [100, 101]. The new formalism considers up to second nearest neighbor interactions while the original MEAM only considered first nearest neighbor interactions and this was named the second nearest neighbor (2NN) MEAM which is used in this thesis.

While atomic simulations are limited in size, and especially in simulation time, mesoscopic simulation can be used as a tool to bridge the gap between the atomistic and macroscopic length-scales. In mesoscale simulations the essential physics is incorporated in a simple model that exhibits the main behaviour.

2.5 Peierls-Nabarro model

Accurate modeling of the dislocation-interface interaction needs explicit determination of the dislocation core structure since the critical stage is mainly the cores passing across the interface. Peierls-Nabarro (PN) model specifies a planar core structure that is good for most fcc crystals. The slip plane divides the crystal into two semi-infinite simple cubic crystals. These two parts are modeled as isotropic linear elastic continuum while the two atomic planes immediately above and below the glide plane are connected by inelastic atomic forces due to the misfit of atomic planes. The dislocation modeled as a continuous distribution of infinitesimal dislocations generates stresses at the glide plane, which are calculated according to elasticity theory. The elastic stresses are balanced by atomic forces connecting the two atomic planes on each side of the glide plane. The knowledge of the stress field of a Volterra dislocation in an infinite medium with one or two interfaces is necessary in applying the PN model in heterogeneous media. The Volterra dislocation model, assuming linear elastic response in the core, induces physically unrealistic singularity in the core, therefore a rough estimation of the core cut-off parameter r_0 and core energy E_0 are used to represent the core effect. A model of extended dislocation was first presented, rather tersely, by Peierls

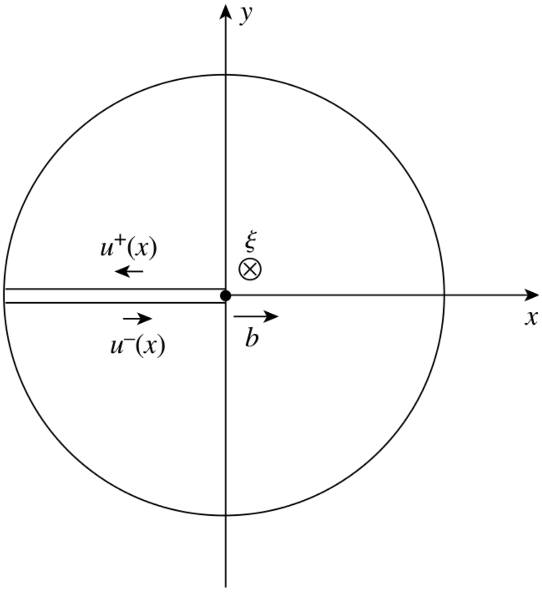

Figure 2.2: The Volterra edge dislocation inserted along the negative z axis at the origin $x = y = 0$. This figure is taken from Ref [18].

(1940) [102], which was extended further by Nabarro (1947) [103]. The details of the PN model described here follows the description given by Bulatov and Cai [18].

Formalism of the PN model

Consider an extended edge dislocation originally considered by Volterra. In Fig. 2.2, a cut is introduced from the left along plane $y = 0$ such that the boundary of the cut is along the z axis (out of plane). Assigning the displacement fields on the upper and lower surfaces of the cut to be $u^+(x)$ and $u^-(x)$ respectively, the Volterra dislocation is created by displacing the lower surface with respect to the upper surface by $b\ \mathbf{e}_x$ and then reconnecting the two surfaces together. Choosing the line direction ξ to be along the negative z axis (into the plane), the Burgers vector of this dislocation is $\mathbf{b}$=$b\ \mathbf{e}_x$.

Let us define $u(x) \equiv u^+(x) - u^-(x)$ as the *disregistry* or *misfit* across the cut plane. Then, in the Volterra dislocation, $u(x)$ is a step function,

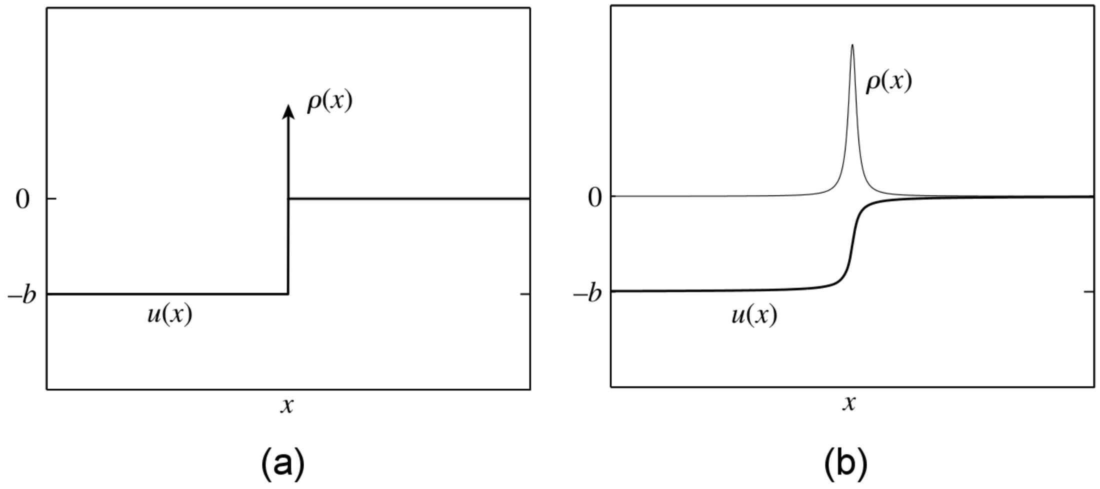

Figure 2.3: (a) In the Volterra dislocation, the distribution of disregistry $u(x)$ across the cut plane is a step function, while the density of this distribution $\rho(x) = du(x)/dx$ is a delta function. (b) In the PN dislocation, both $u(x)$ and $\rho(x)$ are smooth functions. This figure is taken from Ref [18].

$$u(x) = \begin{cases} -b, & x < 0 \\ 0, & x > 0 \end{cases}$$

Equivalently, the distribution of disregistry across the plane of the cut is described by the disregistry density $\rho(x) \equiv du(x)/dx$, which, for the Volterra dislocation, is a delta function, $\rho(x) = b\,\delta(x)$, Fig. 2.3(a). This simple discontinuous distribution is a useful idealization leading to simple analytic solutions for the elastic fields produced by the Volterra dislocation. However, the same solutions for the stress and strain fields are singular along the dislocation line ($x = y = 0$) itself. This behavior is unphysical and the PN model removes the singularity by allowing the Burgers vector distribution to spread out, as shown in Fig. 2.3(b). Furthermore, the actual shape of the distribution function $\rho(x)$ is selected in the PN model to take into account the non-linear interactions in the dislocation core.

As proposed by E. Orowan, the non-linear core is treated separately while keeping the linear elasticity intact everywhere else. Accordingly, the total energy of a dislocation is written as the sum of two contributions, $E_{tot} = E_{el} + E_{msft}$, in which E_{el} is the elastic energy and E_{msft} is an extra energy term associated with the non-linear misfit in the core. The actual shape of the distribution function $\rho(x)$ is such that it minimizes the total energy E_{tot}. As we shall see below, the elastic energy decreases, while the misfit energy increases with the increasing width of the misfit distribution $\rho(x)$. The shape of this distribution is determined by the best compromise between these two opposing energy terms. The elastic energy is given by,

$$E_{el} = \frac{1}{2}\int_{-\infty}^{\infty} \sigma_{xy}(x)u(x)dx \tag{2.54}$$

The solution for the stress produced by the singular Volterra dislocation shown in Fig. 2.2 is very simple,

$$\sigma_{xy}^{0}(x) = \frac{\mu b}{2\pi(1-\nu)}\frac{1}{x} \tag{2.55}$$

For the PN dislocation whose disregistry density is $\rho(x)$, the stress $\sigma_{xy}(x)$ is simply the convolution of $\sigma_{xy}^{0}(x)$ with $\rho(x)$,

$$\sigma_{xy}(x) = \frac{\mu}{2\pi(1-\nu)}\int_{-\infty}^{\infty} \frac{\rho(x')}{x-x'}dx' \tag{2.56}$$

Substituting this expression into Eq. 2.54 and integrating by parts, the elastic energy becomes

$$\begin{aligned} E_{el} &= \frac{\mu}{4\pi(1-\nu)}\int_{-\infty}^{\infty}\int_{-\infty}^{\infty} \frac{\rho(x')u(x)}{x-x'}dxdx' && (2.57) \\ &= -\frac{\mu}{4\pi(1-\nu)}\int_{-\infty}^{\infty}\int_{-\infty}^{\infty} \rho(x)\rho(x')ln|x-x'|dxdx' + C && (2.58) \end{aligned}$$

where C is a constant whose magnitude is independent of the shape of the disregistry distribution as long as the values of $u(x)$ at two integration limits $x = \pm\infty$ are fixed. More generally

$$E_{el}[u(x)] = -K\int_{-\infty}^{\infty}\int_{-\infty}^{\infty} \rho(x)\rho(x')ln|x-x'|dxdx' + C \tag{2.59}$$

where $K = \mu/(4\pi)$ for a screw dislocation and $K = \mu/(4\pi(1\nu))$ for an edge dislocation.

As mentioned earlier, due to the displacement of the lower surface with respect to the upper surface there exists a local misfit energy E_{msft}. In case of real crystals, the glide is not uniform across the cut plane. It depends on the two dimensional vector $\mathbf{u}_0$. To describe the energy cost incurred as a result of the shift, it is convenient to use the energy γ per unit area of the cut as a function of the shift vector $\mathbf{u}_0$. Function $\gamma(\mathbf{u}_0)$ is commonly referred to as the *generalized stacking fault* (GSF) energy or simply the γ-surface. In the context of the PN model, $\gamma(\mathbf{u}_0)$ is sometimes called the *misfit potential.* Because of the periodic nature of the crystal lattice, $\gamma(\mathbf{u}_0)$ is a periodic function of two components of the shift vector $\mathbf{u}_0$. Let us assume that $\mathbf{u}_0$ is along the x axis. Then the period of $\gamma(\mathbf{u}_0)$ along the x direction is equal to the Burgers vector b of the dislocation. The simplest form of $\gamma(\mathbf{u}_0)$ is a sinusoid,

$$\gamma(\mathbf{u}_0) = \frac{U}{2}[1 - cos(2\pi u_0/b)] \tag{2.60}$$

Even though in the PN model the misfit $u(x)$ varies along the cut plane, the misfit energy is expressed as

$$E_{msft}[u(x)] = \int_{-\infty}^{\infty} \gamma(u(x))dx \tag{2.61}$$

This integral form assumes that the misfit energy density at point x is a function of the local misfit at the same point. This locality assumption is an approximation that is expected to be valid if $u(x)$ varies slowly as a function of x. Combining Eqs. 2.59 and 2.61, we arrive at an expression for the total energy of the PN dislocation,

$$\begin{aligned} E_{tot}[u(x)] = -K &\int_{-\infty}^{\infty}\int_{-\infty}^{\infty} \rho(x)\rho(x')ln|x - x'|dxdx' \\ &+ \int_{-\infty}^{\infty} \gamma(u(x))dx + C \end{aligned} \tag{2.62}$$

The solution of the PN model is a misfit distribution function $u(x)$ that minimizes the total energy functional Eq. 2.62. In general, there are two approaches to finding a solution. The first is to take the variational derivative of the energy functional to obtain an equation that the optimal solution must satisfy and then solve this equation. The second approach is to obtain a solution by direct minimization of Eq. 2.62. The variational approach is discussed below.

We assume that $u(x)$ is the yet unknown solution, subject to the boundary counditions of $u(-\infty) = -b$, $u(\infty) = 0$. Let us add to it a small variation $\delta u(x)$ such that $\delta u(-\infty) = \delta u(\infty) = 0$. The corresponding variation in E_{tot} must be zero, leading to the following integro-differential equation,

$$0 = \frac{\delta E_{tot}}{\delta u(x)} = 2K \int_{-\infty}^{\infty} \frac{\rho(x')dx'}{x - x'} + \frac{d\gamma(u(x))}{du(x)} \tag{2.63}$$

This equation has the following physical interpretation. At each position x, the first term on the right-hand side of eq. 2.63 represents the Peach-Koehler force due to the local elastic stress which, in equilibrium, must balance the force produced by the gradient of the misfit potential (the second term). When the misfit potential γ takes the form of eq. 2.60, this equation becomes

$$-2K \int_{-\infty}^{\infty} \frac{\rho(x')dx'}{x - x'} = \frac{U\pi}{b} sin\left(\frac{2\pi u(x)}{b}\right) \tag{2.64}$$

Peierls found the following simple analytical solution of this equation:

$$u(x) = \frac{b}{\pi} arctan\left(\frac{x}{\xi}\right) - \frac{b}{2} \tag{2.65}$$

$$\rho(x) = \frac{b}{\pi} \frac{\xi}{x^2 + \xi^2} \tag{2.66}$$

where $\xi = Kb^2/(U\pi)$ can be interpreted as the width of the dislocation core. The stress field of this dislocation along the x axis is

$$\sigma_{xy}(x) = \frac{\mu b}{2\pi(1-\nu)} \frac{\xi}{x^2 + \xi^2} \tag{2.67}$$

which is no longer singular. Notice that ξ is proportional to K but inversely proportional to U. Thus, a stronger elastic interaction (large K) produces a wider dislocation core, whereas a stronger misfit interaction (large U) leads to a narrower core.

Chapter 3

Effect of hydrogen on degradation mechanism of zirconium: A molecular dynamics study

3.1 Introduction

Zirconium is technologically important primarily due to its use as nuclear reactor material. Zirconium alloys are widely used in the nuclear industry for fuel cladding and structural components because of their low capture cross-section, good mechanical and corrosion properties. These alloys are capable of operating in extremely harsh environments, involving high temperature and presence of corrosive coolant such as water.

The application of Zr and Zr alloys however gets limited by the so called hydrogen induced degradation problem. The oxidation of zirconium alloys by decomposition of water leads to release of hydrogen. Subsequently hydrogen diffuses

---

This chapter is based on "Effect of hydrogen on degradation mechanism of zirconium: A molecular dynamics study" - *Poulami Chakraborty*, Amitava Moitra, and Tanusri Saha-Dasgupta, J. Nucl. Mater. **466**, 172 (2015) in the material and forms hydrides, when its terminal solid solubility is exceeded. At lower concentration, the absorbed hydrogen (H) occupies interstitial site in the Zr matrix to form Zr-H solid solution. In both the dilute and concentrated regimes, inclusion of H deteriorates the mechanical properties of Zr, causing embrittlement. Hydrogen embrittlement in Zr alloys is one of the main causes of mechanical degradation of light water reactor fuel cladding and is regarded as one of the most important issues in safety regulation for light water reactor type nuclear power plants [104]. The embrittlement of metallic alloys by hydrogen primarily involve three mechanisms [105] as discussed below: (a) phase transformations, such as hydride precipitation induced by combined presence of H and stress, (b) H-enhanced local plasticity, and (c) weakening of grain boundaries by H. Hydrogen embrittlement may occur by repeated hydride precipitation and cleavage in front of a growing crack. The phenomena involves hydrogen transport and phase transformation (nucleation and growth) near a crack tip which gets affected by the combined effects of stress concentration, temperature distribution and accommodation modes between hydride and matrix. The Zr-H equilibrium phase diagram [106] is shown schematically in Fig. 3.1 [107, 108], which includes an interstitial solid solution phase and a large variety of hydride ZrH_x phases. In our study, we have focussed only on two phases, one in dilute limit of H incorporation, namely α-Zr which is the solid solution HCP phase of Zr metal formed with H, and another in concentrated limit of H incorporation, namely ϵ-Zr which is the ZrH_2 phase.

In the dilute limit of H, several different microscopic mechanisms underlying the H induced degradation have been proposed in literature. For example, several studies have reported H-induced lowering of the critical cleavage stress that affects opening up or propagation of cracks [109, 110, 111]. Adsorption of H on surfaces may reduce the surface excess free energy [112]. Literature supports hydrogen enhanced localized plasticity (HELP) mechanism [113, 114, 115] to be responsible for degradation in metals. A few *ab-initio* studies have evaluated the planar defect properties for a Zr-H solid solution, based on density functional theory (DFT) calculations [112, 114, 116]. These studies indicate that hydrogen in a Zr-H solid solution can enhance dislocation mobility while it lowers surface energy. However, these speculations are yet to be confirmed either through advanced experimental

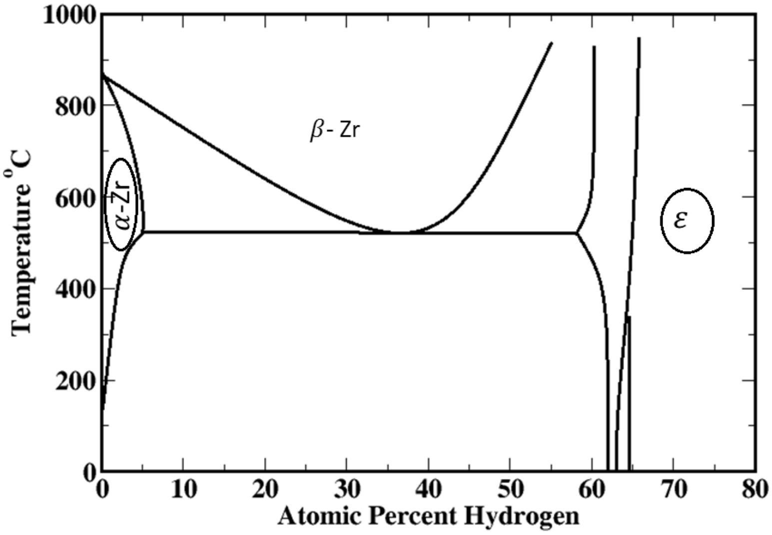

Figure 3.1: A schematic phase diagram of the Zr-H system. The encircled regions are the two phases considered in the present study.

techniques or large scale atomistic simulation, where one can identify specifically the effect of H in Zr deformation behaviour. As hydrogen solubility limit is fairly low even at the operating temperature of light water reactor plants, large scale atomistic modeling of Zr-H systems with different atomic percentage of H may determine the details of the influence of hydrogen on macroscopic mechanical behaviour.

In the concentrated limit of H, the hydrides are brittle and produce cracks on application of stress, that reduces the performance and life expectancy of nuclear reactor, thereby increasing the cost of nuclear power plants. Various studies focusing on the deformation [117, 118, 119, 120] or fracture [121, 122, 123] behavior of zirconium hydrides suggest that hydride precipitates play an important role in the hydrogen embrittlement of various zirconium alloys. Farrow *et al.* have claimed that voids or micro-cracks, generated as a result of interaction between hydride precipitates and twinning structures around the precipitates contribute to embrittlement [124]. Other works suggest that voids nucleate at interfaces between the hydride and zirconium matrix to develop micro-cracks [125].

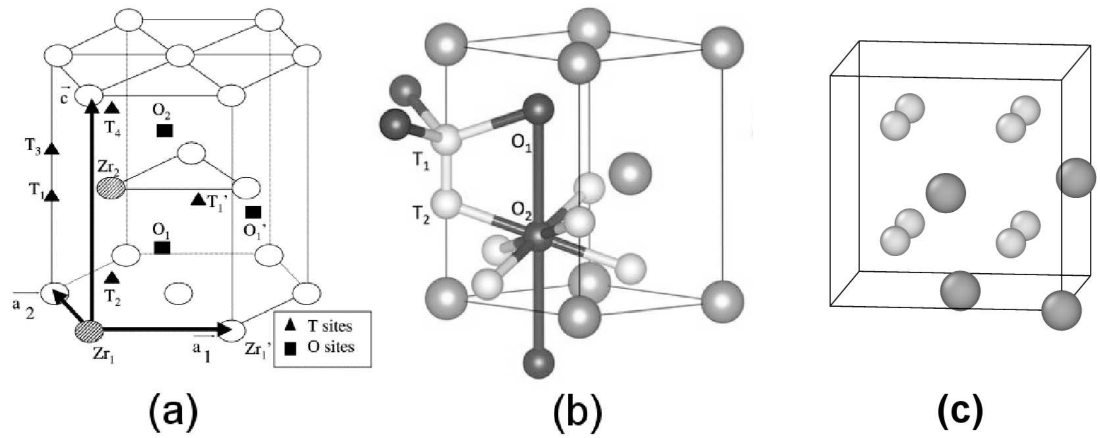

Figure 3.2: (a) Interstitial sites in α-Zr (shaded circles are used for reduced two-atom unit cell). The indexes and primes respectively refer to sites of same (T or O) type in a unit cell, and to similar sites in neighbouring unit cells. Figure adapted from Ref [19]. (b) The orthorhombic α-Zr (bigger balls) unit cell with tetrahedral (light shaded) and octahedral (dark shaded) interstitial sites for hydrogen. Figure adapted from Ref [20]. (c) The tetragonal ϵ-ZrH_2 unit cell with Zr (bigger balls) occupying the face centres and H (smaller balls) occupying the tetragonal sites.

However, in comparison to experimental studies, only few atomic-scale simulation studies of the Zr-H system have been achieved. The atomistic approach involving empirical interatomic potential is ideally suited for such long range defect problems, which aims in capturing details of deformation and fracture processes at atomic level.

3.2 Computational Details

All the molecular dynamics simulation in this study are performed using the Large-scale Atomic/Molecular Massively Parallel Simulator (LAMMPS), developed at the Sandia National Laboratory [126]. This fully parallelized program uses spatial decomposition technique to partition the simulation domain that significantly decreases the simulation time. All simulations are carried out using Zr-H modified embedded atom method (MEAM) semi-empirical potential. Over the last two decades the MEAM methodology has been successfully applied to metals and alloys for studying deformation mechanisms [127, 128]. The original methodology, where only up to the first nearest neighbor interactions are considered, is improved recently by Lee *et al.* to extend the interactions up to second nearest neighbors [129]. A few of these second nearest neighbor (2NN) MEAM potentials has been recently used in large scale atomistic simulations to study the microscopic mechanism for void growth [130], nature of dislocation core structure in Ti [131], ductile to brittle transition [132], etc. The 2NN MEAM potential used in present work was originally used for comparative study on hydrogen diffusion in amorphous and crystalline metals [133].

In order to test the reliability of the chosen potential, we first consider the case of pure Zr in bulk. The atomic positions were first generated in accordance with the crystal symmetry, followed by a structural optimization. The energy per atom as a function of atomic volume was then fitted in order to obtain the relaxed lattice parameters and cohesive energy of pure Zr. Our obtained lattice parameters (a=3.23 Å, c/a=1.59) and cohesive energy (6.36 eV/atom) agree well with other theoretical [116] and experimental [134] observations, reflecting the reliability of the chosen 2NN MEAM potential. Similarly, we found that the calculated lattice parameter, a=4.2 Åfor ϵ-ZrH$_2$ phase matches closely with experimental results [133, 135]. Various structural and elastic properties, other than lattice constant and cohesive energy, such as dilute heat of solution of hydrogen, vacancy formation energy, planar defect properties including stacking fault energies in α-Zr, heat of formation of ϵ-ZrH$_2$ and elastic constants $C_{11}, C_{12}, C_{44}, C_{66}$ of α-Zr phase have been calculated by Kim *et al* [134] and Lee *et al* [133] to check the reliability of this potential. In Ref.[134] the authors also tested the reliability of this potential for thermal properties, such as thermal expansion coefficients, specific heat, melting point, enthalpy of melting.

The large scale simulations are performed on rectangular simulation cells having x, y, and z axes oriented along the $[10\bar{1}0]$, $[1\bar{2}10]$, and [0001] directions, respectively with dimensions 20.67 × 20.70 × 41.22 nm^3. The total number of atoms considered are ∼750,000 for both the dilute and concentrated cases. To study the dilute limit, simulations were carried out with different percentages of H, where hydrogens were placed randomly in interstitial sites. In general, there

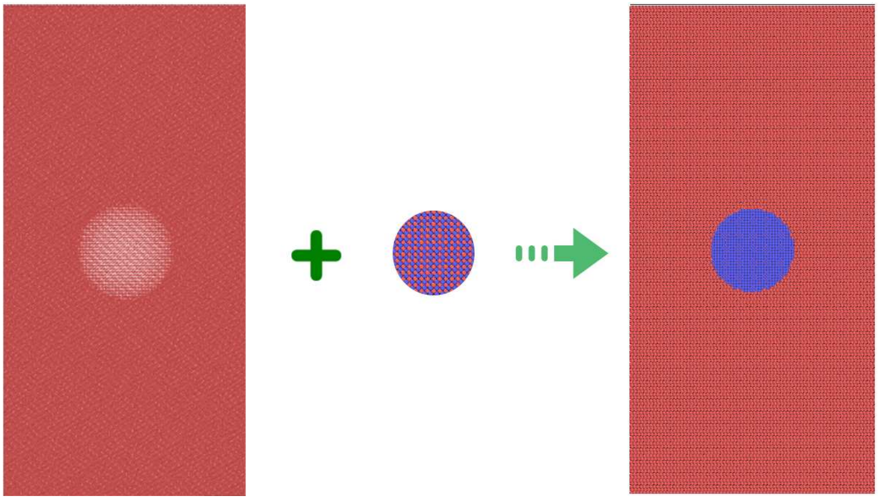

Figure 3.3: Snapshot of the simulation cell for bulk Zr where a sphere of diameter 10nm is cut out as can be identified from the white region at the centre (left panel). The middle panel shows a sphere of ZrH_2 of equal volume. The simulation cell used for the concentrated limit (right panel) where the ZrH_2 sphere is placed inside the bulk Zr simulation cell.

are two interstitial locations in HCP Zr; octahedral (O sites), and tetrahedral (T sites) as illustrated in Fig. 3.2(a) and (b). The hydrogens were placed randomly in these two type of sites. As shown in Ref.[133], based on a comparative study on hydrogen diffusion in amorphous and crystalline metals, the site preference between octahedral and tetrahedral location does not play a significant role for studying the dynamic behavior of hydrogen, since the migration energy between the two sites is not very high. The structures upon introduction of H were completely relaxed including the volume. Five different systems were studied, with H concentration chosen between 1 to 5 atomic percentage of H. For our study in the concentrated limit, we placed a spherical ϵ-ZrH_2 precipitate of three different sizes (5, 7, and 10 nm diameter) in the Zr matrix as starting configuration as illustrated in Fig. 3.3. The whole structure was completely relaxed afterwards. Note bulk Zr and ZrH_2 have different lattice parameters and have different crystal structures [136]. Keeping this aspect in mind, to prepare the starting configuration, we cut out a spherical volume in bulk Zr as shown in the left panel of Fig. 3.3

where the white region depicts the hollow spherical volume inside the bulk Zr. In the white region, we inserted an equal volume of ZrH_2 sphere in its place. We have tried to match the volume of the precipitate with that of the hollow sphere cut in bulk Zr, instead of matching the number of removed Zr atoms and number of inserted ZrH_2 atoms. No dislocation was pre-constructed at the starting configuration. Initially all the atoms in the simulation cell were relaxed at T = 0 K through energy minimization using the conjugate gradient (CG) method [137]. In the next step, the simulation cells were equilibrated at a temperature of 500 K by using a Nose-Hoover thermostat [138, 139] for 20,000 time steps (20 ps) and further equilibrated under constant pressure and temperature (NPT) condition using Parrinello and Rahman barostat [140] for another 20,000 time steps (20 ps) without any applied strain. A total of 30,00,000 time steps is considered for each run. Finally, the system was subjected to an uniaxial tensile strain along [0001] direction with a constant strain rate of $10^8 s^{-1}$, maintaining a zero-stress condition at the cell boundaries [141, 142] in other two directions [143]. The strain rate parameters were fixed such that the box length expands by 0.01% of its original length every picosecond along the direction [0001] maintaining a zero-stress condition at the transverse direction. The system stress calculated without considering the kinetic energy part, as used in virial definition, is given below:

$$\sigma_{\alpha\beta} = \frac{1}{V} \sum_{i}^{N^*} \sum_{j(\neq i)}^{N} f_{\alpha}^{ij} r_{\beta}^{ij}, \tag{3.1}$$

where f_{α}^{ij} is the force vector between atoms i and j in the direction α, r_β is the distance vector in direction β, N is the number of neighboring atoms for atom i, N^* is the total number of atoms, and V is the simulation cell volume. The volume-averaged stress tensor as defined in Eqn. 3.1 is the same as the global stress used in previous MD simulations [144]. The common neighbor analysis (CNA) [145] is used to identify the atomic structure in terms of atoms having the environment as in FCC, BCC, HCP crystal structure and those not following any specific crystal geometry. Visualization of the atomic configurations was carried out using the Open Visualization Tool (OVITO) [146].

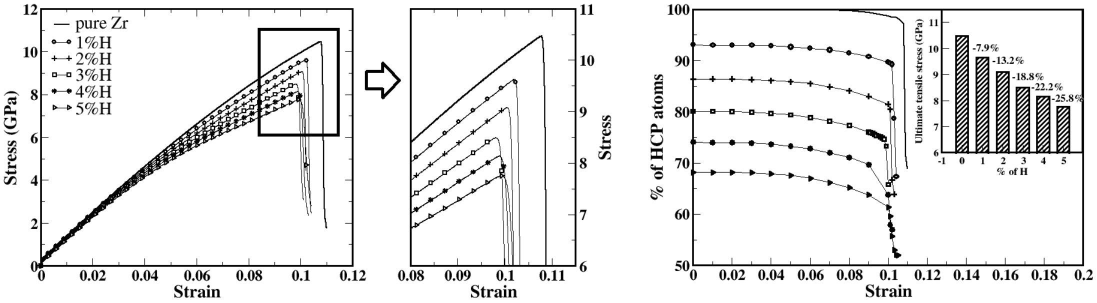

Figure 3.4: Stress-strain plot for pure Zr and Zr with different percentages of H (left panel). Adjacent figure shows the zoom in portion at which the material breaks down for different cases. Percentage of HCP atoms with applied strain alongwith variation of Ultimate Tensile Stress (UTS) for different percentages of H(inset) is shown in right panel.

3.3 Results and Discussions

3.3.1 Dilute limit of H

As the system is heated up from room temperature to higher temperature (∼850 K or above), two major changes happen. As depicted in Fig. 3.1, firstly the HCP Zr undergoes a phase transformation from α-Zr to β-Zr and secondly the solubility for H in α-Zr decreases very sharply. Thus, in order to study the effect of H in HCP Zr (α-Zr phase) the temperature in all of our simulations is set at 500K. Furthermore, since this phase has a maximum solubility limit of 5.93 atomic percentage of H [106], the simulation cell is developed with (1-5) atomic percentages of H.

3.3.1.1 Stress-strain curve

The stress-strain curves with various atomic percentages of H are shown in left panel of Fig. 3.4, along with the case of pure Zr. The linear onset of the curves up to a certain strain indicate the elastic response, whereas for higher strains the curves gradually bend, indicating the onset of plastic deformation. When strain exceeds a certain level, damage in the structure develop and grows until rupture occurs around a strain of about 10%. The precise strain value at which rupture occurs depend on the H concentration (10.8% for pure Zr). It is found that with increase in percentage of H, linear elastic region decreases gradually and the non-linear elastic-plastic region increases, signifying a ductile failure. The strain value at which the material breaks down, the Ultimate Tensile Stress (UTS), decreases as the H content in the simulation cell is increased. This is highlighted in the zoomed in plot in left panel of Fig. 3.4. In order to examine the effect of H, snapshots at different strain level with different percentage of H is studied. Using common neighbor analysis as calculated by OVITO [146], we identify the non-HCP (defected) atoms. Number of non-HCP atoms or defected atoms increase as resistance to accommodate the applied load reduces which in turn relates to the strength of the material [147]. The change in the percentage of HCP atoms with applied strain is shown in right panel of Fig. 3.4. In the hydrogen containing systems, it is seen that the initial number of HCP atoms is not 100% as opposed to the case with pure Zr. This is due to the fact that as H atoms are introduced as interstitials into the pure HCP Zr crystal structure, the local symmetry breaks down and surrounding Zr atoms no longer have HCP coordination. Accordingly, the initial percentage of HCP atoms reduces with increase in percentage of hydrogen content. The reduction of percentage of HCP atoms before the fracture compared to the no-load situation increases as the percentage of H increases. This indicates the fact that the strength of material reduces as more and more H is incorporated into Zr. The inset graph of right panel of Fig. 3.4 shows the percentage decrease of UTS compared to that of pure Zr, with increasing H concentration. It is to be noticed that even 1% inclusion of H into Zr may result in ∼8% reduction in UTS.

3.3.1.2 Microstructure

Investigation of microstructures at several strain values may provide information regarding the deformation mechanisms related to the solute softening effect. In order to examine the microstructure, we cut the system halfway, parallel to the loading direction at different strain values. Through a sequential microstructure analysis for five different cases it is found that as the strain increases, the dislocations become more active producing defected (non-HCP) atoms. Using OVITO,

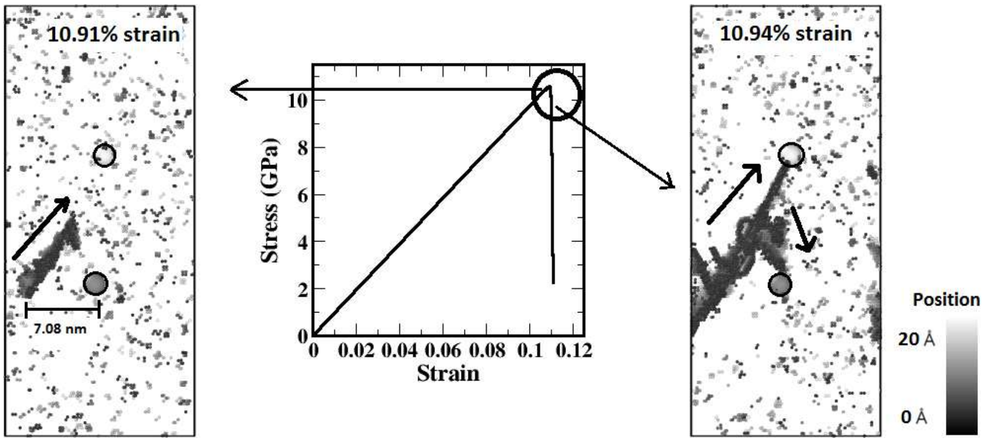

Figure 3.5: Snapshots of the simulation box at two different strain values, just before and after the yielding occurred as encircled in the stress-strain plot. The picture shows only non-HCP atoms, the two H atoms being made artificially bigger in order to distinguish them from other Zr atoms. The grey color coding denotes the proximity of the atoms from the plane of cutting, with black being at the plane of cutting and white being at a distance of 20 Åfrom the plane of cutting, as depicted in the color bar shown by the side.

we find that the dislocations primarily nucleate on prismatic plane along $\langle 1\bar{2}10 \rangle$ direction . Contrary to the general perception that dislocations nucleate at the defected sites, the dislocations are found not to nucleate from the locations where hydrogens are present. All the simulations with different percentages of H in Zr show the same trend. However, once the dislocations are nucleated, it is found that those dislocations get attracted towards nearby H atoms.

To further pinpoint the role of H in dislocation mediated process, atomistic simulation with very few H atoms are performed separately. A snapshot of the atomistic simulation with only two H atoms is shown in Fig. 3.5. It shows only the non-HCP atoms. The two H atoms are made artificially bigger to distinguish them from other atoms. The grey color coding denotes proximity of the atoms to the plane of cutting. The encircled region of the stress-strain graph denotes the strain values at which the snapshots are taken. As seen, dislocation nucleates far from H at 10.91% strain and with increase of strain to 10.94%, the nucleated dislocations are attracted towards the H atoms, as shown by the arrows forming

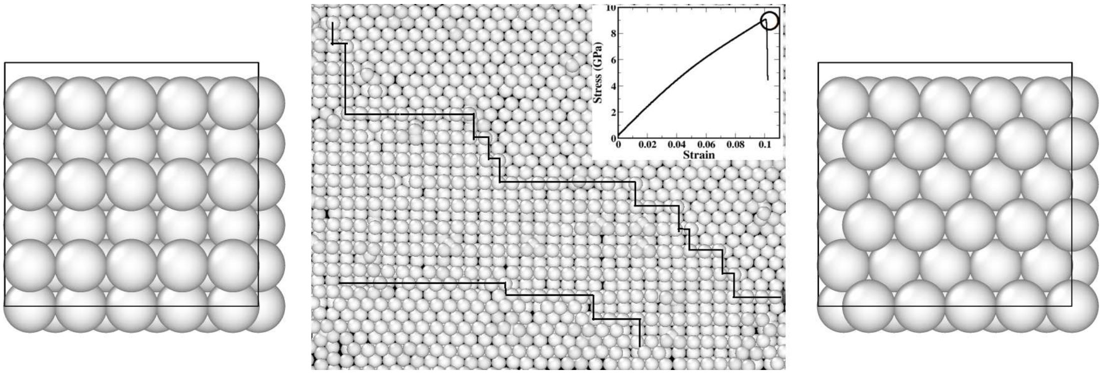

Figure 3.6: Twinning-like lattice reorientation in the prismatic plane, a snapshot taken from the sample with 2% H. The two panels on side left and right depict the atomic arrangement in the prismatic and the basal plane, respectively. The inset shows the strain at which the snapshot is taken.

secondary nucleation centers. We note that the distance from the H atom to the nearest dislocation tip is quite large (more than 5nm). As the applied load is increased, the number of displaced Zr atoms present in the pathway between the dislocation tip and the H atom increases. In such a situation, the dislocation starts interacting with the H atom. A very similar trend is found in all of our simulations in the dilute limit of H inclusion. As the percentage of H atoms in the system increases beyond two H atoms, the interaction of nucleated dislocations with H atoms increases, and the dislocations start getting attracted by the H atoms. Upon reaching the H atom, the dislocation bypasses the H, moving in the same direction.

This analysis emphasizes further that H atoms have no influence in primary dislocation nucleation mechanism, rather influences the dislocation multiplication process. Our finding lends support to the hypothesis that H in solid solution with Zr induces local plasticity, and thus corroborates the hydrogen enhanced local plasticity mechanism.

In order to accommodate the applied load, deformation twinning is a common mode of plastic deformation that occurs in HCP metals, due to their very limited number of slip systems. Twinning generally nucleates in a lenticular shape (Orowan type), and grows with increasing applied load. Here, we observe a very similar twin-like lattice reorientation without an actual twinning plane, similar to what has recently been observed in magnesium [148]. In all the cases with and without H we observe this twin-like re-orientation of atoms as shown in the central panel of Fig. 3.6. It shows a snapshot of the system with 2% H near the fracture point. The left and the right figures show the prismatic and basal plane atomic arrangements, respectively. Observation reveals that the boundary between the parent lattice (prismatic plane) and the 'twinned' lattice (basal plane) is composed predominantly of semi-coherent basal/prismatic interfaces instead of the twinning plane. The migration of this boundary is dominated by the movement of these interfaces undergoing basal/prismatic transformation via local rearrangements of atoms when a sufficiently high tensile stress is applied. The details of the atomic rearrangement for lattice reorientation in our case is different than what has been reported earlier for Mg [148]. A close monitoring of these atomic arrangements, reveal that the shifting of alternate prismatic planes along $\langle 1\bar{2}10 \rangle$ give rise to such basal plane like atomic arrangement. We propose that this shifting mechanism will be energetically more favorable than the earlier reported mechanism involving complex atomic shuffling [148]. Detailed study on such twin like lattice reorientation is beyond the scope of present work and will be taken up in future.

3.3.1.3 Quantitative Analysis

As understood, the degradation in Zr-H solid solution is governed by nucleation of defected atoms, followed by their growth process towards ultimate failure of the material. In order to achieve further understanding of such degradation mechanism in a quantitative manner, we use the Kolmogorov-Johnson-Mehl-Avrami (KJMA) equation [149, 150]. Few recent studies of irradiation-induced defects in metals have used KJMA equation [151, 152]. The present study is one of the few attempts to quantify the degradation mechanism of a metallic system using the KJMA equation. The KJMA equation is given by:

$$f = 1 - \exp^{-kt^n},$$

where, f is the volume fraction of the transformed (defected) phase, t is the time, n is the nucleation rate and k denotes the growth of the transformed phase.

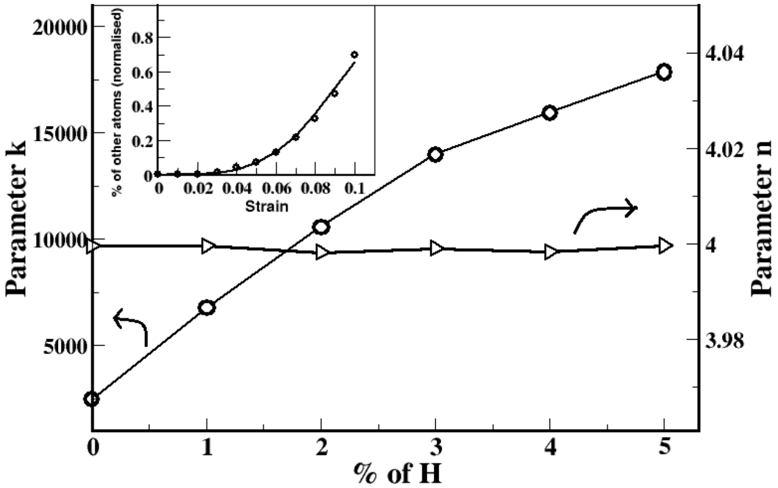

Figure 3.7: Variation of parameters k and n with different percentages of H in bulk Zr, obtained using the Kolmogorov-Johnson-Mehl- Avrami (KJMA) equation. The inset shows the fitting of k and n with the evolution of dislocated atoms for 2%H in Zr as a representative case.

With reference to the present study, the percentage of atoms that are dislocated or displaced is considered as the transformed phase and the increasing strain plays the role of "t".

For each H containing system, the number of dislocated atoms first nucleate, then monotonically increase with increasing strain and finally saturate at the fracture point. Using standard fitting tools, we fit the evolution of non-HCP atoms at different strain values to the KJMA equation to obtain the values of k and n, as shown in the inset of Fig. 3.7 for a representative case of 2% H in Zr. Fig. 3.7 plots the variation of parameter k, representing the growth of the dislocated atoms and n, the nucleation rate as a function of the percentage of H. We find, while the parameter k increases monotonically with increase in the percentage of H, the parameter n, remains almost constant. Thus, H does not play much role in dislocation nucleation but strongly influence the dislocation multiplication process. This is in conformity with the inference drawn from microstructure analysis.

3.3.2 Concentrated limit of H

This section focuses on the effect of H in the concentrated limit which forms ϵ-ZrH_2 phase inside the bulk Zr. The ϵ-ZrH_2 has a face-centred tetragonal structure with 12 atoms per unit cell as shown in Fig. 3.1(c). In the concentrated limit, the simulation cell is prepared as follows: a spherical volume is cut out from bulk Zr, located at the center of the simulation box, and a spherical volume of ϵ-ZrH_2 of the same size is inserted at that place. Three different sizes of the precipitate are studied: 5nm, 7nm and 10nm in diameters respectively, while the parent Zr dimension remains the same as before ($20.67 \times 20.70 \times 41.22\ nm^3$).

3.3.2.1 Stress-strain curve

The effect of ϵ-ZrH_2 precipitate inside bulk Zr on the stress-strain curve is shown in the left panel of Fig. 3.8. In the figure we also show the stress-strain curve for Zr with 5% H to compare the nature of the curves in the dilute and concentrated limit. For all the three sizes of the precipitate, the nature of the stress-strain curves does not alter much from the parent Zr case, except for the decrement in UTS occurring at much lower strain values, indicating a brittle-like fracture. Compared to the dilute limit of H, where the stress-strain curves denote a ductile behavior in terms of the deviation from the linear nature of stress-strain curve, in the concentrated limit the stress-strain curves indicate brittle-like fracture maintaining the linear behavior until large strain values. It is found that with increase in the diameter of the precipitate, the strain value at which the material breaks down decreases. The main cause of the brittle nature of the fracture in the concentrated limit is the influence of precipitate on the cohesion of precipitate-matrix interface. As size of the precipitate gets bigger, the interface area increases, which in turn increases the chance of interfacial crack nucleation and thus the UTS decreases. Our observation suggests that in the concentrated limit of H, the hydrogen enhanced decohesion mechanism is instrumental for Zr degradation. In order to examine the effect of the precipitate-size, snapshots at different strain levels with different sizes of the precipitate are studied. Similar to the previous case of dilute limit, using common neighbor analysis, we identify the non-HCP atoms. The change in the percentage of HCP atoms in bulk Zr with applied strain

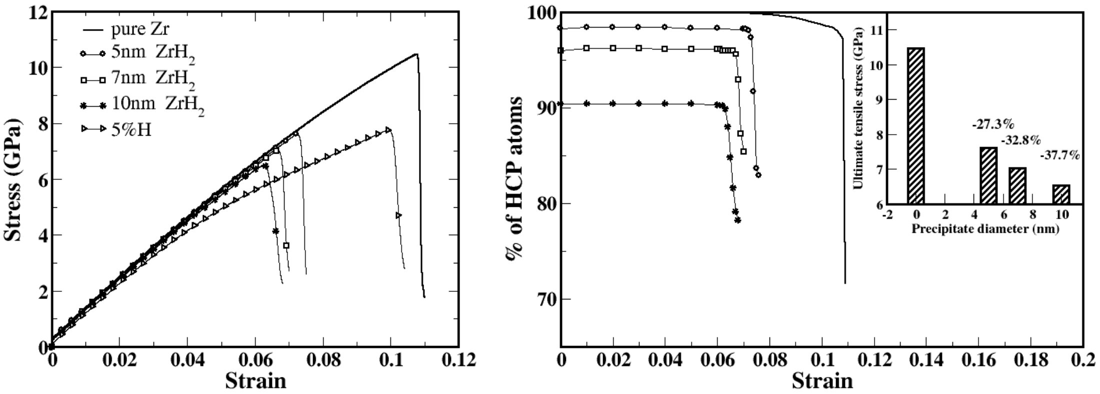

Figure 3.8: Stress-strain plot for pure Zr and Zr with different ZrH_2 precipitate diameters. The representative solid solution case with 5% H is also shown for comparison between the two limits (left panel). Variation of percentage of HCP atoms with applied strain along with Ultimate Tensile Stress (UTS) (inset) for different precipitate diameters is shown in right panel.

is shown in right panel of Fig. 3.8. The relative reduction of the percentage of HCP atoms indicate the fact that the strength of material reduces by incorporating precipitate. The inset in right panel of Fig. 3.8 shows the percentage decrease of UTS with increasing diameter of precipitate. It may be noticed that even with 2 nm diameter precipitate, which amounts to a ratio of precipitate volume and matrix volume of 0.002, may result into more than 25% of reduction in UTS. This may be compared with similar deleterious effect with 5% H in solid solution that results in 25.8% reduction in UTS.

3.3.2.2 Microstructure & Quantitative Analysis

A detailed micro-structure analysis similar to that in the dilute limit, is carried out in the concentrated limit to reveal the role of ZrH_2 precipitate in deformation mechanism. In all the simulations of Zr with its hydride under tensile load, the nucleation of dislocations are found to initiate at the precipitate-matrix interface. Once dislocations are accumulated, cracks are generated at the interface that lead towards ultimate failure of the material. A snapshot of the atomistic simulation with a ZrH_2 precipitate of 5nm in diameter is shown in Fig. 3.9, as a representative

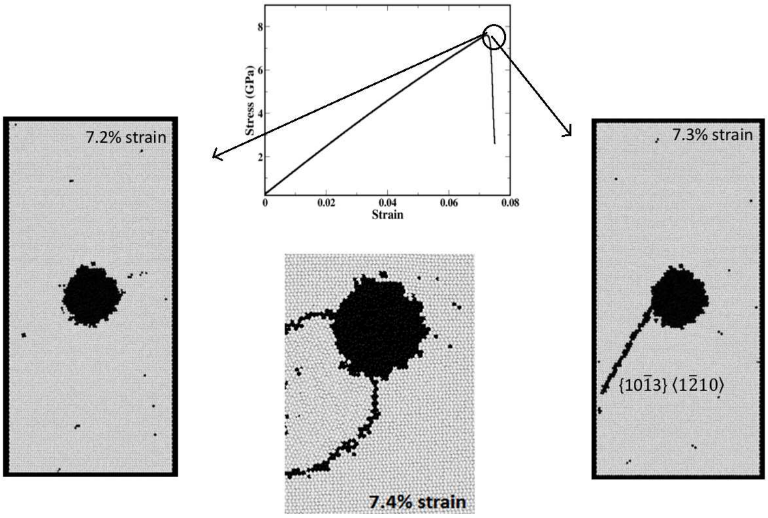

Figure 3.9: Snapshot of the simulation cell with precipitate diameter of 5nm, shown at two different strain values. The dislocation nucleates in the prismatic plane along $\langle 1\bar{2}10\rangle$ direction as strain is increased from 7.2% (left panel) to 7.3% (right panel). The dislocation loops are observed at higher strain values which is shown in the middle panel.

case. The simulation cell is sliced at the middle to reveal the embedded precipitate. The encircled area of the stress-strain curve highlight the strain values at which the two snapshots are taken. At 7.3% strain, dislocations are observed to nucleate from the precipitate-matrix interface in the prismatic plane along the $\langle 1\bar{2}10\rangle$ direction. The direction in which the dislocations nucleate is calculated by using OVITO. Dislocation loops on prismatic plane is observed at higher strain values as shown in the figure. Twinning like lattice reorientation, similar to what has been found in the dilute limit, is also observed in the concentrated limit.

The KJMA plots, as shown in Fig. 3.10, reflect the fact that both the parameters k and n increase with increase in the precipitate diameter. This can be understood from the fact that as the diameter of the precipitate increases, the interfacial area of ZrH_2 with Zr matrix increases, which essentially enhances the number of available sites to nucleate a dislocation or crack. Compared to the dilute limit where the role of H is confined only in the dislocation multiplica-

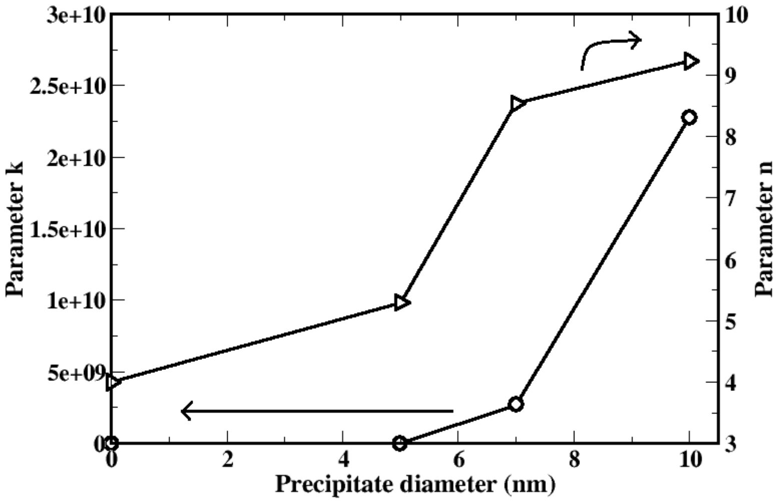

Figure 3.10: Variation of *k* and *n* parameters for Zr with varying diameter of ZrH_2 precipitate, obtained using the KJMA equation.

tion process, the KJMA plots in the concentrated limit indicate the role of the precipitate size in both dislocation nucleation and growth mechanisms.

3.4 Summary

The deformation mechanisms of Zr due to H inclusion in the dilute and concentrated limits were studied using large scale atomistic simulations. The salient points of our findings are summarized below :

- In the dilute limit of H, dislocations nucleate far from H atoms. However, the nucleated dislocations are attracted towards the H atoms. This implies that H atoms in solid solution with Zr helps in dislocation multiplication. Our atomistic simulations to this end support the HELP mechanism for Zr degradation. On the other hand, in the concentrated limit of H, dislocations are observed to nucleate from the precipitate-matrix interface. Accordingly, as precipitate volume fraction increases, the inter-facial area and the probability to nucleate such dislocation increases. At higher concentrations, our simulation indicates the decohesion mechanism as primary mechanism for Zr degradation.

- The H atoms in solid solution enhances the local plasticity leading towards a ductile fracture, in contrast ZrH_2 precipitate in bulk Zr reduces the overall strength of the material which makes the material undergo a brittle fracture.
- Prismatic dislocations were observed in both the limits. Dislocation loops were observed near the precipitate matrix interface in the concentrated limit.
- Twin-like lattice reorientation was observed in both the limits of H inclusion.
- KJMA equation, introduced for the first time to identify the nucleation and growth process of the dislocated atoms in a metallic system, provided quantitative support to the above conclusions.

Chapter 4

Soft MAX phases with Boron-substitution: A Computational Prediction

4.1 Introduction

The MAX phases are a new class of layered solids, having general formula $M_{n+1}AX_n$ with n varying form 1 to 3, as has been already introduced in Chapter 1. As discussed $M_{n+1}X_n$ layers are interleaved with pure A-group element layers (A is a group III or IV element, and X is C and/or N), this laminate structure of MAX phase being responsible to make them machinable, damage tolerant, corrosion resistive and also good thermal and electrical conductors [153]. Many studies have been carried out to investigate different aspects of these materials, some of which have been summarized in Chapter 1. Although there exists different studies both in experimental, and theoretical front, the detailed theoretical studies of mechanical properties are very few. The understanding and tailoring of mechanical properties of this technologically important class of compounds are

---

This chapter is based on "Soft MAX phases with Boron-substitution: A Computational Prediction" - *Poulami Chakraborty*, Aurab Chakrabarty, Amlan Dutta and Tanusri Saha-Dasgupta, (communicated).

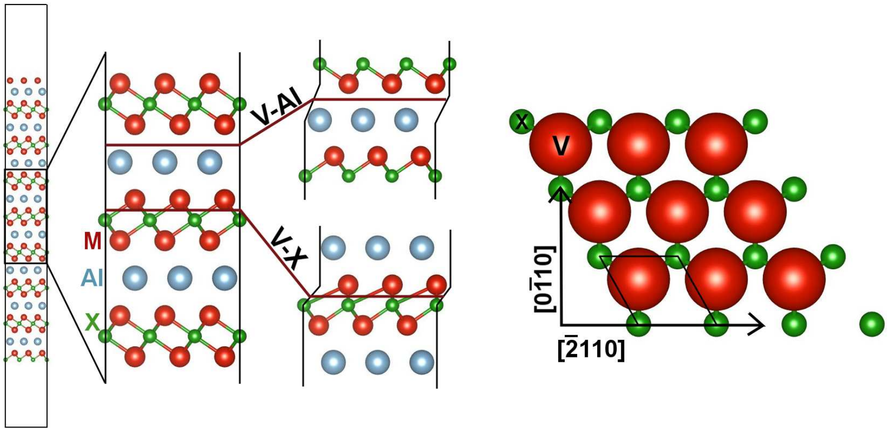

Figure 4.1: Left panel: Crystal structure of V_2AlX (X= C/B) MAX phase with the two slip planes highlighted in the zoomed picture. Right panel: The top view of the structure in the [0$\bar{1}$10]-[$\bar{2}$110] plane. Marked in the figure is the hexagonal unit cell.

intimately connected to the knowledge of the dislocation behaviour. The difference in the bonding characteristic between different atomic layers of MAX phase leads to drastic inhomogeneity in the basal slips for different layers. In the MAX phase geometry, the transition metal M and group IV/V element X are bound with a strong covalent bond. A basal slip between the M and X layer is therefore energetically expensive and practically improbable. On the other hand the M-A bond is of a softer nature and a slip between the M and A layers is more common [154, 155, 156, 157]. In this work, we report the mechanical properties of a representative MAX phase, namely V_2AlC compound, and explore possible tailoring of its mechanical properties. In particular, we computed the generalized stacking fault energies at T=0K. The finite temperature free energies were used to deduce the temperature effect in the T=0K properties. In addition, Peierls-Nabarro (PN) modeling was used to access core structure of dislocations.

In the M_2AX (211) compounds, which is the largest family of MAX phase and the focus of this work, the three constituents are stacked as M-X-M-A. The M and X atoms form a close-packed M_6X octahedra (See left panel in Fig. 4.1) which binds the M and X layers firmly. Therefore, one of the keys to tailor the mechanical properties would be to substitute the M and X with elements that are of similar ionic size but with significantly different chemical characteristics. One such possibility can be use of group III element which shares the same row as IV or V (*e.g.* B instead of C or N). Boron forms weaker covalent bond compared to that of C or N, and it has been found previously that substituting B for C can dramatically alter the properties [158, 159]. Properties of carbides and nitrides that constitute known 211 MAX phases are explored to a reasonable extent [40, 154]. However, a boride has never been tested as a MAX phase. This would open up possible creation of new MAX phases with varied physical properties. In the present study, using combination of *ab-initio* and model calculations, we explored the effect of B substitution for C on mechanical properties of 211 MAX phase for the representative case of V_2AlC. The MAX phase compound V_2AlC was synthesized in bulk form back in 2004 [160], by isostatic pressing of V, Al and C, and its elastic properties have been studied to a good extent [27, 161, 162, 163]. The prediction on boron substitution in V_2AlC thus can be readily checked.

4.2 Computational Details

The *ab-initio* calculations were carried out in plane-wave basis using projector augmented wave (PAW) potentials [164]. The exchange-correlation functional was chosen to be that of Generalized Gradient Approximation (GGA) as implemented in the Perdew-Burke-Ernzerhof (PBE-GGA) formalism [93]. A plane-wave cut-off of 500 eV was found to be sufficient to achieve force convergence of 0.001 eV/Å and total energy convergence of 10^{-8} eV. A slab supercell of dimension 1×1×4 with 32 atoms, in standard hexagonal crystallographic vectors, X = $[\bar{2}110]$, Y = $[1\bar{2}10]$, Z = [0001] was created, which was separated by 20 Å of vacuum from its periodic image, to calculate the generalized stacking fault energies (GSFE). A displacement was introduced on a specific basal plane, such that the part of the supercell above this plane glides over the stationary bottom part. The glide planes were chosen to be the ones between V and Al, and V and X atomic layers as shown in Fig. 4.1. The GSFE was computed as the total energy difference between the un-faulted and faulted systems, defined per unit area of the glide plane. This exercise was carried out systematically for displacements over a fine grid of 18×10 points in the basal planes (0001) at two different cutting levels of

V-X (X=C/B) and V-Al to obtain the stacking fault energy surfaces, defined as γ-surface by Vitek [165]. GSFE along the γ-line $[0\bar{1}10]$ was calculated specifically for a quantitative comparison of shearing at two cutting levels and that between boride and carbide.

The continuum model of plastic deformation proposed by Peierls [102] and refined by Nabarro [103] was used to analyze the *ab-initio* computed γ-surface and to predict characteristics, like Peierls stress and core structure of slip dislocations in different basal planes of the MAX phases.

The model expresses the energy cost associated with a dislocation as a functional of a disregistry function $u(x)$. The total energy cost for dislocation can be split into two parts, i.e. the elastic and misfit energies.

$$E[u(x)] = E_{el}[u(x)] + E_{mis}[u(x)] \tag{4.1}$$

where,

$$E_{el}[u(x)] = -K\int_{\infty}^{\infty}\int_{\infty}^{\infty} \rho(x)\rho(x')ln(x-x')dxdx'$$

and

$$E_{mis}[u(x)] = \int_{\infty}^{\infty} \gamma[u(x)]dx$$

$\rho(x) = \frac{du(x)}{dx}$ and $\gamma[u(x)]$ is the γ-surface obtained as a function of the basal plane vector. The disregistry function $u(x)$ was chosen, following the Volterra model of straight edge dislocation [166] as,

$$u_x(x) = \frac{b}{\pi}\big[A_1v_1(x) + A_2v_2(x)\big] - \frac{b}{2}sin\theta \tag{4.2}$$

$$u_z(x) = \frac{b}{\pi}\big[A_3v_3(x) + A_4v_4(x)\big] - \frac{b}{2}cos\theta \tag{4.3}$$

$$v_i(x) = atan\Big(\frac{x-x_i}{c_i}\Big); \quad i = 1,2,3,4 \tag{4.4}$$

$u(x)$ was solved numerically by minimizing $E[u(x)]$ in Eqn.(4.1) with constraints $A_1 + A_2 = sin\theta$ and $A_3 + A_4 = cos\theta$, θ being the angle of dislocation. The theoretical concept of Peierls stress σ_p,[102] which describes the minimum shear stress required to initiate dislocation at 0K, was computed by considering an additional term [18], $\sigma\int_{\infty}^{\infty} u_x(x')dx'$ in Eqn.(4.1), and finding the maximum of value of σ (σ_p) exceeding which no stable core solution of the problem can be obtained.

To compute the temperature dependency of the stacking fault, finite temperature calculations were carried out. The effect of anharmonic phonon was neglected, which was shown to be of negligible contribution upto a temperature of 80% of melting point. Under the assumption that the thermal expansion coefficient of a material remains invariant upon introduction of fault, the effect of finite temperature on faults can be expressed in terms of Helmholtz free energy, by adding ionic vibration to the total energy [167], $F(T) = E_0 + \frac{k_{BT}}{N_q} \sum_{i,q} ln \Big[2sinh \frac{\hbar\omega_{i,q}}{2k_B T} \Big]$ where, N_q is the number of **q**-points on a (48×48×12) mesh in the Brillouin zone, and $\omega_{i,q}$ is the frequency of the i-th phonon mode at wave vector q.

4.3 Results

4.3.1 Elastic Constants

We start our discussion with calculated elastic properties, for the synthesized V_2AlC (VAC) compound, and the proposed boron compound, V_2AlB (VAB). VAB was found to have slightly larger lattice parameters of a=2.962 Å, c=13.410 Å, than that of V_2AlC (a=2.927 Å, c=13.252 Å). The formation enthalpy (ΔH_f), defined as the total energy difference of the MAX phase and the sum of the total energies of the individual elements in their native state, was calculated to be -1.34 eV and -1.99 eV for VAB and VAC, respectively. This confirms the stability of boron phase to be formed. The five independent elastic constants for hexagonal lattice of VAB in comparison to VAC, along with their bulk and shear moduli, are listed in Table 4.1. The calculated bulk modulus (B) value of 173 GPa of VAC is consistent with other *ab-initio* estimates (175-197 GPa)[27, 161, 162] and the value obtained from measurement of sound velocity [163]. We note that B substitution for C reduces the bulk modulus by more than 9% which reflects weakening of the lattice following weakening of the M-X covalent bond. The shear modulus (G) also shows about 14% suppression in B compound compared to C compound. A good measure of machinability [168] is B/C_{44} and that of

Table 4.1: Elastic constants(C_{ij}), bulk (B) and shear moduli (G) of V_2AlB and V_2AlC. All values are in GPa.

	C_{11}	C_{12}	C_{13}	C_{33}	C_{44}	B	G
V_2AlC	330	74	107	321	149	173	132
V_2AlB	285	86	97	278	120	157	113

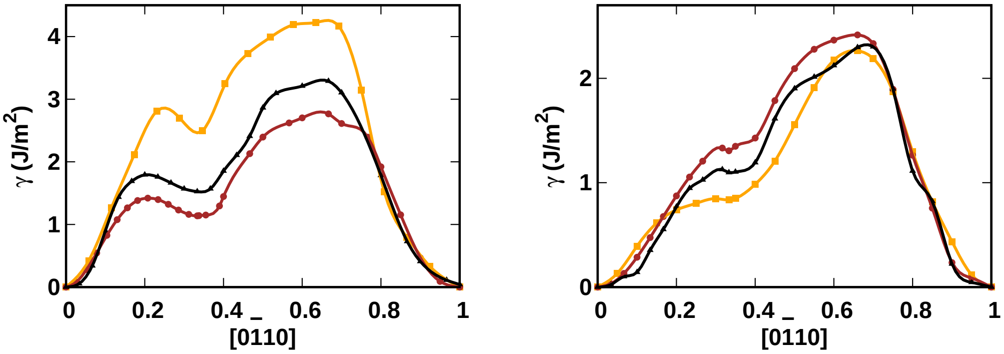

Figure 4.2: The GSFE on V-X (left) and V-Al (right) plane for V_2AlB (brown), V_2AlC (orange), and $V_2Al(C_{0.5},B_{0.5})$ (black) along $[0\bar{1}10]$. The GSFE contains a stable stacking fault at $\frac{\mathbf{b}}{3}$.

ductility is B/G [169]. Following this, boride compound is expected to be more machinable as well as more ductile than carbide.

4.3.2 Dislocation Properties at T = 0K

A slip in the basal plane in the layered MAX phase resembles a stacking fault with two partials on either side [165]. Therefore the misfit energy associated with it can be termed as stacking fault energy (SFE), while the stacking fault energy associated with all possible translational slips in a particular plane is known as generalized stacking fault energy (GSFE).

During a slip along the $[0\bar{1}10]$ direction, the system encounters a high-symmetry configuration at translation $\mathbf{b}/3$; $\mathbf{b}$ being the Burgers vector in the $[0\bar{1}10]$ direction. In this case, the atoms of the slipping partial rest on symmetric 'voids' of the static partial (cf. right panel in Fig. 4.1). As a result, the GSFE exhibits a local minimum at this configuration, commonly known as the stable stacking

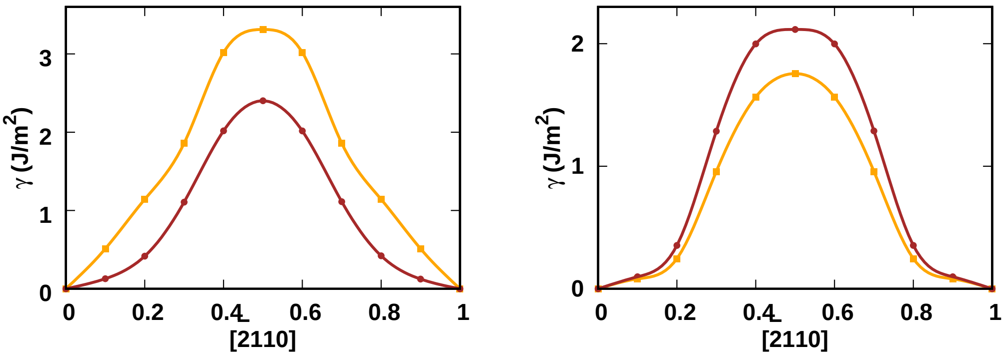

Figure 4.3: The GSFE for the V-X (left) and the V-Al (right) plane for V_2AlB (brown) and V_2AlC (orange) along $[\bar{2}110]$.

fault (SSF) [165]. The energy barrier that precedes the SSFE is named the unstable stacking fault energy (USFE) [170]. Note that the SSF is only observed at $\frac{1}{3}[0\bar{1}10](0001)$ on the γ-surface and is therefore of significant importance in determining the quantitative character of the plastic deformation.

Fig. 4.2 show the plot of the calculated γ-line along $[0\bar{1}10]$ for the two cut levels, M-X (left) and M-A (right) for the carbide and boride compounds. We also show the result for the solid solution of two compounds, namely $V_2Al(C_{0.5},B_{0.5})$. The SSF energy (γ_{SSF}) of VAC, which serves as a key parameter in the characterization of plastic deformation [165, 170], is found to be much larger in the V-C plane (2.39 J/m^2) compared to that in the V-Al plane (0.91 J/m^2), a feature that is observed in other carbide/nitride MAX phases as well [157]. A remarkable change happens upon substitution of C by B. This reduces the stacking fault energy of the M-X drastically by a factor of 1.5-2. The stacking fault energy of the M-A cut on the other hand, remains more or less unaffected. This in turn makes the stacking fault energy of the two cut planes comparable for 100% B-substituted compound, VAB, energies corresponding to SSF of V-B and V-Al planes being 1.1 J/m^2 and 1.3 J/m^2, respectively. Note that the SSF is only observed at $\frac{1}{3}[0\bar{1}10](0001)$ on the γ-surface. The direction perpendicular to it is $[\bar{2}110]$. The GSFE in this direction is shown in Fig. 4.3. The Coulomb repulsion of the gliding ions has yielded a single barrier which, in magnitude, follow the same trend as Fig. 4.2. All the other γ-lines between these two extremes are shown in figures 4.2 and 4.3 are assembled in the γ-surface plots shown in Fig. 4.4.

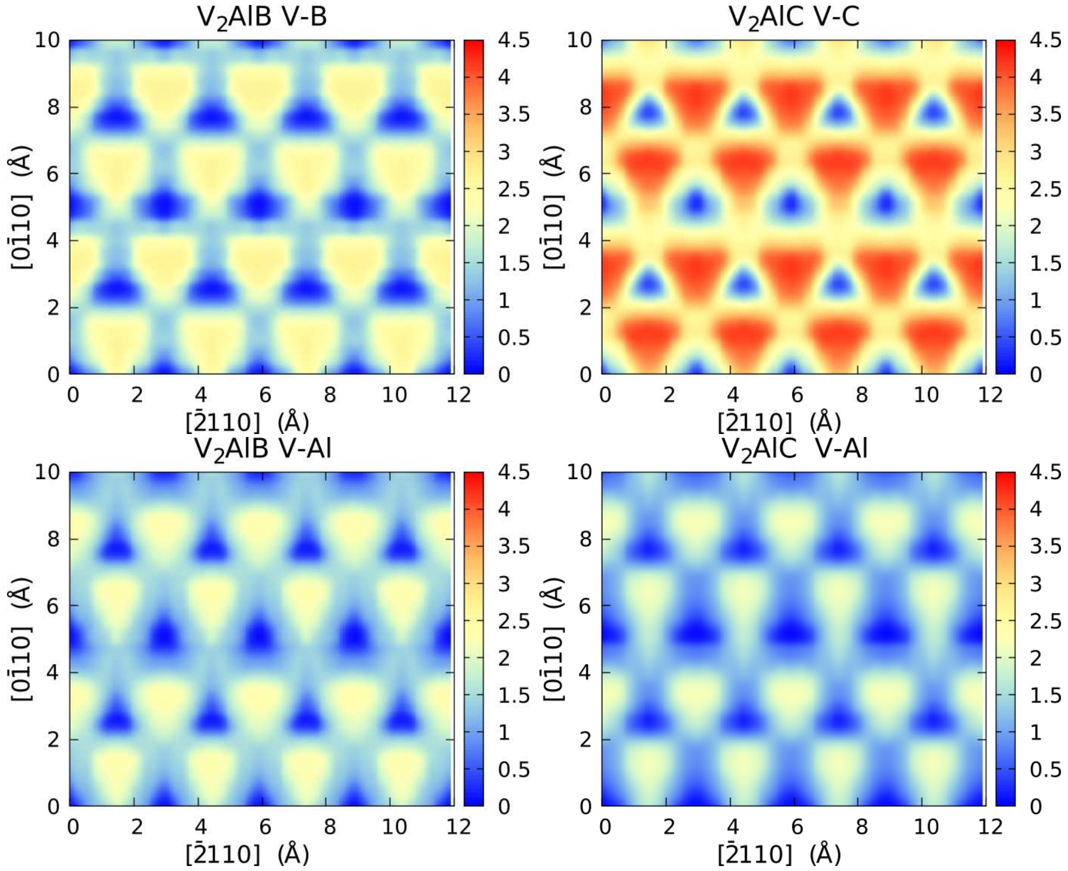

Figure 4.4: The γ-surface of the V-X plane(top) and V-Al plane(bottom) for V_2AlB and V_2AlC .

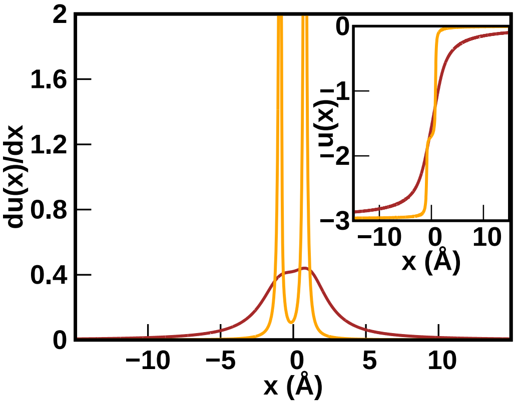

Figure 4.5: Plot of the disregistry function u(x) (inset) and its derivative du(x)/dx along the screw direction for V-X (0001) basal plane in V_2AlC (orange) and V_2AlB (brown).

In order to characterize the full dislocation core structures in C and B compounds, all significant dislocation characters (0° (Screw), 30°, 60°, 90° (Edge)) defined as the angle between the dislocation line and the Burgers vector needs to be computed. This gives rise to the so-called γ-surface plot which contains the information of GSFE in the [$0\bar{1}10$]-[$\bar{2}110$] plane. Fig. 4.4 show such plots for the M-X (0001) basal plane (top) and M-Al (0001) basal plane (bottom). Comparison of the plots reveals significant suppression of stacking fault energy for M-X layer upon replacement of C by B whereas not much change is observed for M-Al cut plane, as already concluded from γ-line plot along [$0\bar{1}10$]. Additionally, we find a qualitative difference in the dislocation core structure of the two compounds, it being much more diffuse for VAB as opposed to sharp structure in case of VAC. In order to have a quantitative analysis of this general observation, the dislocation core parameters were obtained with a variational model based on the Peierls-Nabarro formalism. The core structure in this model, as presented in section 4.2, is expressed in terms of disregistry function $u(x)$ where x is in the direction of specific dislocation line. The full width at half-maximum of the derivative of the disregistry function $u(x)$ represent the width of the dislocation core. The plot of $u(x)$ for VAC and VAB as well as derivative of $u(x)$ is shown in Fig. 4.5 for the screw direction. We find there is a marked difference in behavior between VAC and VAB. A full dislocation is normally dissociated into two partial dislocations and these partials are separated by stacking fault width (Δ). Fig. 4.5 displays the local dislocation density, $\rho(x) = du(x)/dx$, and the corresponding disregistry function, $u(x)$, for screw dislocations in both VAC and VAB. $du(x)/dx$ is found to be a two peaked structure for VAC, with the spread of the two partials, measured in terms of half-widths (ξ_1 and ξ_2) being non-overlapping, while $du(x)/dx$ is found to be a single peaked structure for VAB, with the overlapping spread of the two partials. The same trend is observed for other dislocation directions as well, as summarized in Table. 4.2. We find that both in case of VAB and VAC the stacking fault width (Δ) is about 2 Å, which is too small for individual partial dislocations to be resolved in transmission electron microscopy (TEM), the typical resolution being few nanometers. The dislocations are thus expected to appear as perfect dislocations, as reported in TEM studies of other MAX compounds [155]. The effect of replacing carbon by boron is immediately visible in terms of significant increase in widths of the peaks in $\rho(x)$, which correspondingly indicates a wider dislocation core. In the conventional analytical formulations, the Peierls stress varies as $\sim e^{-4\pi\zeta/b}$, where ζ and b are the core width and Burgers vector, respectively. Peierls stress quantifies the lattice resistance to dislocation motion and hence is an important factor dictating the mobility of a dislocation. As is seen from Table. 4.2, σ_p for M-A plane for VAB is only 2-6 % smaller than that of VAC, while σ_p for M-X plane for VAB shows a large decrease compared to VAC, by about 40-50%. Our T = 0 K results thus suggest a qualitative difference in the mechanical behavior of the two compounds at low temperature, with possibility of activation of two basal slip systems in VAB against a single slip system in VAC. VAB therefore should exhibit larger strain rate than VAC under identical conditions of loading; in other words, should be more ductile.

In order to understand the difference in the dislocation characteristics between the boride and the carbide MAX phases, one must comprehend the nature of the bonds across the consecutive slip planes. We estimated the bond strength between M-X and M-Al pairs by calculating the crystal orbital Hamiltonian population (COHP). The COHP is defined as the density of states weighted by the corresponding Hamiltonian matrix element. This is a tool that permits energy-resolved analysis of pairwise interactions between atoms. Table. 4.3 lists the

Table 4.2: The calculated half-widths of the two partials (ξ_1 and ξ_2), separation of the partials (Δ) and the Peierls stress (σ_p) for the different glide planes in VAC, characterized by different dislocation angles θ. The corresponding values of the calculated parameters for V_2AlB are given in parentheses. The last column lists the percentage decrease in Peierls stress ($\Delta\sigma_p$) for V_2AlB with respect to that of V_2AlC.

θ	ξ_1 (Å)	ξ_2 (Å)	Δ (Å)	σ_p (MPa)	$\Delta\sigma_p$(%)
V-X (X=B/C) plane					
0(Screw)°	0.11(1.5)	0.11(1.5)	1.6(2.1)	1450(718)	50.48
30°	0.10(1.9)	0.11(1.8)	1.5(1.9)	1700(842)	50.47
60°	0.18(1.8)	0.16(1.6)	1.5(2.0)	1550(970)	37.42
90(Edge)°	0.14(2.1)	0.14(2.1)	1.6(1.9)	1650(797)	51.69
V-Al plane					
0(Screw)°	1.9(1.6)	1.9(1.6)	1.9(2.2)	755(710)	5.96
30°	2.0(1.9)	2.0(2.0)	1.8(1.9)	835(815)	2.39
60°	2.1(2.1)	1.9(2.1)	1.7(2.1)	820(805)	1.82
90(Edge)°	2.2(1.8)	2.2(1.8)	2.0(1.7)	840(810)	3.57

COHPs for M-A and M-X bonds energy integrated until Fermi energy (ICOHP). The stable stacking fault energies are also listed to show a correspondence between ICOHP and γ_{SSF}. As is evident V-B bond is much weaker than the V-C bond, V-B bond-length being larger than V-C bond. This correlates with the fact that the γ_{SSF} in M-X plane of VAB is significantly lower than that in M-X plane of VAC. The weakening of V-B bond in VAB compared to V-C bond in VAC is further evident in the charge density plots presented in left panel of Fig. 4.6. The computed phonon band structure of the two compounds, presented in right panel of Fig. 4.6 supports the same. Appreciable softening of phonon modes is observed for VAB as compared to VAC, the effect being most pronounced for the lowest acoustic branches.

Similar studies involving bonding characteristics of boride and carbide were done with neighbouring atom Ti. The bond strength between its M-X and M-Al pairs were evaluated. M-B bond being weaker than M-C bond, this trend is found

Table 4.3: Estimate of pairwise bond strengths obtained with ICOHP. The bond lengths and γ_{SSF} associated with the plane across the pair of atoms are also given.

	V_2AlB		V_2AlC		Ti_2AlB		Ti_2AlC	
Plane	V-B	V-Al	V-C	V-Al	Ti-B	Ti-Al	Ti-C	Ti-Al
ICOHP (eV)	-3.17	-1.68	-3.49	-1.45	-2.57	-1.10	-2.92	-1.15
Bond legth (Å)	2.075	2.739	2.016	2.737	2.189	2.935	2.111	2.894
γ_{SSF} (J/m^2)	1.138	1.305	2.391	0.905	1.122	0.755	1.454	1.055

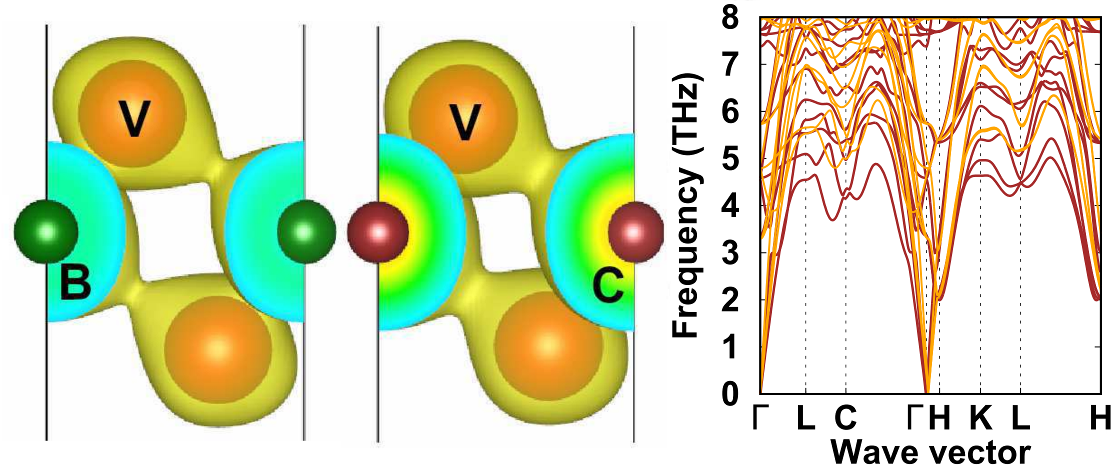

Figure 4.6: Left panel: The plot of calculated charge density for V_2AlB and V_2AlC. The isosurface value is chosen at 0.07 $e^-/\AA^3$. Right panel: The phonon band structure of V_2AlB (in brown) in comparison to that of V_2AlC (in orange).

to hold good even for Ti_2AlB and Ti_2AlC as shown in Table 4.3. Stacking fault energy calculations were also done to evaluate the change in the correspondence between ICOHP and γ_{SSF} when the M atom is changed in M_2AlX i.e. V is replaced by Ti. In case of Ti also, γ_{SSF} in M-X plane of boride is found to be lower than that in M-X plane of its carbide. The one to one correspondence between the bond strength and the γ_{SSF} was found to be consistent. Thus softening of M-X bond with X = B holds true even with the substitution of M in MAX phases.

4.3.3 Dislocation Properties at Finite Temperature

Table 4.4: Stacking fault energies at stable (SSF) and unstable stacking faults (USF) without vibrational contribution in comparison to that at 750K and 1500K.

	V_2AlB		V_2AlC	
	V-B	V-Al	V-C	V-Al
	Without vibrational contribution			
γ_{SSF}	1.138	1.305	2.391	0.905
γ_{USF}	1.421	1.332	2.813	0.922
$\gamma_{SSF}/\gamma_{USF}$	0.800	0.979	0.849	0.981
	With vibrational contribution at 750K			
γ_{SSF}	0.981	1.133	2.267	0.829
γ_{USF}	1.303	1.132	2.689	0.846
$\gamma_{SSF}/\gamma_{USF}$	0.753	1.001	0.843	0.980
	With vibrational contribution at 1500K			
γ_{SSF}	0.832	0.988	2.182	0.754
γ_{USF}	1.289	0.964	2.604	0.771
$\gamma_{SSF}/\gamma_{USF}$	0.645	-	0.838	0.978

Finally, it is important to study the influence of temperature. SFE at finite temperatures are calculated by adding the vibrational free energy to the the DFT total energy. The harmonic approximation is computationally expensive and therefore only the energies associated with the unstable and stable stacking faults, i.e. γ_{USF} and γ_{SSF} are calculated. Table 4.4 lists the γ_{SSF}, γ_{USF} and their ratio $\frac{\gamma_{SSF}}{\gamma_{USF}}$. Fig. 4.7 shows the temperature evolution of $\Gamma_{SSF}/\Gamma_{USF}$, where Γ_{SSF} and Γ_{USF} are the free energy corresponding to SSF and USF for the M-X and M-A planes for VAC and VAB compounds. Interestingly, we find while this ratio, is more or less temperature independent for the carbide compound, it shows significant temperature dependence for the boride compound. Even more interestingly, we find that the temperature dependence of $\Gamma_{SSF}/\Gamma_{USF}$ in VAB to be opposite between the V-Al and V-B planes. The value of $\Gamma_{SSF}/\Gamma_{USF}$ for V-B plane decreases from a value of 0.8 at 0 K to a value of 0.65 at 1500 K,

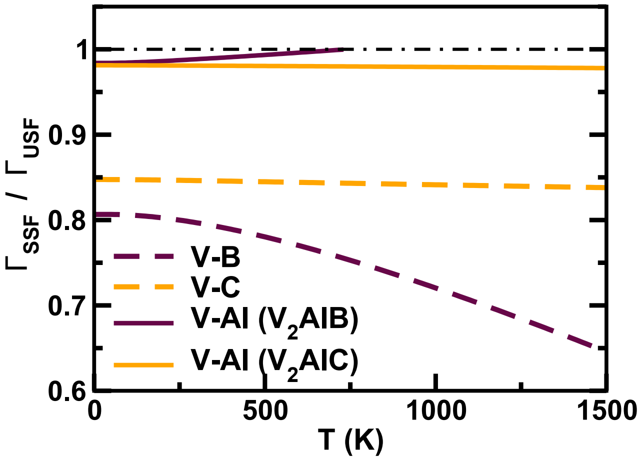

Figure 4.7: Temperature evolution of $\Gamma_{SSF}/\Gamma_{USF}$ for two different cut planes and two different compounds.

indicating an increased tendency of formation of wider stacking faults in boride compound at elevated temperature. $\Gamma_{SSF}/\Gamma_{USF}$ for V-Al plane of VAB, on the other hand, upon increasing temperature, increases from a value slightly below 1 ($\approx$ 0.98) to a value of 1 at a critical temperature of $\approx$ 730 K, at which USF and SSF configurations become degenerate and the fault vanishes.

4.4 Conclusion

Strength and ductility are two important mechanical properties for structural materials. However, it is difficult to have both high strength and high ductility. In addition to that materials with *hcp* structure have limited number of independent slip systems. SFE is commonly accepted as a useful quantity for understanding the plastic deformation in metals. The introduction of alloy elements as well as substitutional doping is considered an effective approach to improve mechanical properties. Therefore, in order to improve the mechanical properties, we studied the effect of boron-substitution in V_2AlC. In particular, we computed the generalized stacking fault energies for VAC and B-substituted compounds. The calculated stacking fault energies at T = 0 K associated with basal slips between the V-Al and V-X (X=B/C) atomic layers, resulted in the reduction of stable stacking fault energy by a factor of about 1.5-2 in the V-X layer for the boron-substituted compounds, compared to the carbide compound. This makes the SSF of the M-A plane comparable to that of the M-X plane in case of VAB, they being very different in case of VAC. This in turn triggers two basal (M-X and M-A) planes to be operative at T = 0 K in case of VAB as opposed to a single basal plane (M-A) in case of VAC. The Peierls stress obtained from the continuum modeling based on inputs of DFT computed γ-surface and the elastic constants, shows significant reduction for M-X layer upon B-substitution. Peierls stress being related to mobility of dislocation and being the lower bound of the yield strength, this indicates that the boride MAX phases will be significantly more ductile compared to conventional carbide MAX compounds.

Extension of our study to finite temperature showed that while the stacking faults are not very temperature sensitive for carbide, they show interesting temperature dependence for the boride counterpart, having contrasting temperature dependence of the M-A and M-X slip planes. Curiously, the stable stacking fault in the V-Al plane of the boron compound becomes more and more unstable as temperature is increased, and finally disappears at $\sim$730K. On the other hand, the SSF for the V-B plane becomes more stable at higher temperature, which implies a well-defined stacking fault to be observed at higher temperatures. The improved mechanical properties of the computer designed boron-based MAX phases, should motivate future synthesis and exploration of these new MAX phases.

Chapter 5

Manipulating the mechanical properties of Ti_2C MXene: Effect of substitutional doping

5.1 Introduction

In the last decade, discovery of two dimensional (2D) solids such as graphene has significantly advanced our understanding of the properties of these materials [171, 172, 173]. 2D materials have unusual electronic, mechanical and optical properties [174, 175, 176, 177, 178], which have led to their extensive study. Recently, a new class of graphene-like 2D materials of transition metal carbides/nitrides have been synthesized by micromechanical exfoliation of their three-dimensional (3D) counterparts [179], the layered ternary transition metal carbides or nitrides, known as MAX phases [180]. As discussed in the previous chapter, the MAX phases have the general formula $M_{n+1}AX_n$, where M is a transition metal, A is an A-group element and X denotes carbon or nitrogen. Weaker relative strength of M-A bonds compared to M-X bonds allows selective etching

---

This chapter is based on "Manipulating the mechanical properties of Ti_2C MXene: Effect of substitutional doping" - *Poulami Chakraborty*, Tilak Das, Dhani Nafday, Lilia Boeri and Tanusri Saha-Dasgupta, Phys. Rev. B **95**, 184106 (2017) of the A layer by chemical means without disrupting the M-X bonds. The nomenclature MXene denotes the loss of A element from the parent $M_{n+1}AX_n$ phase, and also emphasizes the structural similarity with graphene [181, 182]. Today, the MXene family includes compounds such as Ti_3C_2, Ti_2C, Nb_2C, V_2C, Ti_3CN and Ta_4C_3 [183]. A single MXene sheet may consist of 3, 5, or 7 atomic layers, which depends on the value of n that can vary from 1 to 3. In all cases, the individual MXene layer thickness is less than 1nm, while their lateral dimensions can reach tens of microns. MXenes have been discussed as potential candidates for Li-ion battery anodes and hydrogen storage medium [66, 184]. However, there have been fewer studies on the mechanical properties of MXene and possible application of MXenes that utilizes the flexibility of these 2D materials [185, 186]. The concept of flexibility of a material is related to its mechanical properties with emphasis on deformability under large strains. The few computational studies that have been carried out in this context, showed that Ti_2C to be less stiff compared to graphene or *h*-BN, but stiffer to MoS_2 [187]. To investigate the possibility of application of MXenes in flexible devices, it is essential to develope our understanding further in the domain of the mechanical properties of this 2D nanomaterial under deformation, *i.e.* complete stress-strain relations, from which the critical strain and the strength of the material could be obtained. One should also explore means to make these materials further flexible to meet the application requirement.

MXenes that are synthesized using acidic-fluoride-containing solutions have a mixture of -OH, -O and -F terminations with the chemical formula $M_{n+1}X_nT_x$, where T represents the surface terminations. Non-terminated MXenes are yet to be synthesized. Recent calculations have considered study of surface terminations in addition to properties of bare $M_{n+1}X_n$ layers [61, 62, 188]. These calculations showed that surface passivation by O termination improves the mechanical properties in terms of in terms of increase in the critical strain value [187]. We thus considered both unpassivated Ti_2C as well as oxygen passivated Ti_2C.

In this work, we considered substitutional doping of B at C and V at Ti sites of Ti_2C. We studied the manipulation of the mechanical properties through substitutional doping. We carried out calculations of in-plane stiffness, Young's modulus, Poisson's ratios, and critical strains.

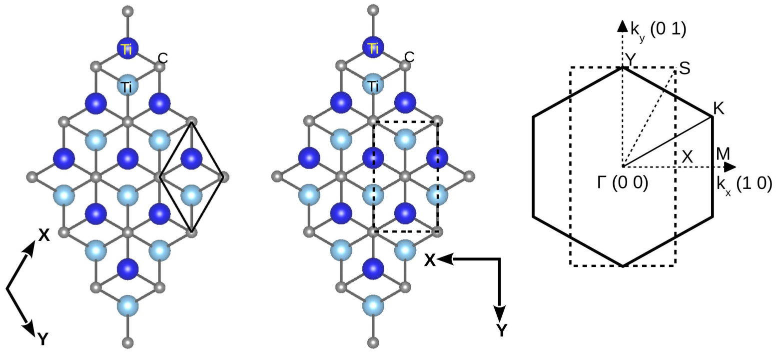

Figure 5.1: Left panel: One formula unit, hexagonal primitive cell with three atoms, marked with solid lines in the lattice. The large and small sized balls denote Ti and C atoms, respectively. The Ti atoms belonging to top and bottom layers are colored differently. Middle panel: Two formula units, orthorhombic cell with six atoms, marked with dashed lines in the lattice. Right panel: The primitive cell of the reciprocal lattice corresponding to the hexagonal cell (marked with solid lines) and the orthorhombic cell (marked with dashed lines).

5.2 Methodology

All DFT calculations on pure and B or V doped Ti_2C or Ti_2CO_2 have been performed using projector augmented wave (PAW) potentials and the plane-wave based Vienna Ab initio Simulation Package (VASP) [164]. The exchange-correlation functional was chosen to be that of the generalized gradient approximation (GGA) as implemented in the Perdew-Burke- Ernzerhof (PBE-GGA) formalism [93]. The calculations have been also verified using the local density approximation (LDA). For Ti and V we have used [Ar]3p3d4s configurations as valence configurations while for C, B, and O [He]2s2p configurations were used as valence. The monolayer of Ti_2C was obtained from the bulk structure of the MAX phase Ti_2AlC by removing the A layer and adding a vacuum of 20 Å along the z direction. The generated quasi-2D monolayer of MXene-structured Ti_2C consists of a hexagonal layer of C atoms sandwiched between top and bottom monoatomic hexagonal Ti planes. The primitive hexagonal cell of Ti_2C is shown in the left panel of Fig. 5.1. 50% of the C (Ti) atoms were replaced by B (V) in order to generate the B-doped (V-doped) Ti_2C compounds. For 50% doping by V and C, a two-formula-unit orthorhombic supercell was considered (shown in the middle panel of Fig. 5.1), with one out of two Ti atoms belonging to the top layer in the cell being replaced by V, and out of two Ti atoms belonging to the bottom layer in the cell being replaced by V for (Ti,V)C. Similarly for $Ti_2(C_{0.5},B_{0.5})$ one out of two C atoms belonging to the middle layer in the cell is replaced by B. The right panel of Fig. 5.1 shows the Brillouin zone (BZ) of the hexagonal primitive as well as orthorhombic supercell. The two-formula-unit orthorhombic cells of doped Ti_2C are shown in Fig. 5.2 where Fig. 5.2(a) represents the B doped case and Fig. 5.2(b) represents the V doped case. Note that the orthorhombic cell has the X direction as the zigzag or nearest-neighbour metal-C(B) bond direction and the Y direction as the armchair or second-nearest-neighbour metal-C(B) bond direction. For our stress-strain calculations, for undoped as well as doped compounds we have considered the two-formula-unit orthorhombic supercell, which allows one to apply the uniaxial strains along the zigzag and armchair direction. The structures were fully relaxed to obtain the in-plane lattice parameters and the atomic positions until the Hellmann-Feynman forces became less than 0.001 eV/ Å. The structural relaxations were carried out within the non- spin-polarized PAW PBE-GGA+D3 formulation taking into account van der Waals corrections [189]. Subsequent self- consistent electronic structure calculations were carried out on the optimized structures within the spin-polarized GGA approach. In order to check the influence of the missing correlation effect beyond GGA, calculations have been also carried out with supplemented Hubbard U calculations within the GGA+U [190] method with the choice of U = 4 eV and J_H = 0.8 eV at Ti (V) sites.

A 12 x 24 x 1 Monkhorst-Pack k-point mesh [191] in the orthorhombic BZ and with an 800 eV plane-wave cutoff was found to provide good convergence of the total energy. The convergence of the energies was ensured using the self-consistency criteria of 10^{-8} eV. In order to cross-check the magnetic ground states in terms of total energy calculations of different chosen magnetic configurations, calculations have been repeated in terms of the all-electron method of the linearized augmented plane wave (LAPW) with no shape approximation to the potential and charge density, as implemented in the Wien2k code [192]. For LAPW calculations, we chose the APW+lo as the basis set and the expansion in spherical

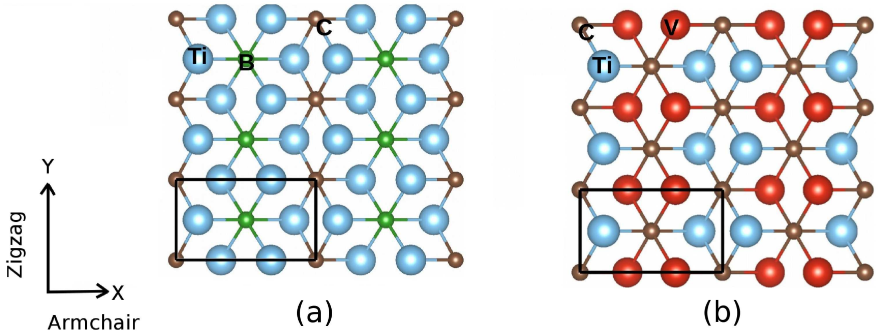

Figure 5.2: The inplane view of the optimized geometries of (a) B-doped Ti_2C and (b) V-doped Ti_2C are shown. The large balls denote Ti (cyan) and V (red), while the small balls denote C (brown) and B (green). The orthorhombic unit cell in each cases have been marked with solid, black line.

harmonics for the radial wave functions was taken up to $l_{max} = 10$. The charge densities and potentials were represented by spherical harmonics up to $l_{max} = 6$. For the number of plane waves, the criterion used was the smallest muffin-tin radius (RMT) multiplied by K max (for the plane wave) yielding a value of 8.0. The RMTs of Ti, V, C, B were chosen to be to 1.15, 1.11, 0.90, 0.95 Å, respectively. The mechanical properties of 2D MXenes under discussion were studied using the stress-strain relation of the materials upon application of biaxial and uniaxial tensions along zigzag and armchair directions. The strain was applied by increasing both the in-plane lattice parameters for the biaxial case and the lattice parameters along the X or Y axis for uniaxial cases. The structural coordinations were allowed to relax within the PAW PBE-GGA scheme of calculations until the component of the stress tensor along the orthogonal direction due to Hellmann-Feynman forces was below 0.1 GPa. To avoid the influence of the vacuum present in the periodic setup of our calculation, the stress value was scaled by the factor h/d_0 , where h is the cell height along the Z axis and d_0 is the thickness of the material.

Phonon calculations have been carried out within the formulation of density functional perturbation theory (DFPT) [193] as implemented in the Quantum Espresso (QE) code [194]. For this purpose, the ground state geometries obtained from VASP were reoptimized within QE using ultrasoft pseudopotentials of Garrity, Bennett, Rabe, and Vanderbilt [195]. The exchange-correlation functional was chosen to be PBE-GGA, as in VASP calculations. The energy cutoffs for the wave function and charge density were set to about 680 eV and 6802 eV, respectively, and the energies were converged to 10^{-10} eV. The ground state geometries and the electronic structure obtained within QE were found to be in good agreement with those obtained with VASP. For phonon calculations, the dynamical matrices were computed on a 4 x 8 x 1 k mesh of the BZ of the orthorhombic cell (cf. Fig. 5.1), and the phonon band structures, obtained by Fourier interpolation of the real-space force constants, were plotted along the high-symmetry k points of the BZ. In order to have an idea of phonon softening, the frequencies of the phonon modes at the Γ point were computed for 50% B and V doped structures as well as for the pure Ti_2C.

5.3 Results and Discussion

In order to study the doping effect on mechanical properties of 2D Ti_2C, we first focus on the electronic and magnetic structures of pristine Ti_2C as well as that of $Ti_2(C_{0.5},B_{0.5})$ and (Ti,V)C. After having an understanding of the underlying electronic and magnetic structures, we present results for elastic properties such as in-plane stiffness, Youngs modulus, and Poissons ratio, followed by the estimate of critical strains. Since the MXene structures synthesized to date [60] are terminated by either O, OH, and/or F, in the final part we consider the doping effect on properties of O-terminated 2D Ti_2C.

5.3.1 Electronic and magnetic structures of pristine and doped Ti_2C

The DFT computed non-spin-polarized density of states of Ti_2C shows highly peaked structures at Fermi energy (E_F), with density of states at E_F estimated to be about 4.6 states/eV [68]. Within the Stoner criterion and with a Stoner parameter (I) of Ti as 0.615 [196], this indicates the instability towards ferromagnetism. Indeed the magnetic solution with a parallel alignment of all Ti spins turns out to be lower in energy compared to the nonmagnetic solution by about

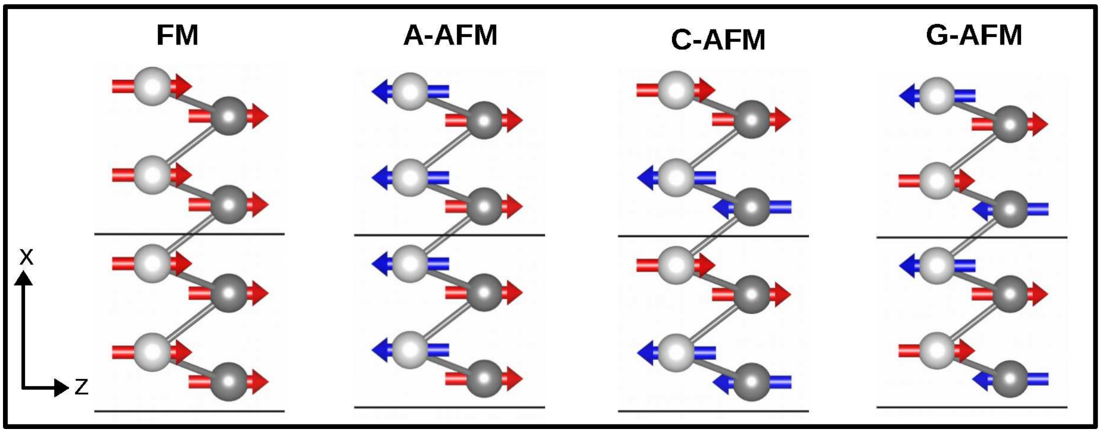

Figure 5.3: The possible magnetic configurations are shown for pure Ti_2C. Ti atoms in the different planes are marked by two different shades. C atoms are not shown.

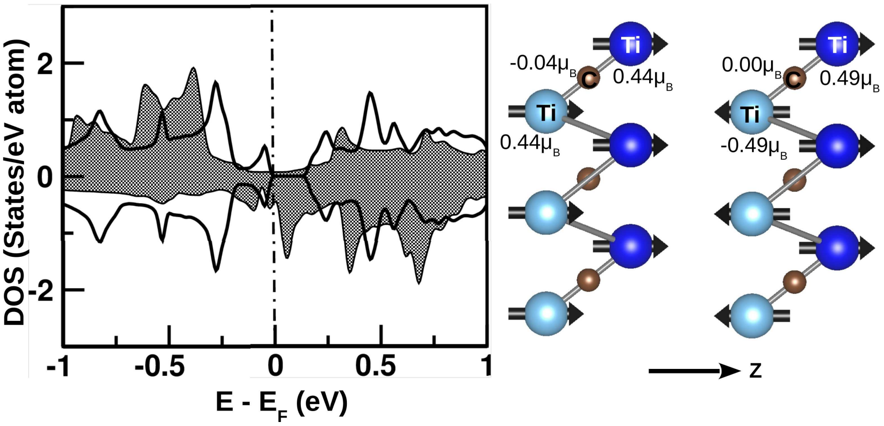

Figure 5.4: Left panel: Comparison of calculated density of states corresponding to FM (shaded area) and A-AFM (solid lines) magnetic states plotted as a function of energy. The energy value is measured with respect to GGA Fermi energy, E_F. The alignment and magnitudes of Ti and C moments in FM and A-AFM magnetic configurations are shown in middle and right panels, respectively.

100 meV/f.u. with a magnetic moment of $\approx 0.5\ \mu_B$ at each Ti atom. While the magnetism of unpassivated Ti_2C has been reported in the literature [197], to the best of our knowledge, the underlying magnetic structure has not yet been clarified. In the Ti_2C structure each Ti atom is covalently bonded with three nearest C atoms, while each C atom is bonded with six nearest Ti atoms, three of which belong to the top layer and three belong to the bottom layer. Thus in addition to the ferromagnetic (FM) structure with a parallel alignment of all Ti spins, three different antiferromagnetic (AFM) structures are possible which are illustrated in Fig. 5.3 (i) A-AFM: ferro ordering between intralayer Ti's and antiferro ordering among interlayer Ti's, (ii) C-AFM: antiferro ordering between intralayer Ti's and ferro ordering among interlayer Ti's, and (iii) G-AFM: antiferro ordering between intralayer Ti's and between interlayer Ti's. Total energy calculations for FM, A-AFM, C-AFM, and G-AFM show the A-AFM structure to be lowest in energy, followed by FM structure, while C-AFM and G-AFM structures are found to be lying significantly higher in energy, by more than 100 meV/f.u. The energy difference between the A-AFM and FM structures turned out to be 32 meV/f.u. This suggests the intralyer Ti-Ti coupling to be strongly ferromagnetic, while the interlayer Ti-Ti magnetic interaction to be weaker compared to intralayer coupling and of antiferromagnetic nature.

Fig 5.4 shows the calculated total density of states of Ti_2C (TC) in the FM and lowest energy A-AFM magnetic structure. We find that the nearly half-metallic nature of Ti_2C in the FM structure gets destabilized in the A-AFM structure, which becomes semiconducting with an estimated band gap of ≈ 0.2 eV. To the best of our knowledge, the semiconducting nature of bare Ti_2C has not been reported in the literature so far. The inclusion of the correlation effect beyond GGA, through the Hubbard U corrected mean-field theory of GGA+U , is found to keep the qualitative trend unchanged with the A-AFM structure as the lowest energy, though the magnetic moment of individual Ti atoms is found to be enhanced to $\approx 0.7\ \mu_B$. The calculated magnetic moments in GGA and GGA+U have been listed in Table 5.1 for the ground state A-AFM structure. The magnetic moments for other magnetic configurations turn out to be rather similar. Since the qualitative trend is found to remain unchanged between GGA and GGA+U calculations, in the following we present results obtained within the GGA scheme of calculation.

Table 5.1: Magnetic moments (in μ_B) at metal (Ti/V) sites in A-AFM phase, calculated within GGA and GGA+U. The moments on C or B are found to be negligibly small.

	GGA			GGA + U		
	TC	TVC	TBC	TC	TVC	TBC
Ti	0.54	0.39	0.48	0.71	0.34	0.74
V		0.47			1.85	

We next consider the effect of substitutional doping at the C site by B, and that at the Ti site by V, by considering $Ti_2(C_{0.5},B_{0.5})$ (TBC) and (Ti,V)C (TVC) compounds. We checked the tendency towards segregation versus homogeneous mixing by comparing the energies of the B-rich and C-rich configurations (Ti-rich and V-rich configurations) to that of a uniform mixing of B and C (Ti and V) with alternating arrangement of B and C (Ti and V). The later is found to be energetically stable by about 30-40 meV/f.u. compared to the segregated structure. Introducing B in the structure causes local deformation, with compression in the out-of-plane direction and an in-plane expansion. The reverse is found to be true for substitution of Ti by V. Even for the doped compounds the A-AFM magnetic structure is found to be the lowest energy magnetic configuration followed by FM structure while the energies for G-AFM and C-AFM magnetic structures turn out much higher, following the same trend as the undoped Ti_2C. The energy difference between A-AFM and FM structure turned out to be $\approx$ 10 meV/f.u. for $Ti_2(C_{0.5},B_{0.5})$, and $\approx$ 100 meV/f.u. for (Ti,V)C. Thus while the B doping somewhat weakens the interlayer magnetic coupling, V doping enhances it substantially.

Fig 5.5 shows the plot of the density of states (DOS) for Ti_2C, $Ti_2(C_{0.5},B_{0.5})$, and (Ti,V)C compounds for the lowest energy A-AFM magnetic structure. Note B substitution at the C site causes hole doping, while V substitution at the Ti site causes electron doping in the system. This together with local deformation makes the system metallic as seen from the plot in the left, topmost panel in Fig.

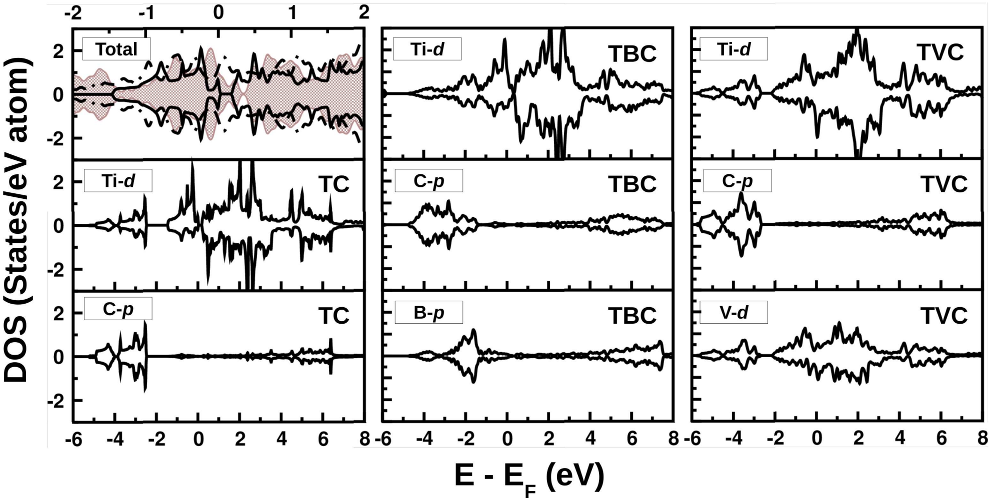

Figure 5.5: Total and partial DOS projected to Ti-d, V-d, C-p, and B-p states in Ti_2C (TC), $Ti_2(C_{0.5},B_{0.5})$ (TBC), and (Ti,V)C (TVC) plotted as a function of energy. The comparison of the total DOS of TC (solid lines), TBC (shaded area), and TVC (dashed lines) is shown in the topmost, left column panel, while the plots in other panels show the partial DOS projected either to Ti-d or V-d or C-p or B-p states.

5.5. As is evident from the plots of partial density of states, presented in the remaining panels of Fig. 5.5, for Ti_2C, the Ti-d-C-p hybridized bonding states appear in the energy range about -5.0 eV to about -2.5 eV, separated by a gap of $\approx$ 1.0 eV from the nonbonding Ti-d dominated states spanning an energy range of $\approx$ -1.5 eV to $\approx$ +4 eV, and arising out of metal-metal bonding. The higher lying states from $\approx$ 4 eV to 6 eV are contributed by Ti-d-C-p hybridized antibonding states. The Ti-d-B-p hybridized bonding states for $Ti_2(C_{0.5}B_{0.5})$ appear in the energy range $\approx$ -3 eV to $\approx$ -0.5 eV, shifted with respect to Ti-d-C-p hybridized bonding states, signalling the difference in the strength of hybridization between C-p and B-p with Ti-d. This in turn closes the energy gap between nonbonding and bonding states in the case of $Ti_2(C_{0.5}B_{0.5})$ which was observed for Ti_2C. In the case of (Ti,V)C, the gap between the nonbonding and bonding states persist with nonbonding V-d dominated states spanning almost the same energy range as that of Ti-d dominated nonbonding states.

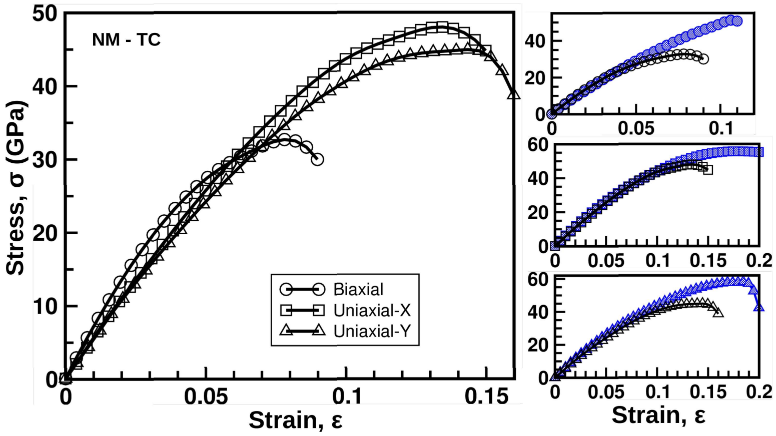

Figure 5.6: The stress-strain curve of the pristine Ti_2C under biaxial and uniaxial tensile strains along the zigzag (uniaxial-X) and armchair (uniaxial-Y) directions. The left panel shows the results for NM state of Ti_2C. The top, middle, and bottom right panels show the comparison for NM (open symbols) and A-AFM (shaded symbols) states under biaxial, uniaxial-X, and uniaxial-Y loading of strain.

5.3.2 Mechanical properties of pristine and doped Ti_2C

We have studied the mechanical response of the pristine and doped Ti_2C under three different loading conditions of the tensile strain: biaxial tension and uniaxial tensions along the X and Y directions of the orthorhombic cell. We applied a series of incremental tensile strains in the cell, and, as mentioned already, simultaneously relaxed the other stress components to zero which takes into account Poisson contraction under uniaxial tension. In the following we first discuss the elastic properties, and then the critical strains.

Stress-strain relations: Elastic properties

The calculated stress-strain curves for pristine Ti_2C are shown in Fig. 5.6. The left panel of the figure shows the result for nonmagnetic (NM) Ti_2C, while the right panels show the comparison of the stress-strain curves between the nonmagnetic Ti_2C and Ti_2C in the lowest energy magnetic state of A-AFM. The elastic constants can be extracted by linear fit to the stress-strain curves for small strain values. We note that unlike graphene or h-BN, Ti_2C is a two-dimensional multiplanar hexagonal structure, and therefore quasi-2D. As discussed in Ref. [83] from a structural point of view the general 2D materials can be classified into four different classes. According to that general classification, the MXene family of compounds such as Ti_2C belongs to class D, where the constituent atoms are not the same and they belong to different planes. Even though these structures have a hexagonal top view, different atoms are found to be placed in different planes. The high-fidelity analytical model developed in Ref. [83] starting from equivalent elastic properties of atomic bonds shows that the elastic properties of quasi-2D materials belonging to class D needs to be described by two Young's moduli (E_1 and E_2) and two Poisson's ratios (ν_{12} and ν_{21}), 1 and 2 directions referring to zigzag and armchair directions respectively. Graphene or h-BN belonging to class A or class B, on the other hand, can be described by a single Young's modulus and a single Poisson's ratio with $E_1 = E_2$, and $\nu_{12} = \nu_{21}$. Our DFT calculations show that for our studied systems E_1 and E_2 differ by 3%-4% with $E_1 > E_2$, in agreement with findings of a previous DFT study [187]. This suggests that the Ti_2C family of compounds is nearly isotropic, as opposed dichalcogenides such as MoS_2 [83]. For the ease of comparison between different 2D materials we have quoted $E = (E_1 + E_2/2)$. Similarly, our calculations show that for our studied systems ν_{12} and ν_{21} differ by 3%-5%. As in the case of Young's modulus, we have quoted $\nu = (\nu_{12} + \nu_{21})/2$.

In the case of 2D materials, because of the reduced dimensionality of these materials, it makes more sense to define the in-plane stiffness, C, which is nothing but E^{2D} instead of the classical 3D Young's modulus, as extensively used in literature for different 2D materials [187, 200]. This can be obtained by fitting the initial slope of the stress-strain curve under the condition of biaxial strain. The calculated in-plane stiffness, Young's modulus (E), and Poisson's ratio (ν) are listed in Table 5.2. Comparing the stress-strain curves between the NM state and A-AFM state, as presented in the right column of the figure, we find that while the effect of magnetism is relatively small in the linear regime or the harmonic region of the strain, it has significant influence in the nonlinear or the anharmonic region. The damage of the A-AFM phase occurs at higher strain than that of

Table 5.2: Elastic constants of pure Ti_2C, B doped and V doped compounds under biaxial, uniaxial-X and uniaxial-Y strain. For comparison, the previously calculated elastic constants of pure Ti_2C [187], MoS_2 [198], graphene [198], *h*-BN [199] and SiC [199] are also listed. The in-plane stiffness constant (C), Young moduli (E) are in GPa, while the biaxial and uniaxial critical strain values are given in %. To compare with elastic constant values of other 2D materials, as given in Refs.[198, 199], our calculated in-plane stiffness constants are also quoted in N/m in parentheses.

				Critical Strain			
		C	E	ε_{c1}^{bi}	ε_{c1}^{1}	ε_{c1}^{2}	ν
TC	NM	704 (142)	577	8	13	14	0.366
	AFM	715 (152)	586	11	18	18	0.292
TVC	NM	738 (152)	590	6	14	15	0.399
	AFM	742 (157)	596	4	11	11	0.360
TBC	NM	515 (120)	426	5	11	11	0.365
	AFM	521 (124)	432	10	16	14	0.301
Pure Ti_2C	Ref.[187]		610	9.5	18	17	
MoS_2	Ref.[198]	120.1					0.254
Graphene	Ref.[198]	340.8					0.178
h-BN	Ref.[199]	275.8					0.220
SiC	Ref.[199]	163.5					0.300

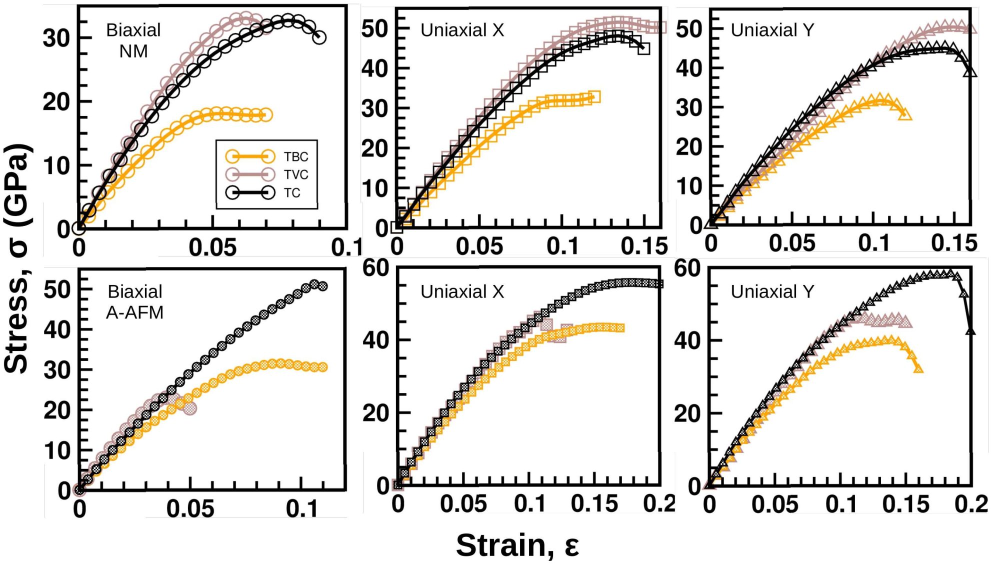

Figure 5.7: The stress-strain curve of Ti_2C, $Ti_2(C_{0.5},B_{0.5})$ and (Ti,V)C under biaxial and uniaxial tensile strains along the X and Y directions. The top panels show the results for NM states, while the bottom panels show the results for the minimum energy A-AFM magnetic state.

the NM phase. This indicates the presence of rather strong magnetostructural coupling, which we will come back to in the following.

Comparison of stress-strain curves between pristine and B/V-doped Ti_2C is presented in Fig. 5.7. Focusing on the linear regime a significant difference is found between the elastic properties of Ti_2C and $Ti_2(C_{0.5},B_{0.5})$. Extracted values of in- plane stiffness, Young's modulus, and for Poisson's ratio for $Ti_2(C_{0.5},B_{0.5})$ and (Ti,V)C are listed in Table 5.2 for the NM state as well as for the A-AFM state. There is about 25%-27% decrease in in-plane stiffness as well as in Young's modulus of $Ti_2(C_{0.5},B_{0.5})$ compared to that of the Ti_2C. Substitutional doping of V at the Ti site, on the other hand, is found to keep the stiffness similar to the undoped Ti_2C. The computed elastic properties of other 2D materials, as reported in literature, are also listed in Table 5.2. On comparison, we find that undoped Ti_2C is much less stiff compared to graphene or h-BN, though somewhat stiffer compared to MoS_2, as discussed before. B doping helps in reducing the in-plane stiffness, bringing it down to the level of MoS_2 .

The appreciable reduction in elastic properties under substitutional B doping

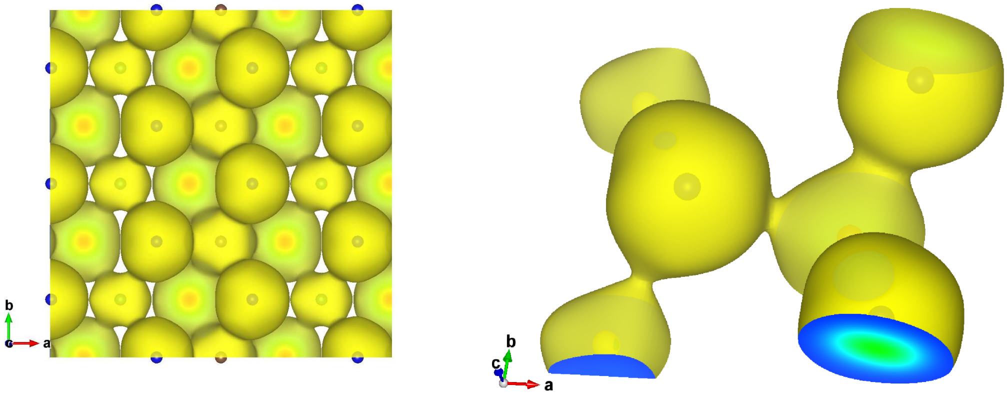

Figure 5.8: The plot of calculated charge density for $Ti_2(C_{0.5},B_{0.5})$. The isosurface value is chosen at 0.065 $e^-/Å^3$. Left panel shows the plot in an extended region, while the right panel presents zoomed view focused on central Ti atom bonded with B and C. The stronger covalency of the Ti-C bond compared to the Ti-B bond is visible.

can be rationalized by the weakening of the Ti-B bond as compared to the Ti-C bond. Fig 5.8 shows the plot of the charge density which highlights the relatively stronger covalency between Ti and C compared to that between Ti and B. This is further corroborated by the calculated phonon frequencies at the Γ point (cf. Fig. 5.9(a)). Upon B doping, the low-frequency phonon modes are found to shift to the lower frequencies to a large extent, while only marginal shifts are observed for V doping. The modes associated with such low-frequency modes, as shown in the insets, correspond to atomic displacements related to movement of Ti-C, Ti-B, or V-C bonds. Since the phonon frequency (ω) is related to the bond stiffness (κ) as $\omega \propto \sqrt{\kappa}$, the softening of these modes confirms the weakening of Ti-B bonds compared to Ti-C bonds, as concluded from charge-density plots.

Critical strains

As mentioned above, the stress-strain curve is characterized by a linear or harmonic region at small strain values, followed by an anharmonic region where higher-order terms in strain energy start to become important. The nonlinear mechanical property is anisotropic [201, 202], thereby giving rise to different critical

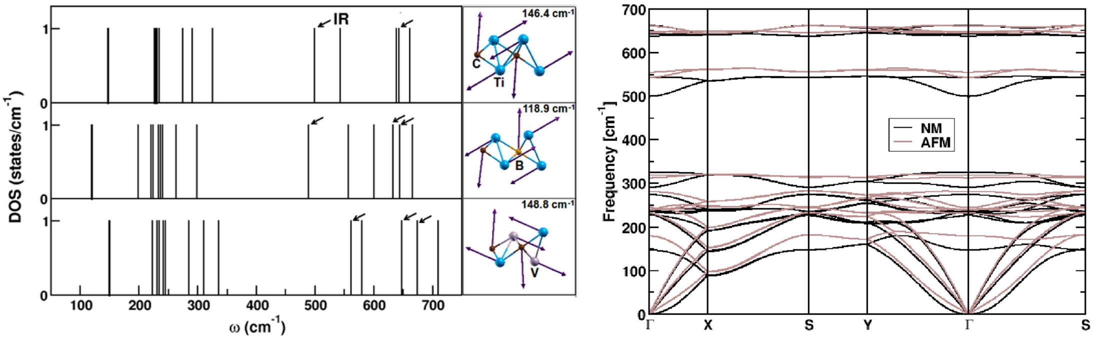

(a) (b)

Figure 5.9: (a) Calculated optical phonon (Γ point) frequencies for Ti_2C (top panel), $Ti_2(C_{0.5},B_{0.5})$ (middle panel) and (Ti,V)C (bottom panel). The arrows highlight the infrared (IR) active modes. The insets in right columns show the atomic displacements corresponding to lowest frequency modes in each cases. (b) Phonon dispersion of Ti_2C in the NM and ground state magnetic structure of A-AFM.

strain values in biaxial and different uniaxial tensions, applied along the zigzag and armchair directions of the orthorhombic supercell. Following the stress-strain plots, the critical strain value, ε_{c1} , is characterized by the strain value at which the stress attains its maximum value after which the stress starts to fall and instability sets in. This provides a measure of the highest withstanding of the strain. Table 5.2 lists the values of ϵ_{c1} for Ti_2C, $Ti_2(C_{0.5},B_{0.5})$, and (Ti,V)C under biaxial and uniaxial strains in the X and Y directions, referred to as ${\varepsilon^{bi}}_{c1}$, ${\varepsilon^{1}}_{c1}$ and ${\varepsilon^{2}}_{c1}$ respectively. As is seen, magnetism has a strong influence in the values of ϵ_{c1} , increasing it from 8%, 13%, and 14% to 11%, 18%, and 18% for Ti_2C under biaxial, uniaxial-X, and uniaxial-Y tensile strains. A similar trend is generally observed for $Ti_2(C_{0.5},B_{0.5})$, though a slight decrease has been observed for (Ti,V)C under biaxial strain.

Fig 5.9(b) shows the phonon dispersion plotted along the high-symmetry points of the orthorhombic BZ for Ti_2C in NM and A-AFM ordered phase. As is evident from the plot, inclusion of magnetism changes the phonon frequencies significantly hinting towards the presence of strong spin-phonon coupling. We find, in general, dispersions to be stiffer for AFM Ti_2C compared to NM Ti_2C,

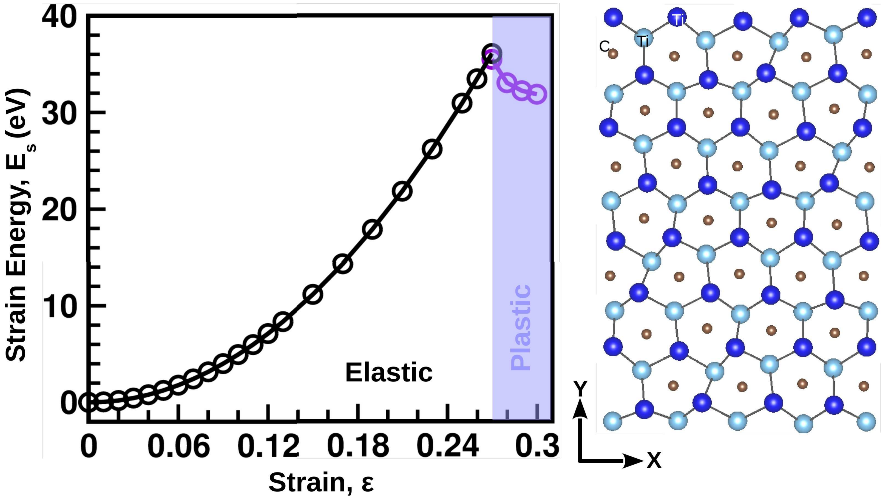

Figure 5.10: Left panel: The variation of strain energy as a function of the biaxial strain for Ti_2C. The strain value at which the drop in the strain energy occurs denotes the second critical point, ϵ_{c2} . Right panel: The structure of Ti_2C at the strain value of ϵ_{c2} .

especially at the vicinity of the point. Given the fact that the slopes of the dispersion curves close to can be expressed as the square root of the elastic constant (or combinations) over density, this amounts to increased stiffness of the Ti_2C in the AFM phase compared to NM. This is supported by the calculated elastic constants (cf. Table 5.2).

The three lowest energy branches designate three acoustic (A) branches corresponding to long-wavelength vibrations, classified as LA, TA, and ZA (cf. Fig. 5.9(b)), where L stands for longitudinal polarization, T for in-plane transverse polarization, and Z for out-of-plane transverse polarization. For NM Ti_2C, the ZA branch close to Γ shows the quadratic dispersion, which is a characteristic feature of other 2D materials as well, such as graphene [203]. This very soft mode, which propagates parallel to the layer, corresponds to the *layer-bending* or *ripple mode* [204]. In AFM Ti_2C the dispersion corresponding to ZA modes changes considerably compared to NM Ti_2C suggestive of hardening of such layer-bending or ripple mode. This justifies the observation that AFM Ti_2C can withstand significantly higher strain as compared to NM Ti_2C (cf. Fig. 5.6 and discussions therein).

The anharmonic region is followed by a plastic region where irreversible structural changes occur in the system and it transforms into a different structure after the yielding point. The second critical point, ϵ_{c2} , is the yielding point and marks the boundary between elastic and plastic regions. Up to ϵ_{c2} , the system preserves the hexagonal symmetry and upon release of strain the system reverts back to the unstrained structure. We have estimated ϵ_{c2} for the biaxial strain. For this purpose, we plotted the strain energy (E_s) as a function of biaxial strain (ϵ). The strain energy is calculated by subtracting the total energy of the strained system from the equilibrium total energy, and related to stress, as $\sigma = \frac{dE_s}{d\epsilon}$. The E_s versus ϵ plot for NM Ti_2C is shown in the left panel of Fig. 5.10. ϵ_{c2} is given by the strain value at which the strain energy drops, which in the present case is estimated to be 27%. The structure at this strain value is shown in the right panel of Fig. 5.10, which demonstrates the deviation of the structure from the hexagonal symmetry at the yield point. We note that the presence of defects and the temperature effect can reduce our estimated ϵ_{c2} value significantly. Repeating the same exercise for B-doped Ti_2C, the value of ϵ_{c2} was estimated to be $\approx$ 33% indicating effectiveness of B doping in also enhancing the yield strength. V doping, on the other hand, is found to reduce the ϵ_{c2} value slightly with an estimated value of 26%. Introduction of magnetism does not appear to have significant influence on ϵ_{c2} values.

Effect of O termination on mechanical properties

Finally we consider the effect of termination by O. Three possible configurations of termination exist [197] (i) configuration I: O's are located above the hollow site of three neighbouring C/B atoms and point to the Ti/V atoms in the second Ti/V layer on both sides of MXene, (ii) configuration II: O's are located above the C/B atoms for both sides of MXene, (iii) configuration III: configuration I on one side and configuration II on the opposite side. Our total energy calculations show configuration I to be the minimum energy configuration among the three in conformity with previous findings [197]. In the following, we thus considered only configuration I as far as termination is concerned. The created local strain due to substitutional doping of B at the C site and V at the Ti site makes the

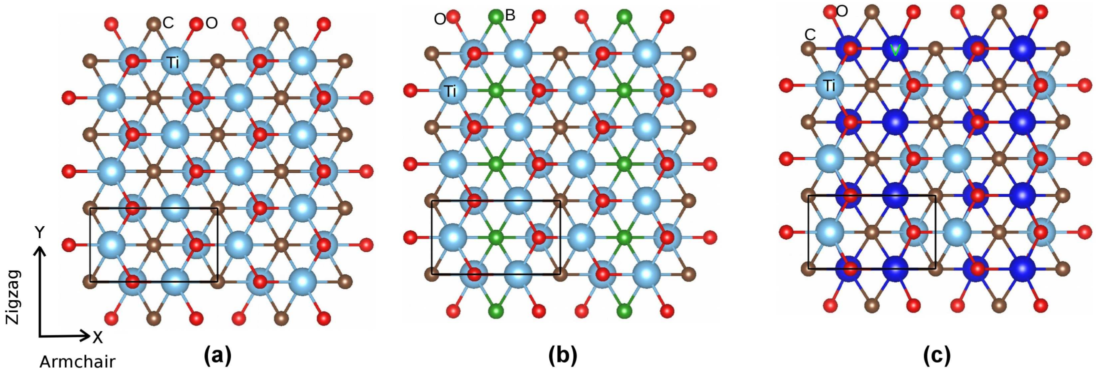

Figure 5.11: The inplane view of the optimized geometries of (a) pure Ti_2CO_2, (b) B-doped Ti_2CO_2 and (c) V-doped Ti_2CO_2 are shown. The large balls denote Ti (cyan) and V (blue), while the small balls denote C (brown), O (red) and B (green). The orthorhombic unit cell in each cases have been marked with solid, black line.

Table 5.3: Elastic properties for pure Ti_2CO_2 (TCO), B-doped Ti_2CO_2 (TBCO) and V-doped Ti_2CO_2 (TVCO) cases. The in-plane stiffness constant (C), Young moduli (E) are in GPa, the critical strain value (ϵ_{c1}) is given in %. The DFT calculated elastic constants for TCO as given in Ref.[187] is also listed.

			Critical Strain			
	C	E	ε_{c1}^{bi}	ε_{c1}^{1}	ε_{c1}^{2}	ν
TCO	745	570	23	28	26	0.303
TCO [187]		567	20	28	26.5	
TVCO	794	560	22	9	28	0.340
TBCO	587	431	16	15	25	0.360

average thickness of the O-passivated MXene larger by about 2% in the doped cases compared to the undoped Ti_2CO_2. The optimized structures of the pure and doped cases are shown in Fig. 5.11. In the doped cases, deformations are observed in the structure. As compared to the pristine case, expansion in the out-of-plane direction is observed for both cases.

We find that O termination leads to complete quenching of magnetism in Ti_2C, as reported already [205], as well as in $Ti_2(C_{0.5},B_{0.5})$ and (Ti,V)C. Fig 5.12 shows the calculated density of states for Ti_2CO_2, $Ti_2(C_{0.5},B_{0.5})O_2$, and $(Ti,V)CO_2$. We find that O-passivated Ti_2C is semiconducting, as reported earlier [197]. Hole (electron) doping by B (V) makes the system metallic. The states lying low far from E_F are primarily Ti-d-(V-d-)O-p, Ti-d-B-p, or Ti-d-(V-d-)C-p bonding states, while the dominant states close to E_F are Ti-d (V-d) non- bonding states. The high lying states away from E_F are the antibonding states arising out of Ti-d-(V-d-)O-p, Ti-d-B-p, or Ti-d-(V-d-)C-p hybridization.

The stress-strain curves for Ti_2CO_2, $Ti_2(C_{0.5},B_{0.5})O_2$, and $(Ti,V)CO_2$ under biaxial, uniaxial-X, and uniaxial-Y tensile strains are plotted in Fig. 15.13. We find the change in slope of the linear regime in the B-doped compounds compared to that of the undoped or V-doped compounds, similar to that observed for the unpassivated compounds. Table 5.3 lists the computed in-plane stiffness, Young's modulus, critical strain, ϵ_{c1} , for undoped and doped compounds. Henceforth, we make the following observations. Firstly, we noted a general increase in the ϵ_{c1} value in the O-passivated compounds compared to unpassivated compounds. For undoped Ti_2C, this increase is 45% to 100% in agreement with previous literature [187]. For B and V doped compounds, this trend is maintained except for uniaxial X for which a decrease is observed. For B-doped Ti_2C the increase in ϵ_{c1} for biaxial and uniaxial Y for O-terminated compound is about 60% - 80% compared to unpassivated compounds, while for V-doped Ti_2C this increase is very large, being 1.5 to 4.5 times. The second important observation is that the trend of suppression of stiffness as well as that of Young's modulus in B-doped compounds compared to the undoped compound continues to be the case even for passivated compounds. The suppression of in-plane stiffness and Youngs modulus is found to be 21% - 26%, rather similar to that found for the unpassivated compounds.

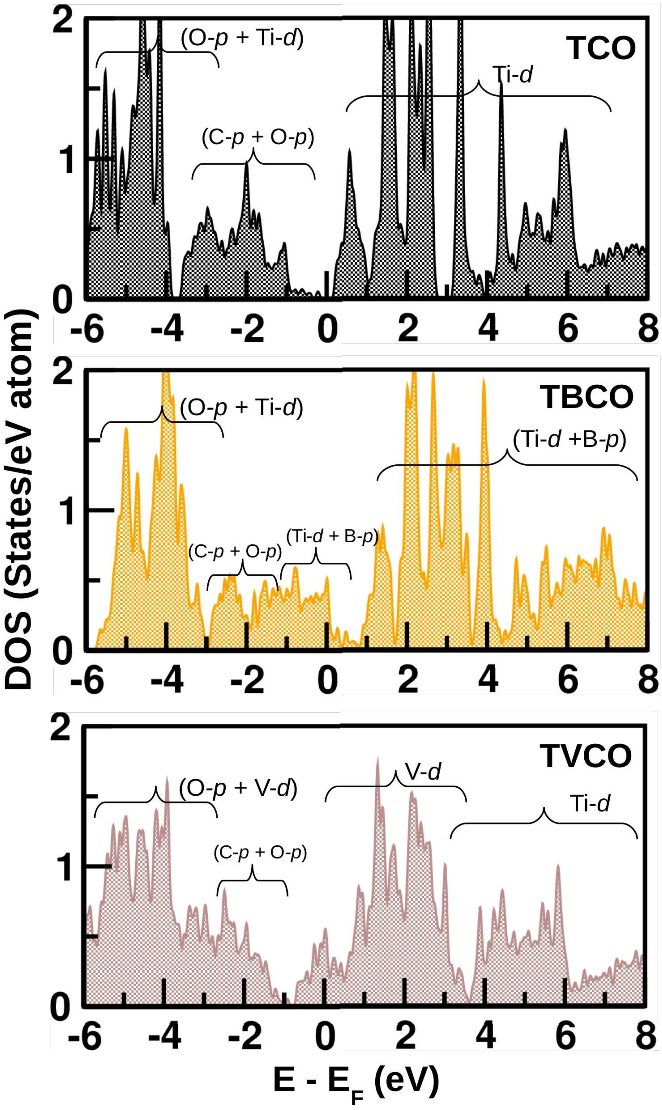

Figure 5.12: The density of states for O-passivated Ti_2C (TCO) (top panel), B-doped Ti_2CO_2 (TBCO) (middle panel), and V-doped Ti_2CO_2 (TVCO) (bottom panel) plotted as a function of energy. The dominant orbital characters have been marked.

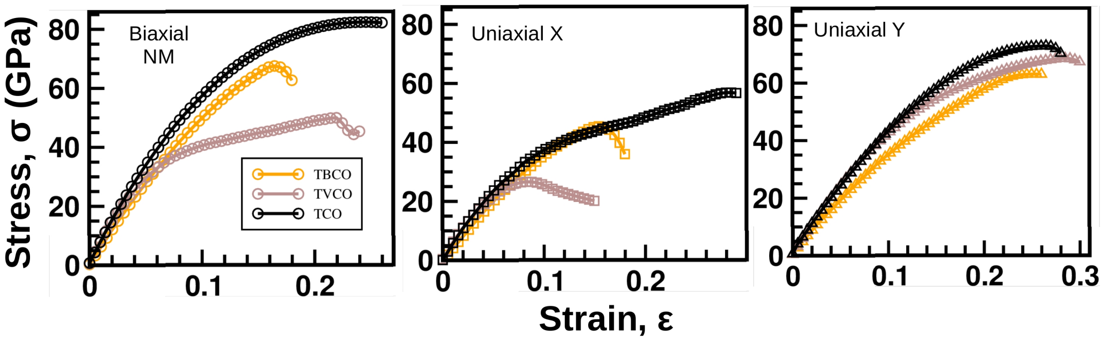

Figure 5.13: The stress-strain curve of Ti_2CO_2 (TCO) , $Ti_2(C_{0.5},B_{0.5})O_2$ (TBCO) and $(Ti,V)CO_2$ (TVCO) under biaxial and uniaxial tensile strains along the X and Y directions.

5.4 Conclusions

The newest addition to the list of 2D materials with fascinating properties are MXene compounds, which are 2D counterparts of 3D hexagonal MAX compounds. To make these materials commercially useful, an important issue is the tunability of the properties using various approach. Among the various possible routes to do so, one is alloying with other elements. In the present study we focus on the mechanical properties and study the effect of alloying at both X and M sites of MXene. In particular, we take up the representative case of Ti_2C and consider the solid solutions $Ti_2(C_{0.5},B_{0.5})$ and (Ti,V)C. Since the Ti_2C compounds synthesized so far are all reported to be passivated, we also consider the effect of O passivation. Moreover as earlier studies suggested, functionalization of MXenes with different atoms can lead to fundamental changes in the conductive properties, namely, from metal-like to semi-conductor as verified in our calculations too. Our study concludes that B doping of O-passivated Ti_2C compound makes it a system with improved mechanical properties both in terms of reduced stiffness (by about 27%) and extended critical strain (by about 100%) compared to the pristine unpassivated Ti_2C compound. The microscopic origin of the improved elastic properties upon B doping has been traced to the weakening in the covalency of the Ti-B bond compared to that of the Ti-C bond, a fact also supported by phonon calculations.

Our study additionally reports an interesting observation in terms of magnetism of unpassivated Ti_2C, which to the best of our knowledge has remained unexplored so far. We clarify the magnetic ground state to be of A-AFM type having the Ti spins between the top and bottom layers aligned in an antiparallel manner. The stabilization of A-AFM structure drives the semiconducting behaviour of Ti_2C as compared to previously reported metallic or half-metallic behaviour of Ti_2C [68, 206]. Interestingly we find that AFM order hardens the phonon frequencies having the significant influence on the out-of-plane layer-bending or rippling mode. This makes unpassivated Ti_2C in its ground state A-AFM structure withstand larger strain compared to that of NM Ti_2C. This in turn highlights the significant role of spin-phonon coupling in magnetic MXene materials, a topic which needs to be explored in the future.

Chapter 6

Properties at the interface of graphene and Ti_2C MXene

6.1 Introduction

Two-dimensional (2D) materials can exhibit a variety of electronic properties, graphene being metallic, MoS_2 being semiconducting and *h*-BN being insulating in nature. Hence, for technological applications this class of materials is attractive often in combinations. There have been several recent efforts towards fabricating heterostructures, which are vertical stacks of 2D dissimilar materials held together by van der Waals (vdW) forces. While taking advantage of the unique set of individual properties, such heterostructuring may result in properties entirely different from their individual components. This opens up new opportunities for materials designing. A prominent example in this respect are the heterostructures between transition-metal dichalcogenide (TMD) 2D semiconductors, such as MoS_2, WS_2, $MoSe_2$ as well as *h*-BN, and graphene. Such heterostructures have led to opening of bandgap in graphene [207, 208, 209], drastic improvement of on/off current ratios [210, 211, 212] and also tuning of mechanical properties

---

This chapter is based on "Properties at the interface of graphene and Ti_2C MXene" - Pallavi Paul, *Poulami Chakraborty*, Tilak Das, Dhani Nafday, and Tanusri Saha-Dasgupta, Phys. Rev. B **95**, 035435 (2017)

[213]. However, the number of different heterostructures that one can obtain following this route is large, and their physical properties are hard to predict before measurement. *Ab initio* modeling is suitable in this respect for studying structure-property relations.

Graphene, one of the most studied two-dimensional (2D) atomic-layer-based material, is a zero-gap semiconductor with a point-like Fermi surface and a linear dispersion close to Fermi level [214]. Since its discovery it has attracted enormous attention due to its unique physical properties and plausible applications in novel electronic devices [215, 216]. On the other hand several studies carried out by Barsoum and co-workers [41, 154] have made popular a new class of 2D material named MXenes which are derived from its 3D counterpart named MAX phases through exfoliation as already discussed in the previous chapters. In recent studies, MXenes have demonstrated versatile electronic properties and potential applications to energy storage [70, 184, 217, 218]. Heterostructuring these two attractive class of materials, namely MXene and graphene are expected to generate unexplored, novel properties. This motivated the present study. In this study, we have chosen the specific case of Ti_2C, which is the most common member of the MXene family and the lightest MXene exfoliated from the parent 3D Ti_2AlC MAX phase [68]. Density functional theory (DFT)-based first-principles calculations have been employed to explore the geometry, bonding, phonon, optical, electronic, and magnetic properties of the graphene-Ti_2C hybrids. Two geometries, namely the overlayer geometry with graphene placed on top of Ti_2C and the sandwich geometry with a monolayer of Ti_2C sandwiched between two graphene sheets, have been considered. We have also analysed the hybrid structures formed between oxygen-passivated Ti_2C (Ti_2CO_2) and graphene.

6.2 Computational Details

First-principles DFT calculations have been performed using the choice of generalized gradient approximation (GGA) of the Perdew-Burke-Ernzerhof (PBE) exchange-correlation functional [93] and the plane-wave basis as implemented in the Vienna Ab initio Simulation Package (VASP) [164]. The projector-augmented wave (PAW) potentials [219] have been used. For Ti, we have used the [Ar]3p3d4s configuration as the valence configuration, while for C and O, [He]2s2p configurations have been used as the valence. 600 eV energy cutoff has been chosen to expand the plane-wave basis and 10^{-6} eV tolerance has been set as the convergence criteria of the self-consistent ground-state energy calculations. Geometry relaxations have been done until the maximum value of the force component is converged to a value below 0.01 eV/Åwith a dense Γ-centered 42 x 42 x 1 Monkhorst-Pack k-point [191] grid. A damped van der Waals (vdW) correction (DFT-D2) has been added to the DFT exchange-correlation functional to incorporate the effect of nonbonding forces [189].

To understand the influence of heterostructure geometry on the infrared and Raman active phonon modes, Γ-point phonon calculations were carried out within the formulation of density functional perturbation theory (DFPT) [193] as implemented in the QUANTUM ESPRESSO (QE) code [194]. As such, calculations were performed for the pristine graphene, pristine Ti_2C, and the graphene/Ti_2C heterostructure systems whose ground-state geometries were obtained by VASP. We have also checked the geometries by carrying out additional structural optimization within QE code. The changes are found to be only marginal. Ultrasoft pseudopotentials of Garrity *et al.* [195] were used along with PBE-GGA as the exchange-correlation functional. The energy cutoffs for the wave function and charge density were set to about 816 and 8164 eV, respectively, and the energies were converged to 10^{-10} eV. The computed dynamical matrix was diagonalized to obtain the eigenvalues which are the phonon frequencies for the system.

6.3 Ti_2C-Graphene Heterostructures

At first we investigated the electronic structure of an isolated graphene layer and the Ti_2C layer. Graphene which is one of the most studied 2D material, is known to be a zero-gap semiconducting material with a Dirac (linear) band crossing at the K and K' points of the hexagonal Brillouin zone (BZ) [220]. Magnetic structure of Ti_2C shows A-type antiferromagnetic (A-AFM) spin configuration, with Ti moments between the top and bottom layers of the Ti_2C structure aligned in an antiparallel manner [5]. The stabilization of antiferromagnetism makes Ti_2C a semiconductor with an estimated band gap of 0.2 eV. The in-plane lattice

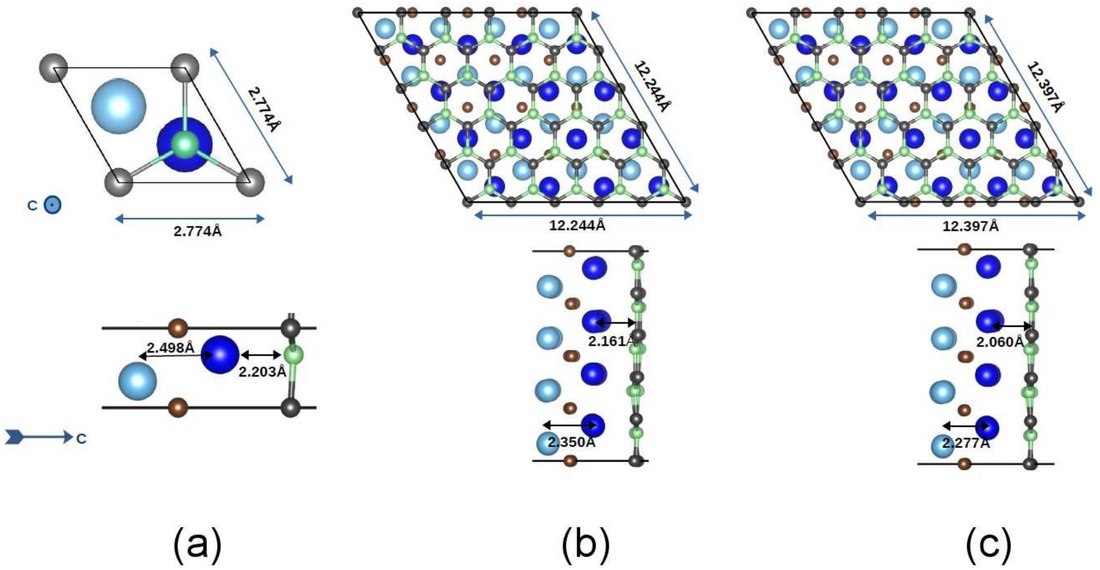

Figure 6.1: Top view and side view of the fully optimized geometries for the three models of graphene/Ti_2C hybrid structure: (a) 1 x 1 geometry, (b) 5 x 5@4 x 4 (A), (c) 5 x 5@4 x 4 (B). The dark blue (light blue) balls represent Ti atoms of top(bottom) layer of Ti_2C monolayer, whereas brown balls indicate the C atoms of Ti_2C monolayer which are sandwiched between the Ti atoms. The C atoms in graphene are shown by light green (dark grey) balls.

constants of the optimized freestanding Ti_2C and graphene are found to be 3.06 and 2.46 Å, respectively which results in a large lattice mismatch of 24%. Keeping this in mind, we have modelled the graphene/Ti2C heterostructures in three different possible ways which are discussed in the following section.

Possible Models

There are different possibilities in modeling the graphene/Ti_2C hybrid structures. One possible model is that the Ti_2C and graphene will adopt a common lattice parameter and form a commensurate structure with a minimal cell size with a 1 x 1 cell of graphene placed on a 1 x 1 cell of Ti_2C (referred as 1 x 1 structure in the following). This would cost large strain energy which may be compensated by possible gain in covalency induced energy. The common optimized lattice constant of the 1 x 1 structure of graphene/Ti_2C hybrid was obtained by plotting the sum of the total energies of Ti_2C and graphene, $E_{tot} = (E_{Ti_2C} + E_{gr})$, as a function of the common in-plane lattice constant, varied within the range 2.4 to 3.4 Å. It shows a parabolic behaviour with a minimum at 2.9 Å, resulting in a compressive strain of 5% on Ti_2C and tensile strain of 18% on graphene. The optimized structure is shown in Fig. 6.1(a). The other possible model to consider is a bigger supercell, where a 5 x 5 graphene layer is placed on top of a 4 x 4 Ti_2C layer which would reduce the mismatch between Ti_2C layer and graphene layer. This can be done in the following two ways. Firstly, a 5 x 5 supercell of graphene was stacked on top of a 4 x 4 supercell of Ti_2C monolayer. Here, 5 times lattice parameter of graphene and 4 times lattice parameter of Ti_2C leads to a small mismatch of only 0.5%. Full relaxation of atomic coordinates was carried out by applying a small compressive strain to the graphene sheet to match that of the inplane lattice constant of Ti_2C while the latter is kept fixed. The optimized geometry is referred as 5 x 5@4 x 4 (A) geometry as shown in Fig. 6.1(b). The second method followed a similar stacking sequence but the optimization procedure was different here. Here no compressive strain was applied to graphene. The inplane lattice constant of Ti_2C was kept fixed and relaxation of only the atomic coordinates was allowed for both graphene and Ti_2C sheets. This allows the graphene inplane lattice constant to adjust to that of Ti_2C. The resultant geometry, referred as 5 x 5@4 x 4 (B) was then fully relaxed in both lattice constants and atomic geometry causing the lattice mismatch to disappear as shown in Fig. 6.1(c). In the above cases, the generated 2D structures were considered within the periodic set-up with a vacuum layer of 20 Å along the out-of-plane lattice constant, i.e., the z direction. While in a 1 x 1 cell the atoms on the top layer of Ti_2C point towards the atoms of the graphene layer, in the 5 x 5@4 x 4 structures the atoms between the two layers are misaligned. We considered all three possibilities.

Finally, we compared the relative stability of the three models. Since the number of atoms in the 1 x 1 and 5 x 5@4 x 4 structures are rather different, i.e., 5 and 98, respectively, a comparison of energies is not meaningful. We thus compared the cohesive energy (E_{coh}) and formation enthalpy (ΔH_f) of the three models. The cohesive energy was defined as $E_{coh} = E_{hyb} - E_{gr} - E_{Ti_2C}$, where E_{hyb}, E_{gr}, and E_{Ti_2C} are the energies of the heterostructure, graphene, and

Table 6.1: The relaxed lattice constants (a_{gr}, a_{Ti_2C}), cohesive energy (E_{coh}) and enthalpy of formation ΔH for the three graphene/Ti_2C hybrid structures.

Models	Lattice constants (Å)	E_{coh} (eV/Ti_2C f.u.)	ΔH (eV/atom)
1 x 1	$a_{gr} = 2.9$ $a_{Ti_2C} = 2.9$	-1.314	-6.302
5 x 5@4 x 4 (A)	$a_{gr} = 2.45$ $a_{Ti_2C} = 3.06$	-0.876	-6.160
5 x 5@4 x 4 (B)	$a_{gr} = 2.48$ $a_{Ti_2C} = 3.10$	-0.901	-6.302

Ti_2C in the heterostructure geometries. The formation enthalpy was defined as $\Delta H_f(A_{n1}, B_{n2} \ . \ . \ .) = E(A_{n1}, B_{n2} \ . \ . \ .) - \sum_i n_i \mu_i$, where μ_i is the chemical potential, i.e., the energy of A and B atoms in their elemental form. Calculated values of cohesive energy in units of eV per Ti_2C formula unit and formation enthalpy in units of eV per atom for the models are given in Table 6.1. Our calculations showed that the 1 x 1 structure with common lattice parameters of Ti_2C and graphene layer are favoured compared to the 5 x 5@4 x 4 structures. In the following, we have thus reported only the results for the 1 x 1 cell. The formation of chemical bonds between atoms of Ti_2C with graphene C atoms explains why the 1 x 1 structure is more stable than 5 x 5@4 x 4 structures. The chemical bonds are not formed in the other two models of 5 x 5@4 x 4 due to the misalignment of atoms between the two layers. The strain energy cost due to the large lattice mismatch in the 1 x 1 model is overcome by the gain in bond energy which renders this as the most stable structure among the three. This is in contrast to other hybrid structures such as graphene-MoS_2 or transition-metal dichalcogenide/transition-metal dichalcogenide heterostructures [221, 222] where van der Waals bonds are formed for which the supercell structure is more favourable. However, the dynamical stability of the 1 x 1 structure is yet to be studied. Also there may be possible structures with domains separated by dislocations, etc. which has not been studied. It will be interesting to study these possibilities in the future.

6.3.1 Overlayer Geometry

Considering the 1 x 1 geometry of graphene on top of Ti_2C, three possible stacking configurations can be obtained, as shown in the top panel of Fig. 6.2. Configuration-1 (conf-1) as shown in Fig. 6.2(a) has a sublattice A atom of graphene (C_A) above the Ti atom in the top layer of Ti_2C and a sublattice B atom of graphene (C_B) above the C atom of Ti_2C. In configuration-2 (conf-2) (cf. Fig. 6.2(b)), C_A is above the Ti atom in the bottom layer of Ti_2C, while C_B is above the C atom of Ti_2C. Configuration-3 (conf-3), shown in top panel of Fig. 6.2(c), represents the stacking where C_A and C_B are above the Ti atoms in the top and bottom layers of Ti_2C, respectively. Structural optimizations were carried out for the above described three different stackings by varying the interlayer separation between graphene and Ti_2C from 1.5 to 3 Å in steps of 0.25 Å. Optimal interlayer separations obtained for the three cases are listed in Table 6.2. We find that the optimized geometries show a rather strong dependency on the stacking pattern. As shown in the charge density plot of Fig. 6.2, strong overlap of electronic wave functions happens between graphene and the top layer of Ti_2C. The difference in strength of the covalency between the C_A and C_B atoms with the atoms beneath belonging to Ti_2C leads to buckling of the graphene layer, with the extent of buckling being different in the three configurations (cf. Table 6.2). We find that in the cases of conf-1 and conf-3, the buckling is appreciable, while for conf-2, it is largely suppressed. This can be rationalized by the fact that while conf-1 and conf-3 are highly asymmetric with respect to C_A and C_B atoms of graphene, with C_A lying above the Ti atom in the top layer of Ti_2C and C_B lying above the C atom in the middle layer or the Ti atom in the bottom layer of Ti_2C, conf-2 is more symmetric with the top Ti atom of Ti_2C occupying the hollow site formed by the hexagon consisting of three C_A atoms and three C_B atoms. This also makes the average interlayer separation between Ti_2C and graphene different in the three different cases of stacking. The calculated cohesive energy of the hybrid systems shows conf-3 to be the most stable one, which has

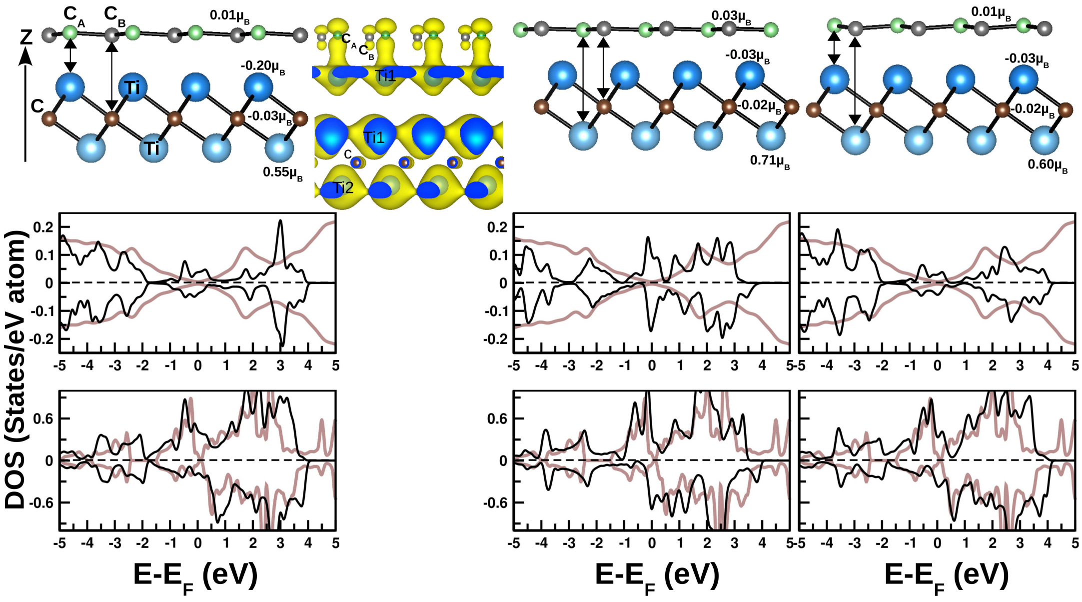

(a) (b) (c)

Figure 6.2: The overlayer geometries of graphene/Ti$_2$C in three possible stacking configurations, in side views are shown in top panels for (a) conf-1, (b) conf-2 and (c) conf-3. The large balls represent Ti atoms, while the small balls represent C atoms. The Ti atoms belonging to top and bottom layers of Ti$_2$C have been coloured differently. The carbon atoms belonging to A and B sublattices of graphene have been marked as well as coloured differently (green and grey), while the C atoms belonging to Ti$_2$C have been distinguished with a different colour (brown). Also the magnetic moment at a given site is marked. The charge density plot of the graphene/Ti$_2$C conf-1 heterostructure obtained from contribution of states close to Fermi level is shown by side of conf-1 geometry. The isosurface value has been set to 0.02 $e^-/\AA^3$. The corresponding density of states projected onto C p states of graphene in graphene/Ti$_2$C heterostructure (in black) compared to that of free standing unstrained graphene structure (brown) are shown in middle panels. The density of states projected to Ti d states of Ti$_2$C in graphene/Ti$_2$C heterostructure (in black) in comparison to that in free standing Ti$_2$C are shown in the bottom panels.

both C_A and C_B atoms forming $pd\sigma$ bonds with top and bottom layer Ti atoms of Ti$_2$C.

Table 6.2: Cohesive energy (E_{coh}), average interlayer separation, buckling of graphene layer in the graphene/Ti_2C heterostructures in overlayer and sandwich geometries.

Geometry	Models	E_{coh} (eV)	Average Interlayer Separation (Å)	Buckling of Graphene (Å)
Overlayer	conf-1	-1.314	2.121	0.102
	conf-2	-1.405	1.838	0.051
	conf-3	-1.467	2.080	0.124
Sandwich (Similar Interface)	1-1	-2.661	2.145	0.092
	2-2	-3.094	1.831	0.090
	3-3	-3.037	2.087	0.122
Sandwich (Dissimilar Interface)	1-2	-2.805	2.136	0.091
			1.863	0.059
	1-3	-2.878	2.127	0.095
			2.010	0.120
	2-3	-3.082	1.834	0.071
			2.056	0.132

The middle and bottom panels of Fig. 6.2 show the spin-polarized density of states (DOS) projected to C p states of graphene and Ti d states of Ti_2C in the hybrid overlayer structure in comparison to the corresponding DOS in isolated graphene and Ti_2C monolayers, respectively. We notice a strong renormalization of the graphene DOS in the hybrid structure compared to the isolated form. This gives rise to a finite density of states at the Fermi level (E_F), which shows strong hybridization with Ti d DOS, thereby also giving rise to finite spin splitting of the graphene states close to E_F. The latter is reflected in the calculated magnetic moments which show small but finite moment (0.03-0.01 μ_B) at C atoms of graphene (cf. Fig. 6.2). Moving to the Ti d contribution, we find that while the Ti spins in the top and bottom layers of Ti_2C in the hybrid remain antiparallel, reminiscent of the A-type AFM magnetic configuration of Ti_2C in isolation [5], the Ti moments on the top layer adjacent to the graphene layer get strongly quenched. The quenching is found to be strong for conf-2 and conf-3, which reduces the atom-centered magnetic moment at the Ti site from a value of 0.6-0.7 μ_B to 0.03 μ_B, while it is only partial for conf-1, reducing to a value of 0.20 μ_B. This leads to a ferrimagnetic solution in the Ti_2C block of the hybrid, as opposed to the A-type AFM solution of Ti_2C in isolation. We further find that while the structure of the DOS close to E_F is rather similar between conf-1 and conf-3 with Ti of the top layer of Ti_2C forming direct bonding with C of the graphene layer, the features are different for conf-2.

This difference in the electronic structure of different stacking is evident in the calculated optical conductivity, shown in bottom panels of Fig. 6.3. The projected DOS are shown in the upper panels of Fig. 6.3. The DOS is projected onto C p states of graphene, Ti d states of Ti_2C, and C p states of Ti_2C. The optical conductivity is the convolution of joint density of states (JDOS) and the transition probabilities or the dipole matrix elements, given by [223]

$$\sigma_{ij}(\omega) \;=\; \frac{4\pi^2 e^2}{\Omega m^2 \omega^2} \sum\nolimits_{knn'\sigma} \langle kn\sigma | p_i | kn'\sigma \rangle \langle kn'\sigma | p_j | kn\sigma \rangle \; \delta(e_{kn'} - e_{kn} - \hbar\omega)$$

where e and m are the charge and mass of the electron, Ω is the volume of the unit cell, ω is the photon energy, and $e_{\mathbf{k}n}$ and $e_{\mathbf{k'}n}$ are the eigenvalues of the final

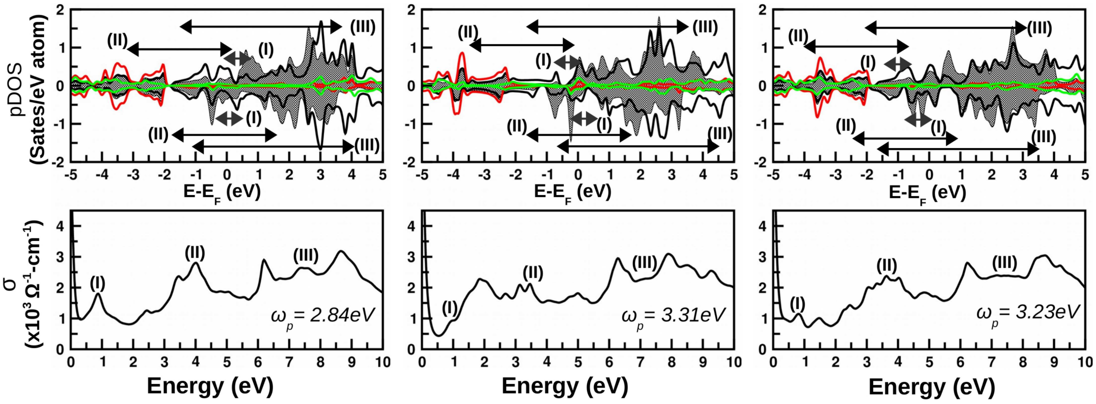

(a) (b) (c)

Figure 6.3: Top panels: Partial density of states (pDOS) plotted against the energy, with zero of energy set at E_F and the corresponding optical conductivity are shown for (a) conf-1, (b) conf-2 and (c) conf-3 of the overlayer geometry of graphene/Ti_2C. The pDOS for top layer Ti d, bottom layer Ti d, C p states of Ti_2C are shown in black line, shaded area, and red line, respectively. The pDOS for C p states of graphene is shown in green line. Marked are the various possible optical transitions. Bottom panels: The corresponding optical conductivity

and initial states at the k point in the BZ for a given spin channel. The JDOS is given by

$$JDOS(\omega) \;=\; \frac{4\pi^2 e^2}{\Omega m^2 \omega^2}\sum\nolimits_{knn'\sigma} \delta(e_{kn'} - e_{kn} - \hbar\omega)$$

$\langle kn\sigma|p_i|kn'\sigma\rangle$ is the dipole matrix element evaluated in the basis of the Kohn-Sham orbitals. To the above defined optical conductivity, the Drude contribution due to the intraband transitions pertinent for the metallic systems is added, from the knowledge of plasma frequency, (ω_p). The values of computed plasma frequency are marked in Fig. 6.3. The resultant optical conductivity, shows the sharp Drude peak and the dip following Drude peak known as plasma edge, shows three prominent features marked as (I), (II) and (III). Analysing the partial density of states, as shown in top panels of Fig. 6.3, we find the probable origins of the three peaks. The feature (I) at very low energy arises due to optical transition from primarily nonbonding Ti *d* to nonbonding Ti *d* states. This transition becomes allowed by the symmetry rule due to finite mixing between Ti *d* and graphene C *p* states. The feature (II) arises due to optical transition from bonding C *p* of Ti_2C to nonbonding Ti *d* states, while feature (III) originates from transitions between nonbonding Ti *d* and antibonding Ti *d* states. It can be seen from Fig. 6.3 while the feature (I) is almost masked by the Drude peak and the plasma edge effect in the case of conf-3, it is rather pronounced in conf-1, while it nearly overlaps with the broad feature of (II) in the case of conf-2. Thus, while the three-prominent-peak feature is readily visible for conf-1, conf-2 and conf-3 primarily show two prominent features, (II) and (III). Feature (II), which lies in the broad energy range of 1.5 - 3.5 eV for conf-2, gets shifted to the energy range 2.5 - 5.0 eV in conf-3. The measured optical conductivity therefore should show distinct features for conf-1, conf-2 and conf-3, which can be used for identification of the nature of the interfaces formed during the growth of the heterostructures.

To obtain further understanding, Γ point phonon calculations were carried out for individual components as well as for graphene/Ti_2C heterostructure, the results being summarized in Fig. 6.4. We find that the frequencies of graphene are much harder than that of Ti_2C which explains the differences in their elastic behaviour [187, 198]. Formation of the graphene/Ti_2C heterostructure breaks the center of inversion which is present in the individual components, thereby allowing the modes to be both IR and Raman active. It is important to note that the phonon spectra for conf-1 and conf-3 appears to be rather similar suggestive of similar elastic properties driven by the direct bonding between top layer Ti *d* and p_π states of graphene. Analyzing the modes, we find conf-1 and conf-3 exhibit modes with combined movement of atoms in both graphene and Ti_2C layers as well as modes involving only movements of graphene or Ti_2C layer. However, in case of conf-2, all modes involve combined movement of atoms in both graphene and Ti_2C. The combined or joint graphene-Ti_2C modes can be either a combination of an acoustic mode in the graphene layer and an optic mode in the Ti_2C layer, or both optic/acoustic modes in the individual graphene and in the Ti_2C layers, as shown in Fig. 6.4.

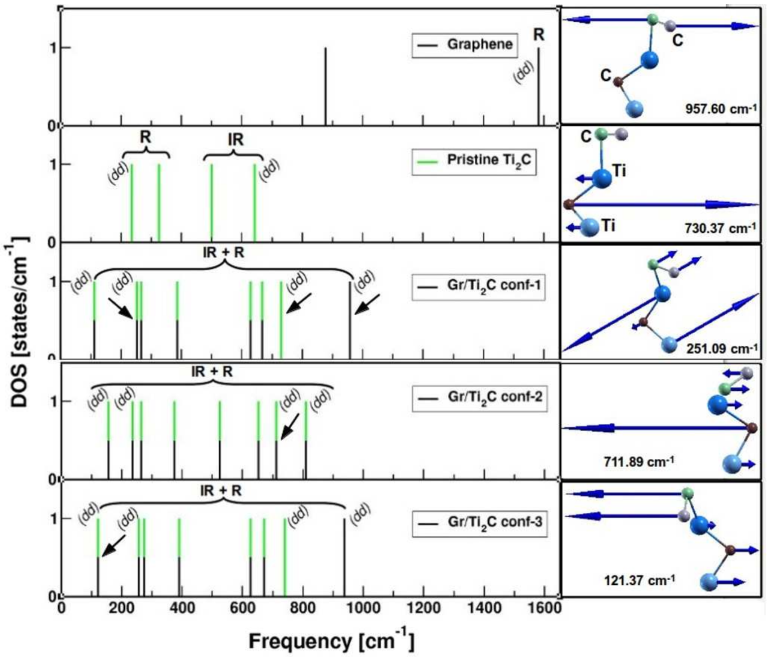

Figure 6.4: Phonon density of states for pristine graphene, pristine Ti_2C, graphene/Ti_2C heterostructures in conf-1, conf-2 and conf-3 of the overlayer geometry. The various infra-red (IR) active and Raman (R) active modes have been marked. The doubly degenerate modes are marked as *dd*. The graphene and Ti_2C modes are shown in black, green colours, respectively, while the joint graphene-Ti_2C modes are shown in part black-part green colour. The atomic displacements corresponding to the phonon modes in heterostructures having displacements confined solely to graphene layer, solely to Ti_2C layer and to both Ti_2C and graphene layers are also shown by side.

6.3.2 Sandwich Geometry

We have also considered the sandwich geometry of the graphene/Ti_2C/graphene heterostructures where the monolayer of Ti_2C is sandwiched between two layers of graphene. This results in two interfaces, one is between graphene and top layer of Ti_2C and the other being graphene and bottom layer of Ti_2C. This leads to two types of possible interfaces, either both interfaces are of similar type or of dissimilar type. There are three different possibilities of similar interfaces, of type 1-1: both interfaces having conf-1 geometry, type 2-2: both interfaces

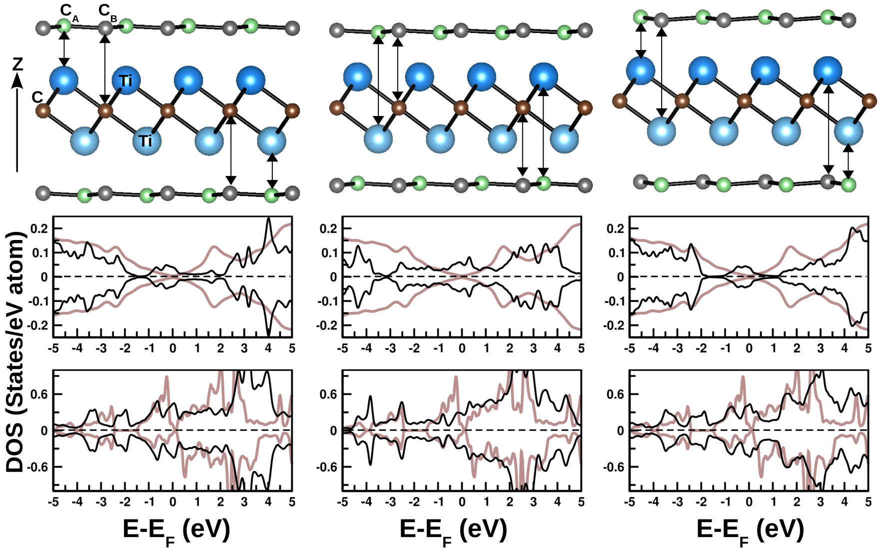

(a) (b) (c)

Figure 6.5: Top panels: The sandwich geometries of graphene/Ti_2C/graphene considering two similar interfaces, 1-1, 2-2, 3-3 configurations [(a),(b),(c) respectively]. As in Fig. 6.2 large balls represent Ti atoms, while the small balls represent C atoms. The density of states in the middle panels are projected to C p states of graphene in graphene/Ti_2C/graphene heterostructure (in black) as compared to that of graphene in isolation (brown). Similarly the corresponding Ti d states of Ti_2C are plotted in the bottom panels.

having conf-2 geometry and type 3-3: both interfaces having conf-3 geometry. Similarly there exists three different possibilities of dissimilar interfaces, of type 1-2, type 1-3 and type 2-3. The resulting configurations for sandwich geometry with similar interfaces are shown in top panels of Fig. 6.5 and dissimilar interfaces are shown in top panels of Fig. 6.6. Computed values of cohesive energy, average interlayer separation, buckling of graphene layers are listed in Table 6.2. Analysing the results we find that interfacing of Ti_2C layer from both sides with graphene quenches the magnetism of Ti atoms completely resulting into nonmagnetic solution in all cases. The strong hybridization between C atoms of graphene and Ti_2C makes the graphene layer as well as the Ti_2C layer conducting. Two interlayer separations as well as the buckling of the two graphene layers maintain

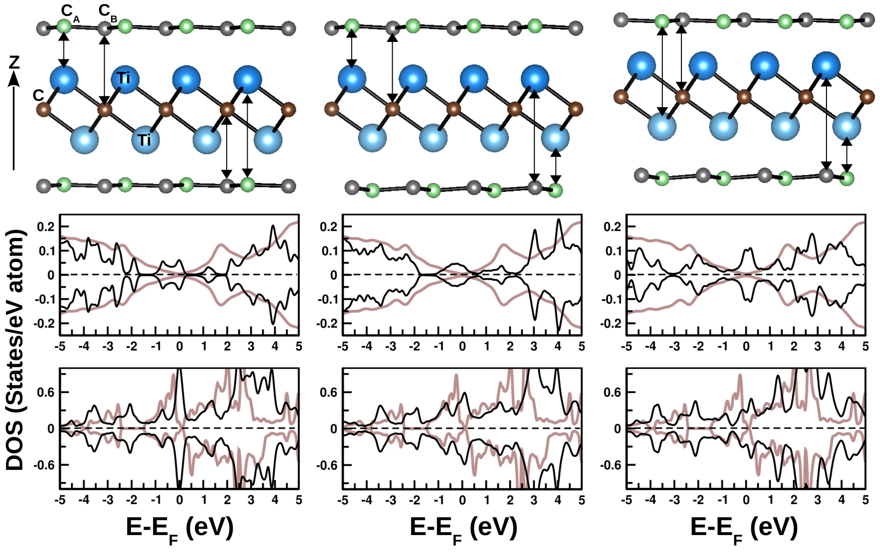

(a) (b) (c)

Figure 6.6: Top panels: The sandwich geometries of graphene/Ti_2C/graphene considering two dissimilar interfaces, 1-1, 2-2, 3-3 configurations [(a),(b),(c) respectively]. As in Fig. 6.2 large balls represent Ti atoms, while the small balls represent C atoms. The density of states in the middle panels are projected to C *p* states of graphene in graphene/Ti_2C/graphene heterostructure (in black) as compared to that of graphene in isolation (brown). The corresponding Ti *d* states of Ti_2C are plotted in the bottom panels.

the general trend followed in overlayer geometry. The cohesive energies are found to be doubled due to the presence of two interfaces having strong covalent bonds.

6.4 Ti_2CO_2-Graphene Heterostructures

Finally, we have also considered interfaces between graphene and O passivated Ti_2C which makes the native Ti_2C nonmagnetic and semiconducting [197]. O atom can be placed on Ti_2C in three possible configurations: (a) O being placed above the hollow sites formed by three neighboring C atoms on both sides of Ti_2C, (b)oxygen atoms placed directly above the C sites on both sides of Ti_2C, or (c) having a combination of (a) on one side of Ti_2C and (b) on the other side

Table 6.3: Cohesive energy (E_{coh}), average interlayer separation, buckling of graphene layer in the graphene/Ti_2CO_2 heterostructures in overlayer and sandwich geometries.

Geometry	Models	E_{coh} (eV)	Average Interlayer Separation (Å)	Buckling of Graphene (Å)
	conf-1	-0.012	3.928	0.0
Overlayer	conf-2	-0.012	3.945	0.0
	conf-3	-0.012	3.936	0.0
Sandwich	1-1	-0.039	4.067	0.0

of Ti_2C. A comparison of the energetics shows that configuration (a) gives the minimum-energy configuration. We have worked with the lowest energy Ti_2CO_2 configuration. Fixing the Ti_2CO_2 configuration, there are yet three possible stacking configurations for graphene/Ti_2CO_2 similar to that of graphene/Ti_2C. The calculated cohesive energies are listed in Table 6.3, which indicate that graphene-Ti_2CO_2 interaction is insensitive to the stacking pattern indicative of physisorption process in contrast to chemisorption as in the case of graphene and Ti_2C. Due to this weak nature of interaction the interlayer separation is found to be twice that of graphene and Ti_2C. The graphene layer also does not show any buckling induced by the MXene layer. However, construction of graphene/Ti_2CO_2 heterostructure lead to about 15% tensile strain on graphene and about 6% compressive strain on Ti_2CO_2. This large expansion makes the graphene insulating and Ti_2CO_2 metallic with creation of a hole pocket and an electron pocket at the Fermi surface as shown in Fig. 6.7 for conf-1 stacking of the graphene/Ti_2CO_2 interface. Similar electronic behaviour has been observed for conf-2 and conf-3 as well. Sandwich geometries arising from graphene/Ti_2CO_2/graphene heterostructure lead to similar results with stacking insensitive low cohesive energy and large interlayer separation suggestive of weak interaction between graphene and Ti_2CO_2 layers. The computed electronic structure also shows similar trend with metallic conductivity arising from Ti_2CO_2 layer, and insulating behaviour of the

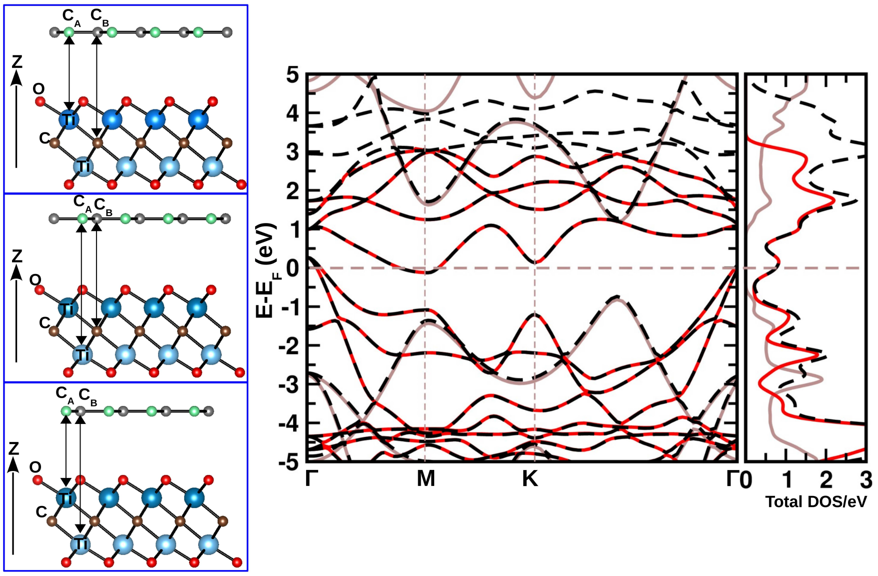

Figure 6.7: Left panels: The stacking of graphene on Ti_2CO_2 in conf-1, conf-2 and conf-3 (from top to bottom) are shown. The large balls represent Ti atoms with Ti atoms belonging to top and bottom layers of Ti_2 colored different, while the small balls represent C and O atoms. The C atoms belonging to A and B sublattice of graphene layer are marked in grey and green layers, while the C atoms belonging to Ti_2C are coloured in brown. The oxygen atoms are coloured in red. Right panels: The bandstructure and the total DOS of graphene/Ti_2CO_2 in conf-1 with the composite bandstructure are shown in black dashed line, that projected to Ti_2CO_2 in red solid line, and that projected to graphene in brown solid line respectively.

graphene layers.

6.5 Conclusion

Density functional theory based first-principles calculations have been employed to explore the geometry, bonding, phonon, optical, electronic and magnetic properties of the graphene-Ti_2C hybrids. Two geometries, namely the overlayer geometry with graphene placed on top of Ti_2C, and the sandwich geometry, with a monolayer of Ti_2C sandwiched between two graphene sheets, have been considered. We have also analyzed the hybrid structures formed between oxygen passivated Ti_2C (Ti_2CO_2) and graphene. Our study shows that graphene in contact with Ti_2C leads to formation of strong chemical bonds between d states of Ti atoms and p_π states of graphene C atoms unlike other heterostructures formed between graphene/transition metal dichalcogenide or transition metal dichalcogenide/transition metal dichalcogenide which bound by van der Waals forces. Following this a strong stacking dependent reconstruction of the electronic structure happens at the interface, making it metallic though graphene is a zero gap semiconductor and Ti_2C in its antiferromagnetically ordered state is a semiconductor with a gap of ≈ 0.2 eV. This reconstruction also makes the Ti_2C block of the heterostructure ferrimagnetic with large quenching of moments at Ti atoms facing graphene. We computed the optical conductivity as well as phonon properties of the constructed heterostructures, which show strong dependency on the stacking pattern. The characterization of stacking arrangement thus should be possible through experimental measurement of optical conductivity or use of IR and Raman spectroscopic techniques. We have also considered the heterostructures with sandwiched geometry forming two interfaces between Ti_2C and graphene. This resulted in complete quenching of Ti moments giving rise to a nonmagnetic metallic state. Our study further showed that consideration of O passivated Ti_2C, changes the above scenario completely, making the graphene-Ti_2C interaction a weak physisorption process which shows negligible dependency on stacking arrangement. This, however leads to metallic solution with low density of states as opposed to semiconducting or insulating solution, due to formation of electron and hole pockets in the electronic structure of Ti_2C under large compressive strain. Our rigorous theoretical investigation should be helpful for future experimantal activity in this direction.

Chapter 7

Conclusion

The focus of the thesis was to have a microscopic investigation of mechanical properties of three different classes of complex materials. The electronic and magnetic properties and their influence on mechanical properties have been also studied in cases. For this purpose, different computational techniques have been used. In particular, first principles electronic structure calculations were performed within the framework of Density Functional Theory (DFT) and classical molecular dynamics simulations with classical potential were used to study the properties at the atomistic scale. The present chapter is a summary of the primary findings that emerged out of our study, as described in chapters 3 to 6. This is followed by a discussion on possible future work.

7.1 Summary

7.1.1 Chapter 3

In this chapter we studied hydrogen embrittlement problem in Zr alloys. This is one of the main cause of mechanical degradation of fuel cladding in nuclear reactors and is regarded as one of the most important issues in safety regulation for nuclear power plants. Therefore, microscopic understanding of the embrittlement process upon H incorporation in Zr is necessary and forms the focus of our study. For this purpose we carried out large scale molecular dynamics simulation based on classical pair potential. Using large scale molecular dynamics simulation in the dilute and concentrated H limits, we studied the effect of 1-5 atomic percentage of hydrogen, and that of ϵ-ZrH_2 precipitates having 5-10 nm diameters, respectively. Our study revealed that H atoms in dilute limit help in dislocation multiplication, following the hydrogen-enhanced localized plasticity mechanism. In the concentrated limit, on the other hand, dislocations and cracks nucleate from precipitate-matrix interface, indicating the decohesion mechanism as primary method for Zr degradation. These findings were corroborated with a nucleation and growth model within the Kolmogorov-Johnson-Mehl-Avrami equation.

7.1.2 Chapter 4

This chapter was aimed at improving the mechanical properties of the MAX phase compounds which are materials of high technological interest. We considered boron substitution at X component of MAX compound using first-principles density functional theory (DFT) calculations, combined with continuum modeling to access the core structure of dislocations. The effect of boron-substitution on plastic deformation properties was evaluated for MAX phase compound, V_2AlC. Our T=0 K results showed that due to the differential nature of chemical bonding between V and B compared to that between V and C, both V-Al and V-B basal slip planes get activated in boron-substituted compounds, compared to only V-Al basal slip in the parent compound. This in turn made the boron compounds significantly more ductile compared to their carbide counterpart, V_2AlC. Furthermore, phonon calculations were carried out to compute the vibrational free energies to predict the stable stacking fault energies in finite temperature. The influence of temperature was found to affect the V-X (X = C, B) and V-Al layers in a contrasting manner, the effect being more pronounced for boride than its carbide counterpart.

7.1.3 Chapter 5

This chapter was devoted to the study of the 2D derivatives of MAX phase, namely MXenes. In the applications based on 2D materials, an essential requirement is the flexibility under application of strain. In our work the effect of substitutional doping of Ti by V and C by B on the mechanical properties of a specific MXene compound Ti_2C were evaluated. Calculations of quantities such as in-plane stiffness, Young's modulus, and critical strain through first-principles technique established that B doping is highly effective in improving the elastic properties. Oxygen passivation of B-doped Ti_2C in addition to improving elastic properties, also was found to provide reasonably high critical strains making them ideally suited for applications in flexible devices. Our study further unravelled the presence of strong spin-phonon coupling in the unpassivated Ti_2C compounds, in turn influencing the mechanical behaviour.

7.1.4 Chapter 6

In this chapter we explored the properties at the interface of MXene and graphene. We know that the creation of the hybrid/composite structure between two different materials may lead to novel properties at the interface of the two which may not be shared by either of the components. This motivated us to consider the MXene/graphene hybrid system. We considered MXene Ti_2C as well as Ti_2CO_2 for our study. The interface was found to be metallic in case of graphene and Ti_2C hybrid structure due to the formation of chemical bonds between Ti and C of graphene. The optical and phonon properties of the interfaces were found to be strongly dependent on the stacking arrangement, driven by the nature of chemical-bond formation. However, graphene on Ti_2CO_2 was found to weaken the bonding between the two, being suggestive of a physisorption process, rather than chemisorption process.

7.2 Outlook

While the present thesis attempts to provide microscopic understanding of properties in certain interesting class of materials, clearly vast possibilities are left unexplored. The following sections discuss few such issues which may be considered for future work.

7.2.1 Dislocation properties of Zr

H embrittlement problem in Zr has been studied in the present thesis employing classical potentials for modelling the system using Molecular Dynamics approach. A more microscopic approach would be first-principles calculation of dislocation properties by calculating Generalised Stacking Fault energy (GSFE) curves. This should provide information of favourable planes for formation of stacking fault, e.g. comparison between $01\bar{1}0$ prismatic plane and 0001 basal plane, possible formation of partial dislocations, etc. In order to understand the deleterious effect of H in Zr systems the GSFE curves with varying distance of H from the slip plane as well as the shape of the curve with varying H concentrations should be investigated. This exercise can be extended to study the effect of various solute atoms on the dislocation properties of Zr so as to increase the fracture toughness of the material and make it more ductile.

7.2.2 MAX phases

Theoretical studies related to MAX phase properties are primarily based on first-principles calculations which investigate the electronic structure, bonding and other microscopic phenomenon. There are very few theoretical study on the mechanical and structural aspects of these unique set of compounds. On the other hand, the complementary approach to study of dislocation behaviour and their mobility with temperature and strain should be large scale atomistic simulation. The atomistic approach such as molecular dynamics (MD) or Monte Carlo (MC) simulation based on interatomic potentials can be an effective way of analysing deformation behaviour of such layered structures. A reliable interatomic potential should reproduce various fundamental physical properties of relevant elements such as elastic properties, structural properties, defect properties, surface properties, and thermal properties, etc. An interesting future study would be to develop a semiempirical interatomic potential for a 211 MAX phase like V_2AlC based on the MEAM formalism. We can use elastic constants, structural energy differences, surface energy, stacking fault energy, and vacancy formation energy for the determination of model parameter values. The value of the model parameters could be determined by fitting to physical properties of V_2AlC.

In order to develop the MEAM potentials for vanadium, aluminum, carbon, and their alloy systems based on first-principles calculations using density-functional theory (DFT), energy calculations and geometry optimizations of various structures may be performed. For each element, several material parameters obtained from the reference structure may be utilized to determine the model parameters. These materials parameters may include the cohesive energy, equilibrium atomic volume, bulk modulus, and several elastic constants. The most stable crystal structures should be chosen as the reference structures, namely a face-centered cubic (fcc) structure for Al, a hexagonal close packed (hcp) structure for C and a body-centered cubic (bcc) structure for V. The cross pair potential can be constructed by fitting elastic properties from DFT calculations for binary alloys of vanadium and aluminium in the fcc reference structure, aluminum and carbon in the rock-salt (B1) reference structure. Also for binary alloys of vanadium and carbon rock-salt (B1) reference structure can be considered. First, the equilibrium lattice parameter, cohesive energy, bulk modulus, shear modulus may be determined from DFT calculations. The pair potential can then be constructed to fit the equilibrium volume and bulk modulus from ab initio calculations. The new MEAM potentials may be used to find the most energetically favourable structures for their binary alloy combinations such as VC, Al_3V and Al_4C_3. As the number of elements in the alloy increases so does the model parameters. Therefore in case of the ternary system V_2AlC, further work needs to be done to fine-tune the parameters and improve the overall agreement with experiments and DFT calculations. The complex bonding properties of MAX phase V_2AlC furthermore adds to the non-triviliatity in the development of such a potential. Hence this area needs much exploration.

7.2.3 MXenes

MXenes with both long-range ferromagnetic order, and antiferromagnetic order have been theoretically predicted. It would be interesting to find MXene phases with transition metal ions other than early transition metal ions, to enhance the magnetism. In this respect, also etching of A-elements other than Al needs to be explored to cover all possible transition metals carbides that form MAX phases.

One of the interesting idea put forward in this thesis is the formation of solid solution phase with borides, together with carbides. This has enormous potential in modulating mechanical properties as revealed in theoretical calculations. The discovery of large magneto-structural coupling should be pursued in more detail, in terms of designing new magneto-capacitive and magneto-electric 2D materials. Magnetic MXene phases could be valuable as new layered magnetic materials useful for data storage and magnetic recording.

An important aspect, which has not been touched upon in this thesis, is the possibility of superconductivity in MXene. Superconductivity in low-dimensional systems has recently attracted a lot of interest, due to the possibility of verifying theoretical predictions on the roles of fluctuations on the superconducting states in perfectly 2D system. Experience have shown that the best phonon-mediated superconductors are materials which are metallic, but retain a strong covalent character, the best examples being magnesium diboride (MgB_2) and doped tetrahedral superconductors[224]. Non-magnetic MXenes, which exhibit at the same time metallic character and remarkably stiff bonds, are strong candidates for this sort of superconductivity. Being layered systems, there is also the possibility to exploit the coupling of phonons to free-electron states confined via ad-atom deposition, in analogy to intercalated graphite and Li/Ca-decorated graphene [225]. In very recent time, Mo_2C MXene has been predicted to be superconductor with chemically-tunable critical temperature [226], but this needs to be followed up with further calculations and experimental verification. The discovery of MgB_2 has generated significant interest in layered superconductors, creating much smaller and more flexible superconductors than the current technology. MgB_2 with alternating graphene layers has been found to increase the superconducting efficiency significantly. Discovery of superconductivity in MXene will be an alternative way to achieve this.

References

[1] F. Haurais, Ph.D. thesis, Universit Paris-Saclay (2017). viii, 5

[2] J. Blomqvist, J. Olofsson, A. M. Alvarez, and C. Bjerkén, Structure and Thermodynamical Properties of Zirconium Hydrides from First-Principle, *Proceedings of the 15th International Conference on Environmental Degradation of Materials in Nuclear Power Systems - Water Reactors* (2016). viii, 6

[3] R. A. Andrievski, Physics-Uspekhi **60**, 276 (2017). viii, 8

[4] Y. Bai, N. Srikanth, C. K. Chua, and K. Zhou, Crit. Rev. Solid State Mater. Sci. **0**, 1 (2017). viii, 10

[5] P. Chakraborty, T. Das, D. Nafday, L. Boeri, and T. Saha-Dasgupta, Phys. Rev. B **95**, 184106 (2017). viii, 13, 102, 109

[6] R. Meshkian *et al.*, Acta Mater. **125**, 476 (2017). viii, 13

[7] M. Khazaei *et al.*, Phys. Chem. Chem. Phys. **20**, 8579 (2018). viii, 13

[8] M. Ghidiu, M. Barsoum, Y. Gogotsi, A. Fafarman, and A. Dillon (2017), eP Patent App. EP20,150,843,168. viii, 13

[9] J.-H. Liu, X. Kan, B. Amin, L.-Y. Gan, and Y. Zhao, Phys. Chem. Chem. Phys. **19**, 32253 (2017). viii, 13

[10] M. Khazaei, A. Ranjbar, M. Arai, T. Sasaki, and S. Yunoki, J. Mater. Chem. C **5**, 2488 (2017). viii, 13, 14

[11] B. Anasori *et al.*, ACS Nano **9**, 9507 (2015). viii, 13

[12] V. M. H. Ng *et al.*, J. Mater. Chem. A **5**, 3039 (2017). viii, 13

[13] V. N. Borysiuk, V. N. Mochalin, and Y. Gogotsi, Nanotechnology **26**, 265705 (2015). viii, 13

[14] C.-Y. Wang *et al.*, Communications in Theoretical Physics **69**, 336 (2018). viii, 13

[15] B. Anasori, M. R. Lukatskaya, and Y. Gogotsi, Nat. Rev. Mater. **2**, 16098 (2017). viii, 13

[16] P. Chakraborty, T. Das, and T. Saha-Dasgupta, *MXene: A New Trend in 2D Materials Science* (Elsevier, to be published), chap. 10414, 2nd ed. viii, 13

[17] W. Widayani, T. D. K. Wungu, S. E. Marsha, and S. Suprijadi, Journal of Polymer and Biopolymer Physics Chemistry **5**, 10 (2017). viii, 27

[18] V. Bulatov and W. Cai, *Computer Simulations of Dislocations* (Oxford, 2006). viii, ix, 39, 40, 65

[19] C. Domain, R. Besson, and A. Legris, Acta Mater. **50**, 3513 (2002). ix, 47

[20] Y. Zhang, C. Jiang, and X. Bai, Sci. Rep. **7**, 41033 (2017). ix, 47

[21] A. Klumpp, U. Schaber, H. Offereins, K. Kuhl, and H. Sandmaier, Sens. Actuator A-Phys. **41**, 310 (1994). 3

[22] N. Ledermann, J. Baborowski, P. Muralt, N. Xantopoulos, and J.-M. Tellenbach, Surf. Coat. Technol. **125**, 246 (2000). 3

[23] B. Cox and W. Chenguang, J. Nucl. Mater. **199**, 272 (1993). 4

[24] M. W. Barsoum and T. El-Raghy, Am. Sci. **89**, 334 (2001). 7

[25] M. W. Barsoum, Prog. in Solid State Chem. **28**, 201 (2000). 7

[26] T. Liao, J. Wang, and Y. Zhou, Phys. Rev. B **73**, 214109 (2006). 7

[27] J. Wang and Y. Zhou, Phys. Rev. B **69**, 214111 (2004). 7, 64, 66

[28] K. R. Whittle *et al.*, Acta Mater. **58**, 4362 (2010). 7

[29] Z. Lin, M. Zhuo, Y. Zhou, M. Li, and J. Wang, Acta Mater. **54**, 1009 (2006). 7

[30] J. C. Napp *et al.*, J. Nucl. Mater. **409**, 53 (2011). 7

[31] Z. M. Sun, Int. Mater. Rev. **56**, 143 (2011). 7

[32] M. Radovic, M. Barsoum, T. El-Raghy, S. Wiederhorn, and W. Luecke, Acta Mater. **50**, 1297 (2002). 7

[33] Z. Sun, S. Li, R. Ahuja, and J. M. Schneider, Solid State Commun. **129**, 589 (2004). 9

[34] M. W. Barsoum *et al.*, J. Phys. Chem. Sol. **60**, 429 (1999). 9

[35] J.-P. Palmquist *et al.*, Phys. Rev. B **70**, 165401 (2004). 9

[36] Z. Lin, M. Zhuo, Y. Zhou, M. Li, and J. Wang, J. Am. Ceram. Soc. **89**, 3765 (2006). 9

[37] J. Zhang, B. Liu, J. Wang, and Y. Zhou, J. Mater. Res. **24**, 39 (2009). 9

[38] N. J. Lane, M. Naguib, J. Lu, L. Hultman, and M. W. Barsoum, J. Eur. Ceram. Soc. **32**, 3485 (2012). 9

[39] H. Zhang, X. H. Wang, H. M. Xiang, Z. J. Li, and Y. C. Zhou, Appl. Phys. Lett. **104**, 131903 (2014). 9

[40] M. W. Barsoum, *Encyclopedia of Materials Science and Technology* (Elsevier, 2006). 11, 64

[41] M. Barsoum and T. El-Raghy, J. Am. Ceramic Soc. **79**, 1953 (1996). 11, 101

[42] M. Barsoum, T. El-Raghy, and M. Radovic, Interceramics **49**, 226 (2000). 11

[43] M. Barsoum, D. Brodkin, and T. El-Raghy, Scr. Metall. Mater. **36**, 535 (1997). 11

[44] A. D. Bortolozo, O. H. Sant'Anna, C. A. M. dos Santos, and A. J. S. Machado, Mater. Sci-Pol **30**, 92 (2012). 11

[45] L. Toth, J. Less Common Met. **13**, 129 (1967). 11

[46] K. Sakamaki, H. Wada, H. Nozaki, Y. nuki, and M. Kawai, Solid State Commun. **112**, 323 (1999). 11

[47] A. D. Bortolozo *et al.*, Solid State Commun. **139**, 57 (2006). 11

[48] S. E. Lofland *et al.*, Phys. Rev. B **74**, 174501 (2006). 11

[49] A. Bortolozo, O. Sant'Anna, C. dos Santos, and A. Machado, Solid State Commun. **144**, 419 (2007). 11

[50] A. Bortolozo, Z. Fisk, O. Sant'Anna, C. dos Santos, and A. Machado, Physica C: Superconductivity **469**, 256 (2009). 11

[51] A. D. Bortolozo *et al.*, Solid State Commun. **150**, 1364 (2010). 11

[52] Y. Zhou and Z. Sun, Phys. Rev. B **61**, 12570 (2000). 11

[53] G. Hug and E. Fries, Phys. Rev. B **65**, 113104 (2002). 11

[54] J. Wang and Y. Zhou, Phys. Rev. B **69**, 214111 (2004). 11

[55] K. S. Novoselov *et al.*, Proc. Natl. Acad. Sci. **102**, 10451 (2005). 12

[56] J. N. Coleman *et al.*, Science **331**, 568 (2011). 12

[57] J. R. Harris and D. Scheffler, Micron **33**, 461 (2002). 12

[58] J. O. Sofo, A. S. Chaudhari, and G. D. Barber, Phys. Rev. B **75**, 153401 (2007). 12

[59] H. Kumar *et al.*, ACS Nano **11**, 7648 (2017). 12, 15

[60] M. Naguib *et al.*, Adv. Mater. **23**, 4248 (2011). 12, 82

[61] I. R. Shein and A. L. Ivanovskii, Comput. Mater. Sci. **65**, 104 (2012). 12, 14, 78

[62] I. R. Shein and A. L. Ivanovskii, Superlattices and Microstruct. **52**, 147 (2012). 12, 14, 78

[63] N. J. Lane, M. W. Barsoum, and J. M. Rondinelli, Europhys. Lett. **101**, 57004 (2013). 12

[64] R. Liu and W. Li, ACS Omega **3**, 2609 (2018). 12

[65] X.-H. Zha *et al.*, Sci. Rep. **6**, 27971 (2016). 12

[66] Q. Hu *et al.*, J. Phys. Chem. A **117**, 14253 (2013). 12, 78

[67] M. Naguib *et al.*, Electrochem. Commun. **16**, 61 (2012). 12

[68] S. Wang *et al.*, Comput. Mater. Sci. **83**, 290 (2014). 14, 82, 99, 101

[69] M. Khazaei, M. Arai, T. Sasaki, M. Estili, and Y. Sakka, Phys. Chem. Chem. Phys. **16**, 7841 (2014). 14

[70] M. Khazaei *et al.*, Adv. Funct. Mater. **23**, 2185 (2013). 14, 15, 101

[71] J. Halim *et al.*, Chem. Mater. **26**, 2374 (2014). 15

[72] J. Halim *et al.*, Adv. Funct. Mater. **26**, 3118 (2016). 15

[73] A. Lipatov *et al.*, Adv. Funct. Mater. **2**, 1600255 (2016). 15

[74] J. Xu, J. Shim, J. Park, and S. Lee, Adv. Funct. Mater. **26**, 5328 (2016). 15

[75] S. Lai *et al.*, Nanoscale **7**, 19390 (2015). 15

[76] K. Hantanasirisakul *et al.*, Adv. Electron. Mater. **2**, 1600050 (2016). 15

[77] A. Miranda, J. Halim, M. W. Barsoum, and A. Lorke, Appl. Phys. Lett. **108**, 033102 (2016). 15

[78] E. C. Stoner, Proc. Royal Soc. Lond A **169**, 339 (1939). 15

[79] C. Si, J. Zhou, and Z. Sun, ACS Appl. Mater. Interfaces **7**, 17510 (2015). 15

[80] S. A. Wolf *et al.*, Science **294**, 1488 (2001). 15

[81] M. I. Katsnelson, V. Y. Irkhin, L. Chioncel, A. I. Lichtenstein, and R. A. de Groot, Rev. Mod. Phys. **80**, 315 (2008). 15

[82] J. He, P. Lyu, and P. Nachtigall, J. Mater. Chem. C **4**, 11143 (2016). 16

[83] T. Mukhopadhyay, A. Mahata, S. Adhikari, and M. AsleZaeem, 2D Mater. **4**, 025006 (2017). 16, 88

[84] L.-Y. Gan, Y.-J. Zhao, D. Huang, and U. Schwingenschlögl, Phys. Rev. B **87**, 245307 (2013). 16

[85] M. Born and R. Oppenheimer, Ann. Phys. **389**, 457 (1927). 20

[86] P. Hohenberg and W. Kohn, Phys. Rev. **136**, B864 (1964). 22

[87] W. Kohn and L. J. Sham, Phys. Rev. **140**, A1133 (1965). 25

[88] R. M. Dreizler and E. K. U. Gross, *Density Functional Theory* (Springer, 1990). 28

[89] D. M. Ceperley and B. J. Alder, Phys. Rev. Lett. **45**, 566 (1980). 28

[90] J. P. Perdew and A. Zunger, Phys. Rev. B **23**, 5048 (1981). 28

[91] U. von Barth and L. Hedin, J. Phys. C: Solid State Phys. **5**, 1629 (1972). 28

[92] J. P. Perdew and W. Yue, Phys. Rev. B **33**, 8800 (1986). 28

[93] J. P. Perdew, K. Burke, and M. Ernzerhof, Phys. Rev. Lett. **77**, 3865 (1996). 28, 64, 79, 101

[94] T. L. Loucks, *Augmented Plane Wave Method* (W.A. Benjamin, 1967). 30

[95] P. E. Blöchl, Phys. Rev. B **50**, 17953 (1994). 31

[96] M. S. Daw and M. I. Baskes, Phys. Rev. Lett. **50**, 1285 (1983). 33

[97] M. I. Baskes, Phys. Rev. B **46**, 2727 (1992). 34

[98] J. H. Rose, J. R. Smith, F. Guinea, and J. Ferrante, Phys. Rev. B **29**, 2963 (1984). 36

[99] M. I. Baskes and R. A. Johnson, Modell. Simul. Mater. Sci. Eng. **2**, 147 (1994). 38

[100] B.-J. Lee and M. I. Baskes, Phys. Rev. B **62**, 8564 (2000). 38

[101] B.-J. Lee, M. Baskes, H. Kim, and Y. Koo Cho, Phys. Rev. B **64**, 184102 (2001). 38

[102] R. E. Peierls, Proc. Phys. Soc. **52**, 34 (1940). 39, 65

[103] F. R. N. Nabarro, Proc. Phys. Soc. **59**, 256 (1947). 39, 65

[104] T. Fuketa, T. Sugiyama, and F. Nagase, J. Nucl. Sci. Technol. **43**, 1080 (2006). 45

[105] S. M. Myers *et al.*, J. Nucl. Sci. Technol. **64**, 559 (1992). 45

[106] H. Okamoto, *Binary Alloys Phase Diagrams* (ASM International, 1996). 45, 51

[107] R. C. Bowman, B. D. Craft, J. S. Cantrell, and E. L. Venturini, Phys. Rev. B **31**, 5604 (1985). 45

[108] M. Gupta and J. P. Burger, Phys. Rev. B **24**, 7099 (1981). 45

[109] D. Shih, I. Robertson, and H. Birnbaum, Acta Metall. **36**, 111 (1988). 45

[110] H. Birnbaum and P. Sofronis, Mater. Sci. Eng. A **176**, 191 (1994). 45

[111] Y. Liang, P. Sofronis, and N. Aravas, Acta Mater. **51**, 2717 (2003). 45

[112] Y. Udagawa, M. Yamaguchi, H. Abe, N. Sekimura, and T. Fuketa, Acta Mater. **58**, 3927 (2010). 45

[113] C. Beachem, Metall. Mater. Trans. B **32**, 437 (1972). 45

[114] C. Domain, R. Besson, and A. Legris, Acta Mater. **52**, 1495 (2004). 45

[115] P. Sofronis, Y. Liang, and N. Aravas, Eur. J. Mech. A/Solids **20**, 857 (2001). 45

[116] C. Domain, R. Besson, and A. Legris, Acta Mater. **50**, 3513 (2002). 45, 48

[117] N. A. P. Kiran Kumar, J. A. Szpunar, and Z. He, J. Nucl. Mater. **403**, 101 (2010). 46

[118] W. Qin, N. A. P. Kiran Kumar, and J. A. Szpunar, Acta Mater. **59**, 7010 (2011). 46

[119] J. A. Szpunar, W. Qin, H. Li, and N. A. P. Kiran Kumar, J. Nucl. Mater. **427**, 343 (2012). 46

[120] C. Korn and S. D. Goren, Phys. Rev. B **33**, 68 (1986). 46

[121] C. J. Simpson and C. E. Ells, J. Nucl. Mater. **52**, 289 (1974). 46

[122] V. Grigoriev and B. Josefsson, J. Nucl. Mater. **257**, 99 (1998). 46

[123] A. Shmakov, D. Yan, and R. L. Eadie, Metal Sci. Heat Treat. **48**, 146 (2006). 46

[124] M. Farrow and B. Watkins, J. Nucl. Mater. **15**, 208 (1965). 46

[125] J. Hwan Kim, M. H. Lee, Y. H. Jeong, and J. G. Lim, Nucl. Eng. Des. **238**, 1441 (2008). 46

[126] S. Plimpton, J. Comput. Phys. **117**, 1 (1995). 47

[127] M. Liao, B. Li, and M. Horstemeyer, Comput. Mater. Sci. **79**, 534 (2013). 48

[128] I. Salehinia, J. Wang, D. Bahr, and H. Zbib, Int. J. Plast. **59**, 119 (2014). 48

[129] B.-J. Lee, M. Baskes, H. Kim, and Y. Koo Cho, Phys. Rev. B **64**, 184102 (2001). 48

[130] S. Groh, E. B. Marin, and M. F. Horstemeyer, Int. J. Appl. Mech. **02**, 191 (2010). 48

[131] M. Ghazisaeidi and D. Trinkle, Acta Mater. **60**, 1287 (2012). 48

[132] W. S. Ko and B. J. Lee, Phil. Mag. **94**, 1745 (2014). 48

[133] B. M. Lee and B. J. Lee, Metall. Mater. Trans. A **94**, 1745 (2014). 48, 49

[134] Y.-M. Kim, B.-J. Lee, and M. I. Baskes, Phys. Rev. B **74**, 014101 (2006). 48

[135] R. C. Bowman, B. D. Craft, J. S. Cantrell, and E. L. Venturini, Phys. Rev. B **31**, 5604 (1985). 48

[136] P. Zhang, B.-T. Wang, C.-H. He, and P. Zhang, Comput. Mater. Sci. **50**, 3297 (2011). 49

[137] M. R. Hestenes and E. Stiefel, J. Res. Natl. Bureau Stand. **49**, 409 (1952). 50

[138] S. Nose, J. Chem. Phys. **81**, 511 (1984). 50

[139] W. G. Hoover, Phys. Rev. A **31**, 1695 (1985). 50

[140] M. Parrinello and A. Rahman, J. Appl. Phys. **52**, 7182 (1981). 50

[141] A. L. Gurson, J. Eng. Mater. Tech. **99**, 2 (1977). 50

[142] T. Pardoen, Acta Mater. **46**, 541 (1998). 50

[143] S. Melchionna, G. Ciccotti, and B. L. Holian, Mol. Phys. **78**, 533 (1993). 50

[144] M. Bhatia, K. Solanki, A. Moitra, and M. A. Tschopp, Metall. Mater. Trans. A **44A**, 617 (2013). 50

[145] G. J. Ackland and A. P. Jones, Phys. Rev. B **73**, 054104 (2006). 50

[146] A. Stukowski, Model. Simul. Mater. Sci. Eng. **18**, 015012 (2010). 50, 52

[147] A. Moitra, Comp. Mater. Sci. **79**, 247 (2013). 52

[148] B. Y. Liu *et al.*, Nat. Comm. **5**, 4297 (2014). 55

[149] W. A. Johnson and R. F. Mehl, Trans. AIME **135**, 416 (1939). 55

[150] M. Avrami, J. Chem. Phys. **7**, 1103 (1939). 55

[151] P. C. Millett *et al.*, Comput. Mater. Sci. **50**, 949 (2011). 55

[152] P. C. Millett and M. Tonks, Comput. Mater. Sci. **50**, 2044 (2011). 55

[153] M. W. Barsoum and T. El-Raghy, American Scientist **89**, 334 (2001). 62

[154] M. Barsoum, Prog. Sol. St. Chem. **28**, 201 (2000). 63, 64, 101

[155] A. Guitton, A. Joulain, L. Thilly, and C. Tromas, Philos. Mag. **92**, 4536 (2012). 63, 71

[156] A. Guitton, A. Joulain, L. Thilly, and C. Tromas, Sci. Rep. **4**, 6358 (2014). 63

[157] K. Gouriet *et al.*, Philos. Mag. **95**, 2539 (2015). 63, 68

[158] M. Kabir, S. Mukherjee, and T. Saha-Dasgupta, Phys. Rev. B **84**, 205404 (2011). 64

[159] P. Chakraborty, T. Das, D. Nafday, L. Boeri, and T. Saha-Dasgupta, Phys. Rev. B **95**, 184106 (2017). 64

[160] S. Gupta and M. W. Barsoum, J. Electrochem. Soc. **151**, D24 (2004). 64

[161] Z. Sun, R. Ahuja, S. Li, and J. M. Schneider, Appl. Phys. Lett. **83**, 899 (2003). 64, 66

[162] Z. Sun, D. Music, R. Ahuja, S. Li, and J. M. Schneider, Phys. Rev. B **70**, 092102 (2004). 64, 66

[163] S. E. Lofland *et al.*, Appl. Phys. Lett. **84**, 508 (2004). 64, 66

[164] G. Kresse and J. Hafner, Phys. Rev. B **47**, 558 (1993). 64, 79, 101

[165] V. Vitek, Cryst. Latt. Def. **5**, 1 (1974). 65, 67, 68

[166] V. Volterra, Ann. Sci. c. Norm. Supr. **24**, 401 (1907). 65

[167] A. van de Walle and G. Ceder, Rev. Mod. Phys. **74**, 11 (2002). 66

[168] Z. Sun, D. Music, R. Ahuja, and J. M. Schneider, Phys. Rev. B **71**, 193402 (2005). 66

[169] S. F. Pugh, Philos. Mag. **45**, 823 (1954). 67

[170] S. Aubry and D. A. Hughes, Phys. Rev. B **73**, 1 (2006). 68

[171] K. S. Novoselov *et al.*, Science **306**, 666 (2004). 77

[172] K. S. Novoselov *et al.*, Nature **438**, 197 (2005). 77

[173] A. K. Geim and K. S. Novoselov, Nat. Mater. **6**, 183 (2007). 77

[174] V. Nicolosi *et al.*, Science **340**, 1226419 (2013). 77

[175] F. Gianluca *et al.*, Nat. Nanotechnol. **9**, 768 (2014). 77

[176] F. Xia, H. Wang, D. Xiao, M. Dubey, and A. Ramasubramaniam, Nat. Photonics **8**, 899 (2014). 77

[177] F. Koppens *et al.*, Nat. Nanotechnol. **9**, 780 (2014). 77

[178] D. Akinwande, N. Petrone, and J. Hone, Nat. Commun. **5**, 5678 (2014). 77

[179] A. Gupta, T. Sakthivel, and S. Seal, Prog. Mater. Sci. **73**, 44 (2015). 77

[180] M. Radovic and M. W. Barsoum, Am. Ceram. Soc. Bull. **92**, 20 (2013). 77

[181] M. Naguib, V. N. Mochalin, M. W. Barsoum, and Y. Gogotsi, Adv. Mater. **26**, 992 (2014). 78

[182] Z. Guo, L. Zhu, J. Zhou, and Z. Sun, RSC. Adv. **5**, 25403 (2015). 78

[183] M. Naguib *et al.*, ACS Nano **6**, 1322 (2012). 78

[184] Q. Tang, Z. Zhou, and P. Shen, J. Am. Chem. Soc. **134**, 16909 (2012). 78, 101

[185] X. Wang *et al.*, Adv. Mater. **26**, 4763 (2014). 78

[186] L. Zheng *et al.*, Proc. Natl. Acad. Sci. **117**, 16676 (2014). 78

[187] Z. Guo, J. Zhou, C. Si, and Z. Sun, Phys. Chem. Chem. Phys. **17**, 15348 (2015). 78, 88, 89, 95, 96, 111

[188] M. Kurtoglu, M. Naguib, Y. Gogotsi, and M. W. Barsoum, MRS Commun. **2**, 133 (2012). 78

[189] S. Grimme, J. Antony, S. Ehrlich, and H. Krieg, J. Chem. Phys. **132**, 154104 (2010). 80, 102

[190] V. I. Anisimov *et al.*, Phys. Rev. B **48**, 16929 (1993). 80

[191] H. J. Monkhorst and J. D. Pack, Phys. Rev. B **13**, 5188 (1976). 80, 102

[192] P. Blaha *et al.*, *WIEN2k: An Augmented Plane Wave plus Local Orbitals Program for Calculating Crystal Properties* (2001). 80

[193] S. Baroni, P. Giannozzi, and A. Testa, Phys. Rev. Lett. **58**, 1861 (1987). 81, 102

[194] P. Giannozzi *et al.*, J. Phys.: Condens. Matter **21**, 395502 (2009). 81, 102

[195] D. Vanderbilt, Phys. Rev. B **41**, 7892 (1990). 82, 102

[196] C. M. Fang, R. S. Koster, W. F. Li, and M. A. van Huis, RSC Adv. **4**, 7885 (2014). 82

[197] Y. Xie and P. R. C. Kent, Phys. Rev. B **87**, 235441 (2013). 84, 94, 96, 114

[198] Q. Peng and S. De, Phys. Chem. Chem. Phys. **15**, 19427 (2013). 89, 111

[199] R. C. Andrew, R. E. Mapasha, A. M. Ukpong, and N. Chetty, Phys. Rev. B **85**, 125428 (2012). 89

[200] M. Topsakal, S. Cahangirov, and S. Ciraci, Appl. Phys. Lett. **96**, 091912 (2010). 88

[201] L. Colombo *et al.*, Rep. Prog. Phys. **74**, 116501 (2011). 91

[202] J. F. Nye, *Physical Properties of Crystals* (Oxford, 1985). 91

[203] N. Mounet and N. Marzari, Phys. Rev. B **71**, 205214 (2005). 93

[204] H. Zabel, J. Phys: Condens. Matter **13**, 7679 (2001). 93

[205] H. Zhang *et al.*, J. Mater. Chem. A **4**, 12913 (2016). 96

[206] G. Gao *et al.*, Nanoscale **8**, 8986 (2016). 99

[207] G. Giovannetti *et al.*, Phys. Rev. B **76**, 073103 (2007). 100

[208] J. Jung, A. M. DaSilva, A. H. MacDonald, and S. Adam, Nat. Comm. **6**, 6308 (2015). 100

[209] H. Terrones, F. Lopez-Urias, and M. Terrones, Sci. Rep. **3**, 1549 (2013). 100

[210] L. Britnell *et al.*, Science **335**, 947 (2012). 100

[211] N. Myoung, K. Seo, S. J. Lee, and G. Ihm, ACS Nano **7**, 7021 (2013). 100

[212] G.-H. Lee *et al.*, ACS Nano **7**, 7931 (2013). 100

[213] J.-W. Jiang and H. S. Park, Appl. Phys. Lett. **105**, 033108 (2014). 101

[214] M. Sprinkle *et al.*, Phys. Rev. Lett. **103**, 226803 (2009). 101

[215] A. K. Geim and K. S. Novoselov, Nat. Mater. **6**, 183 (2007). 101

[216] M. I. Katsnelson, Mater. Today **10**, 20 (2007). 101

[217] M. R. Lukatskaya *et al.*, Science **341**, 1502 (2013). 101

[218] M. Naguib *et al.*, J. Am. Chem. Soc. **135**, 15966 (2013). 101

[219] P. E. Blöchl, Phys. Rev. B **50**, 17953 (1994). 101

[220] A. C. Neto *et al.*, Rev. Mod. Phys. **81**, 109 (2009). 102

[221] H.-P. Komsa and A. V. Krasheninnikov, Phys. Rev. B **88**, 085318 (2013). 105

[222] X. D. Li *et al.*, J. Phys. Chem. C **117**, 15347 (2013). 105

[223] W. Reim and J. Schoenes, *Handbook of Ferromagnetic Materials* (Elsevier, 1990). 109

[224] J. M. An and W. E. Pickett, Phys. Rev. Lett. **86**, 4366 (2001). 123

[225] M. Calandra, F. Mauri, and G. Profeta, Nat. Phys. **8**, 131 (2012). 123

[226] J. Lei, A. Kutana, and B. I. Yakobson, J. Mater. Chem. C **5**, 3438 (2017). 123